

**Integrated Optical Phased Arrays:
Augmented Reality, LiDAR, and Beyond**

by

Jelena Notaros

B.S., University of Colorado Boulder (2015)
S.M., Massachusetts Institute of Technology (2017)

Submitted to the
Department of Electrical Engineering and Computer Science
in partial fulfillment of the requirements for the degree of
Doctor of Philosophy in Electrical Engineering and Computer Science
at the

MASSACHUSETTS INSTITUTE OF TECHNOLOGY

May 2020

© Massachusetts Institute of Technology 2020. All rights reserved.

Author
Department of Electrical Engineering and Computer Science
May 15, 2020

Certified by.....
Michael R. Watts
Associate Professor of Electrical Engineering and Computer Science
Thesis Supervisor

Accepted by
Leslie A. Kolodziejcki
Professor of Electrical Engineering and Computer Science
Chair of the Department Committee on Graduate Students

Integrated Optical Phased Arrays: Augmented Reality, LiDAR, and Beyond

by

Jelena Notaros

Submitted to the Department of Electrical Engineering and Computer Science
on May 15, 2020, in partial fulfillment of the requirements for the degree of
Doctor of Philosophy in Electrical Engineering and Computer Science

Abstract

Integrated optical phased arrays, fabricated in advanced silicon-photonics platforms, enable manipulation and dynamic control of free-space light in a compact form factor, at low costs, and in a non-mechanical way. As such, integrated optical phased arrays have emerged as a promising technology for many wide-reaching applications, including LiDAR sensors and augmented-reality displays. In this thesis, novel integrated-optical-phased-array devices, systems, results, and applications are presented.

First, beam-steering optical phased arrays for LiDAR are shown, including the first beam-steering optical phased arrays powered by monolithically-integrated on-chip rare-earth-doped lasers, the first beam-steering optical phased arrays controlled using heterogeneously-integrated CMOS driving electronics, and the first single-chip coherent LiDAR with integrated optical phased arrays and CMOS receiver electronics. These demonstrations are important steps towards practical commercialization of low-cost and high-performance integrated LiDAR sensors for autonomous vehicles.

Next, integrated optical phased arrays for optical manipulation in the near field are developed, including the first near-field-focusing integrated optical phased arrays, the first quasi-Bessel-beam-generating integrated optical phased arrays, and a novel active butterfly architecture for independent amplitude and phase control. These near-field modalities have the potential to advance a number of application areas, such as optical trapping for biological characterization, trapped-ion quantum computing, and laser-based 3D printing.

Finally, a novel transparent integrated-phased-array-based holographic display is proposed as a highly-discreet and fully-holographic solution for the next generation of augmented-reality head-mounted displays; novel passive near-eye displays that generate holograms, the first integrated visible-light liquid-crystal-based phase and amplitude modulators, and the first actively-tunable visible-light integrated optical phased arrays are presented.

Thesis Supervisor: Michael R. Watts

Title: Associate Professor of Electrical Engineering and Computer Science

To the pioneering giants of electromagnetics and photonics
for providing the foundations of this thesis.

To my current and past advisors, mentors, and professors
for helping me to nearly understand and fully love this field.

To my groupmates and colleagues throughout the years
for all the collaborations and friendships.

To Branislav, Olivera, Milica, and Tesh
for everything else.

Acknowledgments

Throughout my time at both the Massachusetts Institute of Technology and the University of Colorado Boulder, I have had the privileged of working with, learning from, and being supported by many excellent advisors, mentors, and colleagues, all of whom deserve my deepest gratitude.

Foremost, I would like to thank my thesis advisor, Professor Michael R. Watts. Thank you for giving me the exceptional opportunity, genuine advice, overall support, and extensive resources to develop as a young researcher and leader, for which I am truly appreciative.

I would also like to thank all of the other professors and program managers that have served as my advisors, mentors, and collaborators throughout the years, including Professor Erich P. Ippen, Professor Vladimir M. Stojanovic, Professor Milos A. Popovic, Dr. Gordon A. Keeler, Professor Marc A. Baldo, Professor Dirk R. Englund, Professor Franz X. Kaertner, Professor Rajeev J. Ram, Professor Leslie A. Kolodziejski, and Professor Tomas Palacios. Thank you for all of your support, guidance, and advice. It has made a lasting impact on me and my future, and, for that, I am extremely grateful.

Next, I would like to thank all of my current and former groupmates and collaborators throughout the years, in the MIT Photonic Microsystems Group (Milica Notaros, Manan Raval, Christopher V. Poulton, Matthew J. Byrd, Nanxi Li, Zhan Su, Emir Salih Magden, Erman Timurdogan, Diedrik Vermeulen, Neetesh Singh, Alfonso Ruocco, and Purnawirman), at the SUNY Polytechnic Institute (Thomas Dyer, Christopher Baiocco, and Daniel Coleman), in the UC Berkeley Integrated Systems Group (Taehwan Kim, Pavan Bhargava, Panagiotis Zarkos, Sajjad Moazeni, Nandish

Mehta, Sidney Buchbinder, and Krishna T. Settaluri), in the CU Boulder Nanophotonic Systems Laboratory (Fabio Pavanello, Mark T. Wade, Rajesh Kumar, Nathan Dostart, Gil Triginer Garces, Cale M. Gentry, Xiaoge Zeng, and Yangyang Liu), in the MIT Optics and Quantum Electronics Group (Ming Xin, Patrick T. Callahan, Katia Shtyrkova, Ravi Koustuban, and Phillip Donnie Keathley), in the MIT Quantum Photonics Laboratory (Eric Bersin, Jordan A. Goldstein, Jacob Mower, Mikkel Heuck, Uttara Chakraborty, Jacques Carolan, Darius Bunandar, Nicholas C. Harris, and Gregory R. Steinbrecher), and in the MIT Physical Optics and Electronics Group (Amir H. Atabaki and Luca Alloatti). Thank you for your mentorship during the early stages of my academic career, your contributions without which this work would not have been possible, and your friendships that have made every success that much more meaningful. It has truly been a pleasure working with and learning from all of you.

Additionally, I would like to thank all of the MIT EECS, RLE, and MTL staff, especially Dianne Loir, Melissa Sheehan, Gary Riggott, Kurt Broderick, Janet Fischer, William Adams, Benjamin Sharma, Alicia Duarte, Kathleen McCoy, Paul Palei, and Teresa Avila. Thank you for all of your administrative, programmatic, and fabrication support throughout the years.

Finally, to Branislav, Olivera, Milica, and Tesh, to put it simply, thank you for everything. This thesis is dedicated to you.

Funding: This work was supported by the DARPA Visible Integrated Photonics Enhanced Reality (VIPER) program (Grant No. FA8650-17-1-7713), the DARPA Electronic-Photonic Heterogeneous Integration (E-PHI) program (Grant No. HR0011-12-2-0007), the DARPA Direct On-Chip Digital Optical Synthesizer (DODOS) project (Grant No. HR0011-15-C-0056), an MIT Grier Presidential Fellowship, and an NSF Graduate Research Fellowship (Grant No. 1122374).

Contents

1	Introduction	25
2	Beam-Steering Integrated Optical Phased Arrays for LiDAR	28
2.1	Integrated Optical Phased Arrays with Monolithically-Integrated Lasers	30
2.1.1	Introduction	30
2.1.2	Platform	32
2.1.3	Architecture	35
2.1.4	Experimental Results	39
2.1.5	Conclusion	41
2.2	Integrated Optical Phased Arrays with 3D-Integrated Electronics . .	44
2.2.1	Introduction	44
2.2.2	Platform	45
2.2.3	OPA Architecture and Experimental Results	45
2.2.4	LiDAR Architecture and Experimental Results	49
2.2.5	Conclusion	51
3	Near-Field Integrated Optical Phased Arrays	53
3.1	Near-Field-Focusing Integrated Optical Phased Arrays	55
3.1.1	Introduction	55
3.1.2	Theory	57
3.1.3	Splitter-Tree-Based Architecture and Experimental Results . .	62
3.1.4	Pixel-Based Architecture and Experimental Results	70
3.1.5	Conclusion	75

3.2	Bessel-Beam-Generating Integrated Optical Phased Arrays	78
3.2.1	Introduction	78
3.2.2	Theory	79
3.2.3	Architecture	83
3.2.4	Experimental Results	87
3.2.5	Conclusion	88
3.3	Butterfly-Pixel-Based Integrated Optical Phased Arrays	91
3.3.1	Introduction	91
3.3.2	Architecture and Experimental Results	92
3.3.3	Conclusion	94
4	Visible-Light Integrated Photonics for Augmented Reality	96
4.1	Integrated Visible-Light LC-Based Phase Modulators	98
4.1.1	Introduction	98
4.1.2	Theory and Packaging	98
4.1.3	Experimental Results	101
4.1.4	Conclusion	103
4.2	Integrated Visible-Light LC-Based Variable-Tap Amplitude Modulators	105
4.2.1	Introduction	105
4.2.2	Theory and Design	106
4.2.3	Experimental Results	108
4.2.4	Conclusion	109
4.3	Integrated Visible-Light LC-Based Integrated Optical Phased Arrays	110
4.3.1	Introduction	110
4.3.2	Architecture	111
4.3.3	Experimental Results	113
4.3.4	Conclusion	114
4.4	Integrated-Photonics-Based Holographic Displays for Augmented Reality	115
4.4.1	Introduction	115
4.4.2	Passive Architecture and Experimental Results	117

4.4.3	Active Architecture and Experimental Results	121
4.4.4	Conclusion	124
5	Conclusion	126

List of Figures

2.1	Simplified layer schematics of the monolithically-integrated silicon-photonics platform utilized for the phased-array system (a) before the gain trench is etched, (b) after the gain trench is etched, and (c) after the gain film is deposited (not to scale).	33
2.2	Simplified schematic of the phased-array system with an on-chip laser showing major components and process layers (not to scale).	35
2.3	(a) Schematic of the center section of the on-chip DFB laser showing the five-segment gain waveguide, gratings, and center gaps. Simulated mode profiles of the (b) 980-nm-wavelength pump and (c) 1599-nm-wavelength signal in the DFB waveguide.	36
2.4	(a) Schematic of the layer transitions and DC wavelength filter (not to scale). (b) Simulated transmission versus wavelength for the tap (blue) and thru (green) ports of the DC filter.	37
2.5	Simplified schematic of the cascaded-architecture integrated optical phased array.	38
2.6	(a) Photograph of the fabricated phased-array system with an on-chip laser and the experimental setup. (b) Diagram illustrating the experimental setup used to characterize the on-chip laser.	39
2.7	Measured optical spectrum of the on-chip laser showing (a) the full spectrum including the amplified spontaneous emission and (b) the lasing peak at 1599 nm.	40

2.8	(a) Measured far field above the chip showing the main lobe of the phased array. (b) Intensity cross sections of the far-field main lobe in the array dimension (green) and the antenna dimension (blue). (c) Experimental results showing beam steering in the array dimension, Ψ , versus applied electrical power.	41
2.9	(a) Simplified layer schematics showing the key process steps of the 3D-integrated electronics-photonics platform (not to scale). Photographs of (b) the fabricated 3D-integrated 300-mm-diameter wafer and (c) the packaged 3D-integrated chip. (Figures from [9–11].)	46
2.10	Simplified (a) diagram and (b) schematic (not to scale) of the cascaded-architecture integrated optical phased array with integrated CMOS driving electronics. (Figures from [9].)	47
2.11	Measured far field above the packaged chip showing the main lobe of the integrated optical phased array (a) before and (b) after calibration. Experimental results showing beam steering in the (c) array dimension, θ , and (d) antenna dimension, ϕ . (Figures from [9].)	48
2.12	(a) Simplified diagram of the integrated coherent LiDAR system with integrated optical phased arrays and integrated CMOS receiver electronics. (b) Micrograph of the fabricated integrated coherent LiDAR system. (Figures from [11].)	49
2.13	(a) Photograph of the LiDAR characterization setup showing the packaged integrated coherent LiDAR chip and three target positions. (b) Experimental results showing the raw receiver output signals and corresponding post-processed measured versus actual target distances for each of the three target positions. (Figures from [11].)	50
3.1	(a) Schematic of a generalized focusing phased array showing the antenna pitch and focal length. Element phase distribution for a focusing phased array with (b) 40 mm and (c) 20 mm focal length assuming 512 antennas, 2 μm antenna pitch, and 1550 nm wavelength.	58

3.2	Simulated array-factor intensity above the array for a (a) non-focusing, (b) 40 mm focal length, and (c) 20 mm focal length phased array. (d) Simulated cross-sectional array-factor intensity at the focal plane for the 40 mm focal length (black) and 20 mm focal length (red) phased array. Simulated intensities are shown for an array with 512 antennas, 2 μm antenna pitch, and 1550 nm wavelength.	59
3.3	(a) Simulated power full width at half maximum (FWHM) versus aperture size for a focusing phased array with 5 mm focal length and 1550 nm wavelength. (b) Simulated power FWHM versus focal length for a focusing phased array with 1 mm aperture size and 1550 nm wavelength.	60
3.4	Simulated array-factor intensity above the array assuming (a) no steering, (b) linear steering, and (c) corrected non-linear steering. Simulated intensities are shown for an array with $f_x = 1.5$ mm offset, 512 antennas, 2 μm antenna pitch, 5 mm focal length, and 1550 nm wavelength.	61
3.5	Element phase distribution for a focusing phased array with an $f_x = 1.5$ mm offset assuming linear steering (red) and corrected non-linear steering (yellow). Phase profiles are shown for an array with 512 antennas, 2 μm antenna pitch, 5 mm focal length, and 1550 nm wavelength.	62
3.6	(a) Schematic of a splitter-tree-based focusing phased array with 4 antennas. (b) Micrograph of a fabricated splitter-tree-based focusing phased array with 512 antennas and 2 μm antenna pitch.	63
3.7	(a) Schematic of a phase bump device. (b) Simulated (red) and measured (black) relative phase versus phase bump width for the phase bump device.	64

3.8	(a) Schematic of a grating-based antenna. (b) Simulated (red) and measured (black) scattering strength versus antenna perturbation for the grating-based antenna. (c) Simulated relative phase versus length of the unperturbed section of the grating-based antenna. (d) Synthesized unperturbed section length versus distance along the antenna necessary for focusing at 1 mm (yellow), 5 mm (red), and 10 mm (black) for a focusing antenna with a constant 30 nm perturbation and 310 nm perturbed length.	65
3.9	Photographs of (a) a fabricated integrated optical phased array chip on the scanning near-field characterization setup and (b) the scanning near-field characterization setup.	66
3.10	Measured cross-sectional intensity (in dB) above the chip for a 2D-focusing splitter-tree-based phased array in the (a) x plane and (b) y plane with top-down intensity shown (e) in the plane of the chip, (d) at the focal plane, and (c) above the focal plane. Intensities are shown for an array with 512 antennas, 2 μm antenna pitch, 5 mm focal length, and 1550 nm wavelength.	67
3.11	(a) Measured cross-sectional intensity (in dB) above the chip for a 1D-focusing splitter-tree-based phased array with top-down intensity shown (d) in the plane of the chip, (c) at the focal plane, and (b) above the focal plane. Intensities are shown for an array with 512 antennas, 2 μm antenna pitch, 5 mm focal length, and 1550 nm wavelength. . . .	68
3.12	Measured cross-sectional intensity (in dB) above the chip for a 2D-focusing splitter-tree-based phased array at (a) 1550 nm, (b) 1560 nm, and (c) 1570 nm wavelengths. (d) Experimental results showing steering in the antenna dimension, y , versus wavelength. Results are shown for an array with 512 antennas, 2 μm antenna pitch, and 5 mm focal length.	70

3.13	(a) Schematic of a pixel-based focusing phased array with 64 antennas. (b) Micrograph of a fabricated pixel-based focusing phased array with 1024 antennas and 10 μm antenna pitch.	71
3.14	Simulated (a) coupling versus coupling waveguide length and (b) relative phase versus offset length for the pixel-based architecture unit cell. Schematics of the unit cell are included as insets with each variable length indicated.	72
3.15	Measured cross-sectional intensity (in dB) above the chip for a 5-mm-focal-length pixel-based phased array in the (a) x plane and (b) y plane with top-down intensity shown (e) in the plane of the chip, (d) at the focal plane, and (c) above the focal plane. Intensities are shown for an array with 1024 antennas, 10 μm antenna pitch, and 1550 nm wavelength.	74
3.16	Simulated (red) and measured (black) power full width at half maximum (FWHM) versus focal length. Results are shown for pixel-based arrays with 1024 antennas, 10 μm antenna pitch, and 1550 nm wavelength.	75
3.17	(a) Element amplitude distribution for a Gaussian-amplitude phased array with $A_0 = 1/2$ (red) and $A_0 = 1$ (yellow). (b) Element phase distribution for a standard (yellow) and Bessel (red) phased array with $\Phi_0 = 0$ and $\Phi_0 = 5\pi$, respectively. Phase and amplitude profiles and simulated intensities are shown for an array with 64 antennas, 10 μm antenna pitch, and 1550 nm wavelength.	80
3.18	Simulated array-factor intensity above the array for a (a) Gaussian array with $\Phi_0 = 0$ and $A_0 = 1/2$, (b) Bessel array with $\Phi_0 = 4\pi$ and $A_0 = 1/2$, (c) Bessel array with $\Phi_0 = 5\pi$ and $A_0 = 1/2$, and (d) distorted Bessel array with $\Phi_0 = 5\pi$ and $A_0 = 1$. Simulated intensities are shown for an array with 64 antennas, 10 μm antenna pitch, and 1550 nm wavelength.	81

3.19	Simulated (a) power full width at half maximum (FWHM) and (b) Bessel length versus array aperture size for an array with $\Phi_0 = 5\pi$, $A_0 = 1/2$, and 1550 nm wavelength. Simulated (c) FWHM and (d) Bessel length versus maximum element phase variation, Φ_0 , for an array with 64 antennas, 10 μm antenna pitch, $A_0 = 1/2$, and 1550 nm wavelength.	82
3.20	Micrograph of the fabricated quasi-Bessel-beam-generating phased array with 64 antennas and 10 μm antenna pitch.	83
3.21	(a) Schematic of a multi-mode-interference (MMI) splitter. (b) Simulated (red) and measured (black) efficiency versus MMI device length [70].	84
3.22	(a) Schematic of a tap coupler device. (b) Simulated (red) and measured (black) coupling versus coupling length assuming a 500 nm coupling gap.	85
3.23	(a) Schematic of a phase taper device. (b) Simulated (red) and measured (black) relative phase versus length of the 2.2- μm -wide section of the phase taper.	86
3.24	(a) Schematic of a grating-based antenna. (b) Simulated (red) and measured (black) scattering strength versus antenna perturbation. . .	86
3.25	(a) Measured cross-sectional intensity (in dB) above the chip for a quasi-Bessel-beam-generating phased array with top-down intensity shown (d) in the plane of the chip ($z = 0$ mm), (c) within the Bessel region of the emitted beam ($z = 11$ mm), and (b) after breakdown of the Bessel region ($z = 22$ mm). Intensities are shown for an array with 64 antennas, 10 μm antenna pitch, $\Phi_0 = 5\pi$, $A_0 = \sqrt{2}/2$, and 1550 nm wavelength.	87

3.26 (a) Measured cross-sectional intensity (in dB) above the chip for a quasi-Bessel beam generated by a phased array when obstructed by a gold wire. Top-down intensities are shown (d) in the plane of the obstacle ($z = 7.5$ mm), (c) within the shadow zone of the obstacle ($z = 10$ mm), and (b) after reformation of the central beam ($z = 12.5$ mm). Intensities are shown for an array with 64 antennas, $10\ \mu\text{m}$ antenna pitch, $\Phi_0 = 5\pi$, $A_0 = \sqrt{2}/2$, and 1550 nm wavelength. 89

3.27 (a) Simplified schematic of the integrated optical phased array butterfly architecture with inset showing (b) an 8×8 array of butterfly pixels. In the schematics, the red, green, blue, and black shapes represent the silicon waveguides, bottom metal, top metal, and vias, respectively (doping layers and other process layers are not shown for clarity). . . 92

3.28 Simplified schematics of (a) a butterfly coupler and (b) a butterfly pixel. In the schematics, the red, green, blue, and black shapes represent the silicon waveguides, bottom metal, top metal, and vias, respectively (doping layers and other process layers are not shown for clarity). (c) Experimentally measured transmission into the thru (blue) and tap (green) waveguides versus applied amplitude-line electrical power for the fabricated butterfly coupler. (d) Experimentally measured transmission into the thru waveguides (blue/green) and radiation out of the antenna (red) versus applied amplitude-line electrical power for the fabricated butterfly pixel. 93

4.1	(a) Cross-sectional schematic of the integrated liquid-crystal-based phase modulator (not to scale). (b) Top-view schematic of the integrated liquid-crystal-based phase modulator showing the liquid-crystal molecule alignment with no electric field applied versus with maximum electric field applied (not to scale). (c) Simulated mode profiles of the fundamental transverse-electric mode in the integrated liquid-crystal-based phase modulator for a liquid-crystal index of $n_{LC} = 1.53$ versus $n_{LC} = 1.62$	99
4.2	Cross-sectional schematic of the liquid-crystal-based phase modulator (a) as received from SUNY Poly with an initial cross section consisting of an SiN waveguide, empty trench, and electrodes, (b) after in-house dry etch to bring the trench closer to the top of the waveguide, (c) after patterning of the SU-8 photoresist spacer layer, (d) after the top glass chip with an alignment layer is epoxied on top of the spacer layer, and (e) after the liquid crystal is injected into the cavity and sealed with the UV-cured epoxy (not to scale).	101
4.3	Simplified schematic of the integrated MZI test structure and modulation scheme showing major components (not to scale).	102
4.4	Photograph of the fabricated and packaged integrated liquid-crystal-based phase modulator chip and experimental setup.	102
4.5	Experimental results for the integrated liquid-crystal-based phase modulator showing normalized output power versus peak-to-peak voltage applied to one arm of the MZI test structure.	103
4.6	(a) Simplified schematic of the liquid-crystal-based variable-tap amplitude modulator. (b) Cross section of the coupling region after packaging (not to scale).	106
4.7	(a) Simulated tap transmission versus coupler length for various tap waveguide widths. (b) Simulated tap transmission versus liquid-crystal refractive index for various tap waveguide widths.	107

4.8	Experimental results showing tap power output under 1-Hz modulation (speed limited by the detection equipment).	108
4.9	(a) Partial schematic of the liquid-crystal-based integrated optical phased array showing major components. Simplified schematics of the (b) layer-transition escalator, (c) evanescent tap coupler, and (d) grating-based antennas used in the liquid-crystal-based integrated optical phased array.	111
4.10	Photograph of the packaged optical-phased-array chip, experimental setup, and output radiated light.	112
4.11	(a) Measured far field above the chip showing the main lobe of the phased array. (b) Intensity cross sections of the far-field main lobe in the array dimension (θ) and antenna dimension (Ψ). (c) Experimental results showing beam steering in the array dimension (θ) versus applied peak-to-peak voltage.	113
4.12	Simplified diagram of (a) a typical HMD approach using an optical relay system versus (b) the direct-view near-eye VIPER approach. . .	115
4.13	Photographs showing (a) a 300-mm-diameter glass-bonded VIPER wafer, (b) three glass-bonded VIPER chips, and (c) a glass-bonded VIPER chip in the near-eye modality.	116
4.14	(a) Simplified schematic of the VIPER display showing the input optical fiber, active distribution network, and grid of optical-phased-array-based pixels. (b) Viewing configuration for the VIPER display showing the virtual holographic image formed behind the display.	117
4.15	(a) Schematic of the passive VIPER display with 32×32 pixels, $32 \mu\text{m}$ pixel pitch, 6 antennas per a pixel, and $4 \mu\text{m}$ antenna pitch. (b) Schematic of a single optical-phased-array-based pixel of the passive VIPER display showing the phase taper for pixel absolute phase encoding, evanescent tap for pixel amplitude encoding, and pixel-to-antenna taps with varying spatial offsets for pixel phase gradient encoding. . .	118

4.16	(a) Simulation of the virtual image projected by the passive VIPER display and corresponding (b) amplitude, (c) absolute phase, and (d) phase gradient encodings, assuming a 632.8 nm operating wavelength, 1 m virtual object distance, 20 mm human eye focal length, and 12 mm eye relief.	119
4.17	Photograph of (a) the VIPER characterization setup showing the input optical fiber, photonic chip, lens emulating the lens in the eye, and camera emulating the retina, and (b) the transparent holographic-display chip. (c) Experimental measurement of the virtual image projected by the passive VIPER display with a ~ 1 m virtual object distance, 20 mm focal length lens, and 12 mm eye relief.	120
4.18	Partial schematic of the active VIPER display with 4×4 pixels, $32 \mu\text{m}$ pixel pitch, 8 antennas per a pixel, and $4 \mu\text{m}$ antenna pitch.	121
4.19	Schematic of a single optical-phased-array-based pixel of the active VIPER display showing major components, including the liquid-crystal-based phase shifter for pixel absolute phase encoding, liquid-crystal-based variable tap for pixel amplitude encoding, and liquid-crystal-based pixel bus with compact cascaded pixel-bus-to-antenna taps for pixel phase gradient encoding.	122
4.20	Experimental results for a single active VIPER pixel showing (a) power radiated out of the pixel versus applied peak-to-peak variable tap voltage and (b) pixel phase gradient shift versus applied peak-to-peak cascade voltage. (c) Experimental results showing five images of the near field of the multi-pixel active VIPER display; in this experiment, the display was encoded to spell out the letters in the word "LIGHT". . .	123

Chapter 1

Introduction

By enabling optical microsystems with new functionalities, improved system performance, and reduced size, weight, and power, integrated photonics is positioned to enable next-generation optical technologies that facilitate revolutionary advances for numerous fields spanning science and engineering, including computing, sensing, communications, displays, quantum, and biology.

An emerging class of integrated photonic systems is integrated optical phased arrays, which enable manipulation and dynamic control of free-space light in a compact form factor, at low costs, and in a non-mechanical way. As such, integrated optical phased arrays have emerged as a promising technology for many wide-reaching applications, including light detection and ranging (LiDAR) for autonomous vehicles, three-dimensional (3D) holography for augmented-reality displays, free-space optical communications, and trapped-ion quantum computing.

In this thesis, novel integrated-optical-phased-array devices, systems, results, and applications will be presented [1–6].

First, in Ch. 2, beam-steering optical phased arrays for LiDAR will be shown, including the first beam-steering optical phased array powered by a monolithically-integrated on-chip rare-earth-doped laser [7,8], the first beam-steering optical phased array controlled using heterogeneously-integrated CMOS driving electronics [9, 10], and the first single-chip coherent LiDAR with integrated optical phased arrays and

CMOS receiver electronics [11]. These demonstrations are important steps towards practical commercialization of low-cost and high-performance integrated LiDAR sensors for autonomous vehicles.

Next, in Ch. 3, integrated optical phased arrays for optical manipulation in the near field will be developed, including the first near-field-focusing integrated optical phased arrays [12, 13], the first quasi-Bessel-beam-generating integrated optical phased arrays [14, 15], and a novel active butterfly architecture for independent amplitude and phase control [16, 17]. These near-field modalities have the potential to advance a number of application areas, such as optical trapping for biological characterization, trapped-ion quantum computing, and laser-based 3D printing.

Finally, in Ch. 4, a novel transparent integrated-phased-array-based holographic display will be proposed as a highly-discreet and fully-holographic solution for the next generation of augmented-reality head-mounted displays; novel passive near-eye displays that generate holograms [18, 19], the first integrated visible-light liquid-crystal-based phase [20, 21] and amplitude [22, 23] modulators, and the first actively-tunable visible-light integrated optical phased arrays [24] will be presented.

The work discussed in this thesis has resulted in a number of publications upon which this thesis is based [1–24]. Contributions were also made to a number of additional results, including the first optical frequency synthesizer using an integrated rare-earth-doped laser [25, 26], the first monolithically-integrated rare-earth-doped tunable lasers [27, 28] and mode-locked lasers [29], the first integrated datalink powered by an on-chip rare-earth-doped laser [30], a novel integrated transceiver for quantum-secure communications [31, 32], and a novel integrated high-speed non-linear modulator operating at cryogenic temperatures [33]; however, these additional contributions will not be discussed in this thesis.

Chapter 2

Beam-Steering Integrated Optical Phased Arrays for LiDAR

Light detection and ranging (LiDAR) has emerged as a vital and widely-used sensing technology for autonomous systems, such as autonomous vehicles, since it enables 3D mapping with higher resolution than traditional RADAR. However, current commercial LiDAR systems utilize mechanical beam-steering mechanisms that decrease reliability and increase production cost. To address these limitations, integrated optical phased arrays, which enable low-cost, high-speed, and compact non-mechanical beam steering, have emerged as a promising solution for next-generation LiDAR.

In this chapter, the first beam-steering integrated optical phased array powered by an on-chip rare-earth-doped laser will be shown in Sec. 2.1 [7, 8]; this system represents the first demonstration of a rare-earth-doped laser monolithically integrated with an active CMOS-compatible silicon-on-insulator photonics system. Additionally, the first beam-steering optical phased array heterogeneously integrated with CMOS driving electronics [9, 10] and the first single-chip coherent LiDAR with integrated optical phased arrays and CMOS receiver electronics [11], both in a novel 3D-integrated electronics-photonics platform, will be presented in Sec. 2.2 (collaboration with the Berkeley Stojanovic group); this 3D integration scheme allows for photonics and CMOS electronics to be independently optimized and scaled, while

maintaining dense interconnections. These laser- and electronics-integration demonstrations are important steps towards practical commercialization of low-cost and high-performance integrated LiDAR sensors for autonomous vehicles.

2.1 Integrated Optical Phased Arrays with Monolithically-Integrated Lasers

The following work was done in collaboration with Nanxi Li (MIT), Christopher V. Poulton (MIT), Zhan Su (MIT), Matthew J. Byrd (MIT), Emir Salih Magden (MIT), Erman Timurdogan (MIT), Christopher Baiocco (SUNY Poly), Nicholas M. Fahrenkopf (SUNY Poly), and Michael R. Watts (MIT). This work has been published in [7,8].

2.1.1 Introduction

Integrated optical phased arrays, fabricated in advanced silicon-photonics platforms, enable manipulation and dynamic control of free-space light with large aperture sizes and fast steering rates [9,12,19,34–44]. As such, integrated optical phased arrays have many promising wide-reaching applications, including light detection and ranging (LiDAR) [34], holographic displays [19,35], and free-space optical communications [36].

However, due to the absence of a direct-band-gap material in standard silicon-photonics platforms, many of these demonstrations have been limited to systems with off-chip fiber-coupled input lasers. Given that the majority of phased-array applications require sources with narrow linewidths and wide tunability, this results in systems utilizing expensive benchtop tunable lasers with large form factors that restrict the systems' practicality.

To improve the practicality of these systems, phased-array systems with on-chip laser sources have been demonstrated using a hybrid III-V/silicon laser integration approach (wherein a III-V epitaxial material is bonded to the silicon chip and patterned to define the gain regions of the on-chip laser) [37,38] and using an indium-phosphide-based platform (wherein gain is achieved using a front-end quantum-well intermixing technology) [39]. However, although there have been significant commercial efforts in large-scale production of heterogeneously-integrated photonics platforms, including

by Intel [45], Juniper Networks [46], and HP Enterprise [47], these platforms require complex fabrication methods.

Compared to these approaches, optically-pumped monolithically-integrated rare-earth-doped lasers [27, 48–57] offer an approach to on-chip light generation that requires only a single CMOS-compatible back-end deposition step that could be performed at a low cost on the wafer scale. Although rare-earth-doped lasers require an optical pump source, this approach greatly reduces the linewidth and tunability requirements for the input pump since the output wavelength, linewidth, and tunability of the laser are determined by the integrated cavity design. As such, these lasers enable high output powers [49], kilohertz linewidth [50], and wide tunability [27] using inexpensive single-frequency pump sources.

Although rare-earth-doped lasers have been demonstrated in prior work, they have been limited to passive stand-alone lasers [48–56], passive lasers powering passive systems [57], and stand-alone tunable lasers based on metal heaters [27]. Thus far, a monolithically-integrated rare-earth-doped laser has yet to be demonstrated in an active silicon-on-insulator (SOI) photonics system. This is due to the challenges associated with integrating the rare-earth-doped gain material into an active photonics layer stack with multiple waveguide layers, silicon dopants, and routing metals, and ensuring that the gain deposition temperature does not detrimentally affect the active components [48].

In this section, an erbium-doped laser and an electrically-steerable optical phased array are monolithically integrated in an active silicon-photonics platform. An advanced CMOS-compatible 300-mm-wafer silicon-photonics platform was developed that consists of a silicon layer with eight doping masks, two silicon-nitride layers, three metal and via layers, a dicing trench for smooth edge-coupled facets, and a gain-film trench that enables interaction between the gain material and waveguide layers. This platform was used to demonstrate an integrated system consisting of an optically-pumped on-chip laser, layer-transition and wavelength-filtering devices, and an active optical phased array. Lasing with a single-mode output, 30 dB side-mode-suppression ratio (SMSR), and 40 mW lasing threshold was shown, and one-

dimensional beam steering with a $0.85^\circ \times 0.20^\circ$ full-width-at-half-maximum (FWHM) beam and $30^\circ/\text{W}$ electrical steering efficiency was demonstrated. This system represents the first demonstration of an active SOI photonics system powered by a rare-earth-doped monolithically-integrated laser and paves the way for future monolithic silicon-photonics systems, such as data communication links [58] and on-chip optical synthesizers [26, 59].

2.1.2 Platform

The monolithically-integrated system was fabricated at SUNY Poly in an advanced CMOS-compatible 300-mm-wafer silicon-photonics platform consisting of a silicon layer with eight doping masks, two silicon-nitride (Si_3N_4) layers, three metal layers for electrical routing and contact pads, two via layers and metal-to-silicon contacts, a dicing trench for fiber coupling, and a trench for deposition of an erbium-doped aluminum-oxide ($\text{Al}_2\text{O}_3:\text{Er}^{3+}$) thin film (performed at MIT). Figure 2.1 shows a simplified schematic of the layers in the platform.

In the developed platform, a 300-mm-diameter SOI wafer with $2\ \mu\text{m}$ buried silicon-dioxide (SiO_2) thickness and a standard 220-nm-thick silicon device layer was used. This silicon layer was patterned using 193 nm deep-ultraviolet immersion lithography in two steps: a full etch to define silicon strip waveguides and a 120 nm partial etch to define 100-nm-thick silicon ridges. Any residual line-edge roughness was reduced using oxidation and removal steps. The active silicon devices, such as thermal phase shifters [40] and modulators [60], were then P- or N-type doped to define junctions for modulation or increase electrical conductivity for on-chip heaters. A suite of eight dopant masks was used with varying dopant species (Arsenic, Phosphorus, and BF_2), doses, and energies to enable P- and N-type doping for both full-height and partial-height waveguides.

Next, a tetraethylorthosilicate (TEOS) plasma-enhanced-chemical-vapor-deposition (PECVD) SiO_2 layer was deposited on top of the silicon layer and its top surface was planarized using a chemical-mechanical polishing (CMP) step leaving 100 nm of SiO_2 above the silicon layer. A Si_3N_4 layer was then deposited using another PECVD

process, polished to reduce optical scattering loss resulting in a final layer thickness of 200 nm, and patterned using 193 nm immersion lithography. This process was then repeated with a second 100-nm-thick SiO₂ layer and a second 200-nm-thick Si₃N₄ layer. The two resulting Si₃N₄ layers, called the first nitride and second nitride, define the passive Si₃N₄ devices in the system. Additionally, the second-nitride layer was also used as an etch stop for the gain trench.

Above these three waveguide layers, three metal and via layers were formed using a series of additional Si₃N₄ etch stop layers, trenches, metal depositions, and SiO₂ layers. A metal via was used for electrical contact to the silicided regions of the silicon layer, two 1- μ m-thick copper metal layers were patterned to enable routing of electronic signals, copper vias were used for interconnection between the copper metal layers, and a third aluminum metal layer and aluminum vias were used to define pads for electronic probe connection.

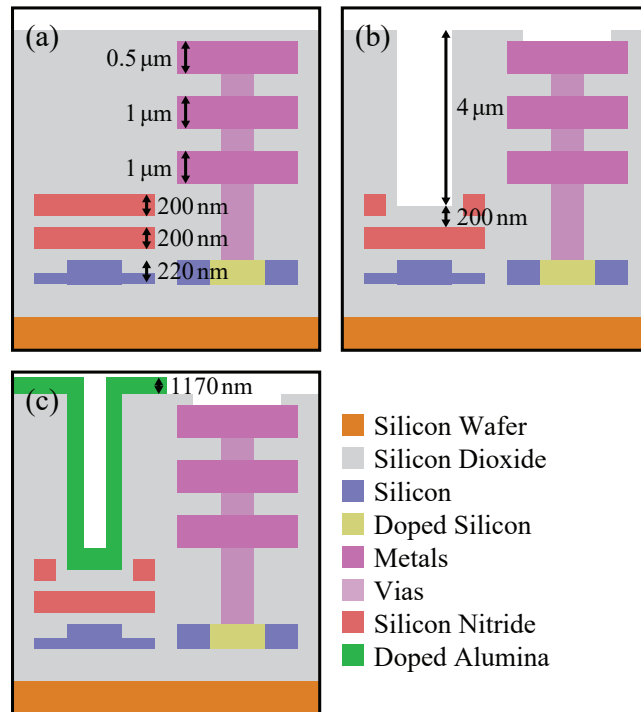


Figure 2.1: Simplified layer schematics of the monolithically-integrated silicon-photonics platform utilized for the phased-array system (a) before the gain trench is etched, (b) after the gain trench is etched, and (c) after the gain film is deposited (not to scale).

Figure 2.1a shows a schematic of the platform at this stage. At this point in the process, the platform resembles a standard multi-layer photonics platform (similar to [61,62]) with measured waveguide losses on the order of 3 dB/cm and 1.5 dB/cm for the silicon and Si₃N₄ waveguides, respectively. (Note that, since PECVD Si₃N₄ was used, the Si₃N₄ waveguide loss increases by about 3 dB around 1520 nm due to residual N-H bonds; this loss could be reduced by optimizing the stoichiometry of the Si₃N₄.)

Next, to enable interaction between a gain material and the waveguide layers in the platform, a trench was formed into which gain material can be deposited. In the majority of prior rare-earth-doped-laser demonstrations [48–54], a gain trench was not used and the gain material was deposited directly on top of passive waveguides using a blanket film approach; this approach enabled strong interaction between the gain material and the waveguide modes, but limited the demonstrations to passive stand-alone devices. By introducing the gain trench, strong interaction between the gain material and the waveguide modes is maintained while simultaneously enabling fabrication of a vertical stack of multiple waveguides, metals, and vias using standard CMOS processes (as discussed in Sec. 2.1.2 above). Specifically, a 4- μ m-deep trench was etched into the SiO₂ using the second-nitride layer as an etch stop. The second-nitride etch stop was then dry etched selectively to the underlying oxide. An additional 100-nm-thick SiO₂ layer was then deposited as a liner within the gain trench, such that the final spacing between the first-nitride layer and the bottom of the trench is 200 nm, as shown in Fig. 2.1b.

Finally, a deep dicing trench was etched to define the edge of each chip and create a smooth facet for fiber edge coupling after dicing, and the oxide above each aluminum pad was removed to create an opening for each pad.

After dicing the wafer into individual reticles, a 1170-nm-thick Al₂O₃:Er³⁺ film was deposited on top of the chip via reactive co-sputtering at MIT [63], as shown in Fig. 2.1c. The gain-film thickness was chosen to ensure high mode overlap and confinement within the film for the pump and signal modes (as discussed in Sec. 2.1.3). Additionally, the deposition temperature was optimized experimentally to ensure that

the silicon contacts in the system did not degrade due to the deposition process and that the laser performance was not sacrificed significantly [48]. Specifically, the temperature was reduced on successive deposition iterations until a change in contact resistance was not measured post deposition. The resulting optimized deposition temperature was measured to be 397°C at the substrate. The background loss of the film was measured to be <0.1 dB/cm. Finally, the Erbium doping concentration was optimized experimentally and estimated to be $1.5 \times 10^{20} \text{ cm}^{-3}$. At the same pump power, a lower doping concentration would lead to lower lasing power due to reduced gain, while a higher doping concentration would lead to lower lasing power due to doped-ion clustering or quenching [64, 65].

2.1.3 Architecture

This advanced platform was used to demonstrate an integrated phased-array system powered by an on-chip laser. The system consists of an optically-pumped on-chip laser, layer-transition and wavelength-filtering devices, and an electrically-steerable integrated optical phased array. Figure 2.2 shows a simplified schematic of the system.

The system uses an on-chip distributed-feedback (DFB) laser [57] as the optical source. The gain waveguide of the DFB laser consists of five Si_3N_4 segments patterned in the first-nitride layer underneath a 30- μm -wide gain trench and $\text{Al}_2\text{O}_3:\text{Er}^{3+}$ film,

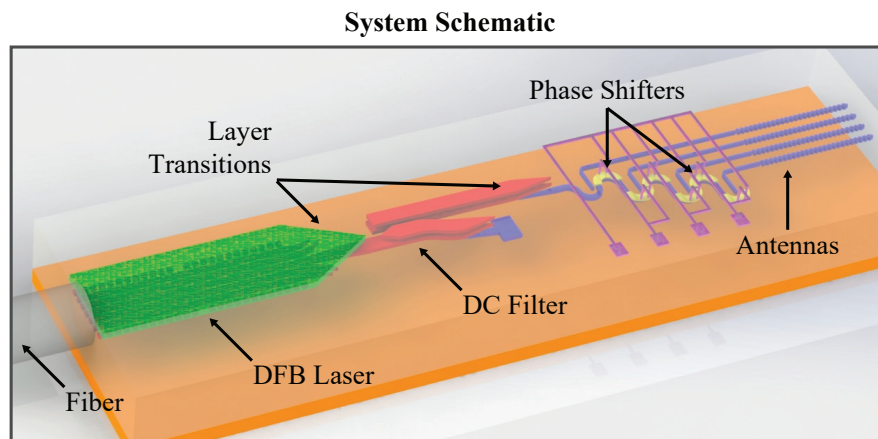


Figure 2.2: Simplified schematic of the phased-array system with an on-chip laser showing major components and process layers (not to scale).

as shown in Fig. 2.3a. The widths of and gaps between the Si_3N_4 pieces were both selected to be 300 nm to ensure high transverse-electric mode overlap and confinement within the gain film for both the 980-nm-wavelength pump and 1599-nm-wavelength signal. The confinement factors in the film were calculated to be 96.9% and 89.8% for the pump and signal modes, respectively, using a two-dimensional mode solver (the simulated mode profiles are shown in Figs. 2.3b–c). The DFB cavity was formed by patterning a 230-nm-wide Si_3N_4 grating in the first-nitride layer along both sides of the gain waveguide, as shown in Fig. 2.3a. To enable a strong single-mode lasing output at the desired signal wavelength, each grating was designed with a 509 nm period, 0.5 duty cycle, 350 nm lateral gap between the gain waveguide and the grating, and quarter-wave gap at the center of the cavity. The total length of the DFB laser is 2 cm, limited by the size of the reticle. Note that variation in the absolute thickness of the gain film will result in a shift of the lasing wavelength [52], whereas variations

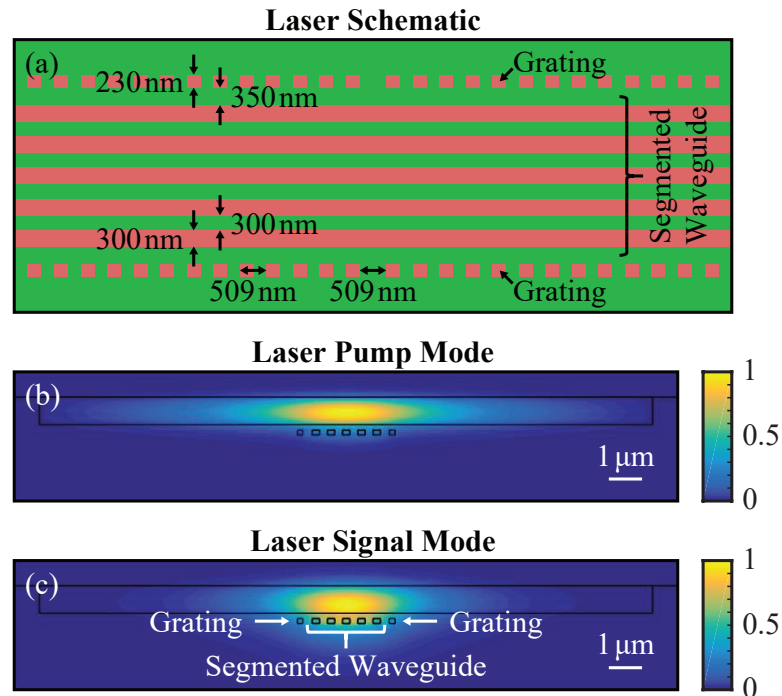


Figure 2.3: (a) Schematic of the center section of the on-chip DFB laser showing the five-segment gain waveguide, gratings, and center gaps. Simulated mode profiles of the (b) 980-nm-wavelength pump and (c) 1599-nm-wavelength signal in the DFB waveguide.

of the gain-film thickness along the length of the laser will affect the quality factor of the cavity [51]; to compensate for radial film-thickness variations, a curved DFB laser could be used [51].

At the far end of the DFB laser, a three-stage 600- μm -long layer transition adiabatically couples the mode from the five-segment gain waveguide under the trench into a 1.2- μm -wide double-layer (first-and-second-nitride) Si_3N_4 waveguide, as shown in Fig. 2.4a. After this layer transition, the 1599 nm signal wavelength is separated from the 980 nm pump using a wavelength-dependent directional coupler (DC). As shown in Fig. 2.4b, the DC acts as a wavelength filter with an approximately 500 nm simulated 3 dB bandwidth and approximately 30 dB simulated signal-to-pump tap-port extinction ratio. The pump output port of the filter is terminated with a doped-silicon block to ensure efficient absorption of any excess pump light. On the signal output port of the filter, another 200- μm -long layer transition adiabatically couples the signal into a 400-nm-wide silicon waveguide connected to the input bus of the

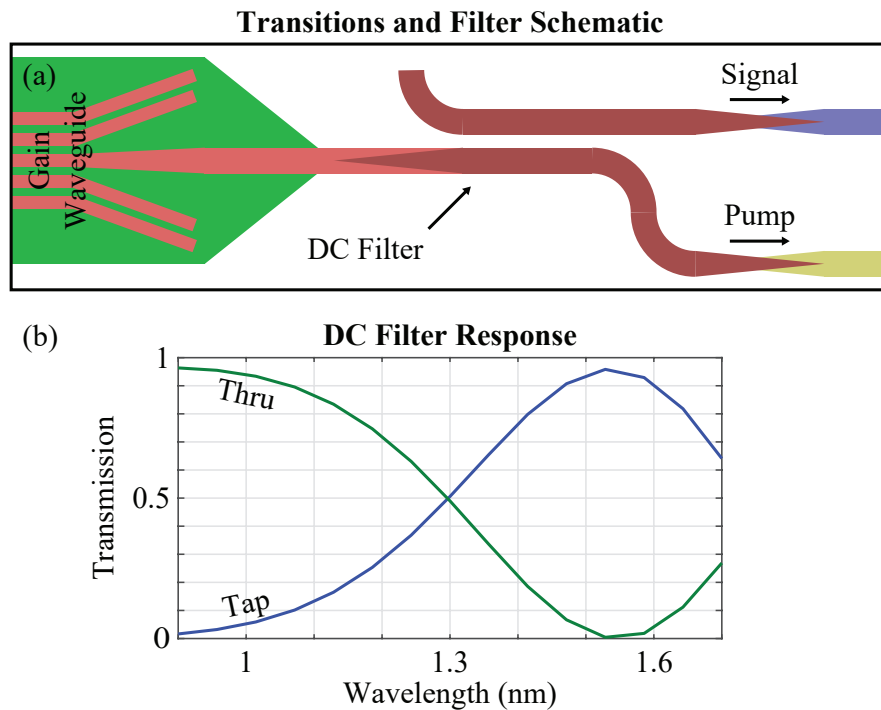


Figure 2.4: (a) Schematic of the layer transitions and DC wavelength filter (not to scale). (b) Simulated transmission versus wavelength for the tap (blue) and thru (green) ports of the DC filter.

integrated phased array with <0.1 dB measured loss, as shown in Fig. 2.4a.

The integrated optical phased array utilizes a grouped cascaded phase-shifter architecture [34], as shown in Fig. 2.5, which controls the relative phases applied to an array of antennas. Evanescent couplers with 120 nm coupling gaps and increasing coupling lengths were used to uniformly distribute the input power from the bus waveguide to 49 grating-based antennas with a $2\text{ }\mu\text{m}$ pitch. Note that the coupling lengths could also be engineered to enable an apodized Gaussian amplitude profile for sidelobe suppression [40]. The antennas utilize a full-etch perturbation geometry (a 64 nm perturbation is etched with a period of 621 nm along the length of the 500- μm -long and 610-nm-wide antennas) to enable radiation out of the plane of the chip at the signal wavelength. A phase shifter was placed on the bus between each evanescent coupler to enable cascaded electronic phase control to the antennas for one-dimensional beam steering. A doped waveguide-embedded thermal phase shifter in an adiabatic-bend configuration was used to ensure thermally-efficient control with low optical loss [40]. The phase shifters are grouped and controlled by 6 electronic signals to reduce control complexity while enabling fine tuning for any fabrication-induced phase variations [34]. Given the $0.5\text{ mm} \times 0.1\text{ mm}$ aperture size and $2\text{ }\mu\text{m}$ antenna pitch, a $0.80^\circ \times 0.16^\circ$ main beam FWHM and grating lobes at $\pm 51^\circ$ are expected in the far field of the array when the main beam is centered at 0° .

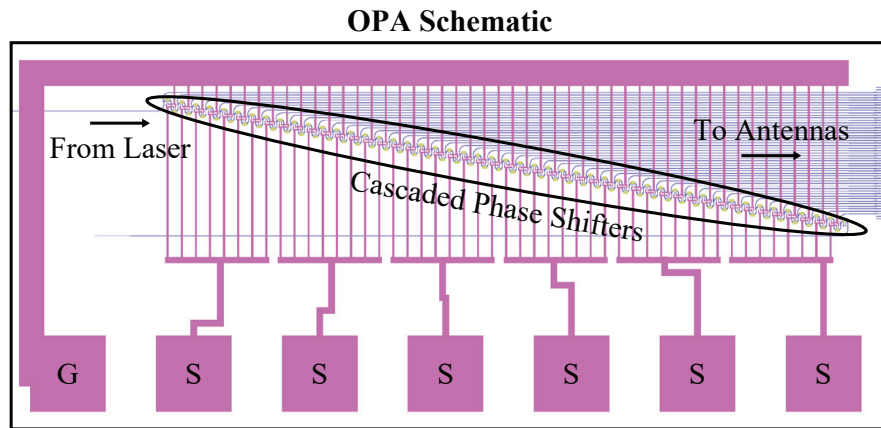


Figure 2.5: Simplified schematic of the cascaded-architecture integrated optical phased array.

2.1.4 Experimental Results

To characterize the fabricated system, an off-chip 980-nm-wavelength laser diode was used for optical pumping, as shown in Fig. 2.6. The pump was routed through a fiber wavelength-division multiplexer (WDM) to enable single-sided characterization of the on-chip laser's signal using either an optical spectrum analyzer (OSA) or a power meter and through a polarization controller to ensure that the transverse-electric mode was coupled into the gain waveguide. The pump was then coupled into the on-chip laser with 254 mW of optical power launched from the input fiber facet (the facet coupling loss was estimated to be 6.2 dB from experiment and was calibrated out). Figure 2.7 shows the normalized laser spectrum, as measured using an OSA. A single lasing peak at 1599 nm with a 30 dB SMSR was observed. Additionally,

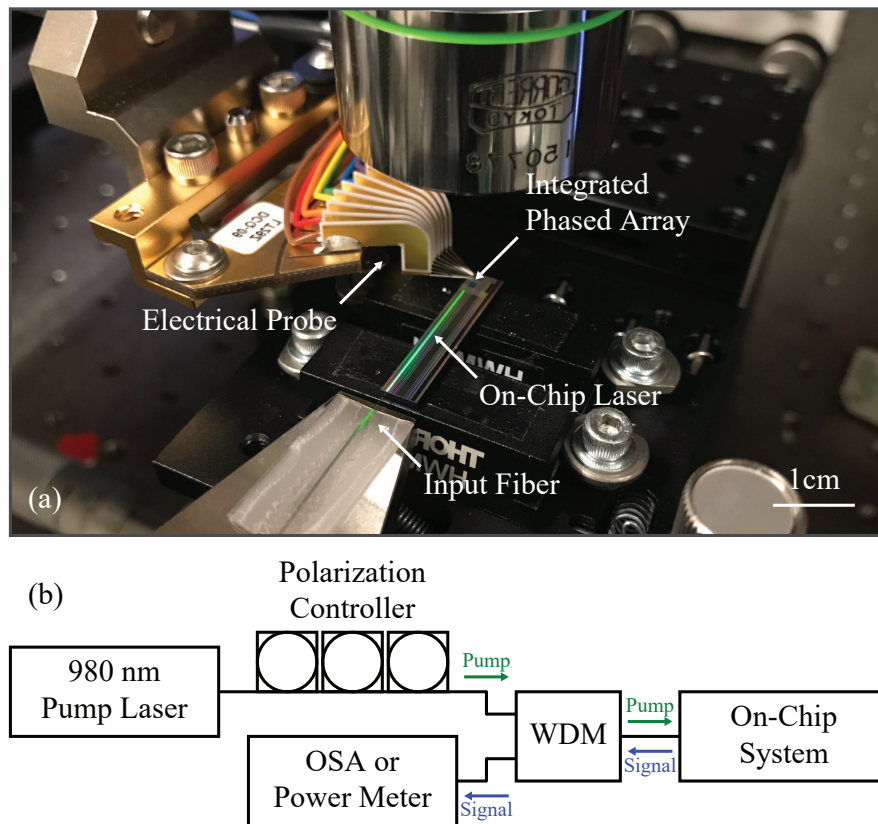


Figure 2.6: (a) Photograph of the fabricated phased-array system with an on-chip laser and the experimental setup. (b) Diagram illustrating the experimental setup used to characterize the on-chip laser.

by varying the input pump power and measuring the resulting signal power using a power meter, the slope efficiency and launch power lasing threshold of the on-chip laser were estimated to be 0.01% and 40 mW, respectively.

Next, a free-space optical setup was utilized to image the far field of the phased array onto an infrared camera. The imaging setup consists of an objective with either a 50° or 16° field of view to serve as a near-to-far-field converter, a singlet lens for magnification, and an InGaAs short-wave-infrared camera [41]. Figure 2.8a shows the measured far-field intensity of the array without fine-tuning optimization. Cross-sectional views of the intensity in the array dimension, Ψ , and the antenna dimension, θ , are shown in Fig. 2.8b. As expected, the system forms a beam in the far field of the array with a measured main-beam FWHM diffraction angle of $0.85^\circ \times 0.20^\circ$, which closely matches both the theoretical value of $0.80^\circ \times 0.16^\circ$ and the $0.85^\circ \times 0.18^\circ$ experimental value previously reported using a similar stand-alone phased array [34]. Note that the far-field pattern could be further improved by utilizing the fine tuning capabilities of the grouped architecture. Additionally, the loss of the system (launched on-chip pump power to radiated main-lobe power) was measured to be approximately 48 dB. Approximately 40 dB of this loss is attributed to the laser, while the remaining 8 dB is largely account for by the power radiated to the higher-order grating lobes, in addition to the minimal losses induced by the layer transitions, phase shifters, and evanescent couplers.

Finally, a multi-pin electrical probe was used to vary the electrical power applied

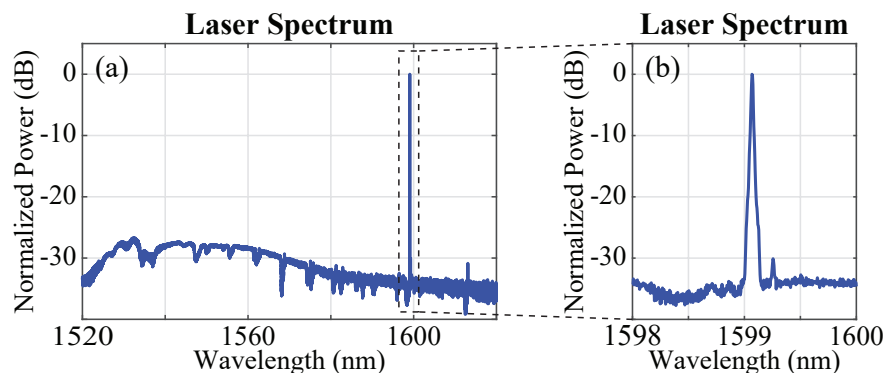


Figure 2.7: Measured optical spectrum of the on-chip laser showing (a) the full spectrum including the amplified spontaneous emission and (b) the lasing peak at 1599 nm.

across the integrated phase shifters in the array and steer the generated beam in the far field. With 0.5 W of applied electrical power, 15° of steering in the array dimension, Ψ , was observed, as shown in Fig. 2.8c. This closely matches the thermal steering efficiency observed previously for a similar stand-alone phased array without gain-film deposition [34], confirming that the film deposition procedure did not detrimentally affect the silicon contact integrity.

2.1.5 Conclusion

In summary, an advanced CMOS-compatible 300-mm-wafer silicon-photonics platform with monolithically-integrated laser sources was developed. The platform was used to demonstrate a complex system of an electrically-steerable integrated optical phased array with a grouped cascaded phase-shifter architecture powered by an on-chip erbium-doped DFB laser. Lasing with a single-mode 1599-nm-wavelength

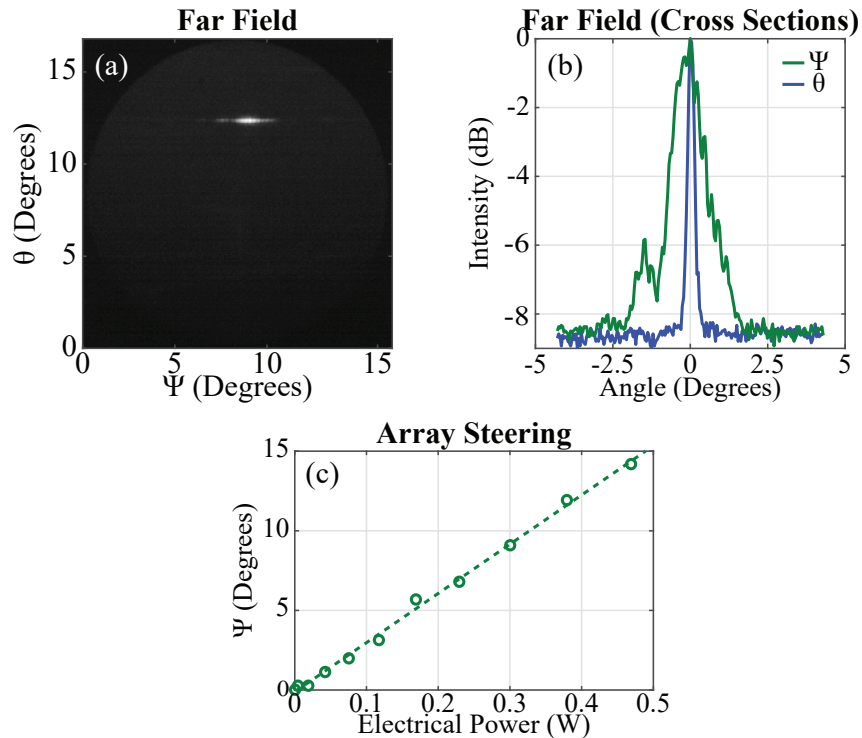


Figure 2.8: (a) Measured far field above the chip showing the main lobe of the phased array. (b) Intensity cross sections of the far-field main lobe in the array dimension (green) and the antenna dimension (blue). (c) Experimental results showing beam steering in the array dimension, Ψ , versus applied electrical power.

output, 30 dB SMSR, and 40 mW lasing threshold was shown. Beam forming and one-dimensional beam steering with a $0.85^\circ \times 0.20^\circ$ FWHM and $30^\circ/\text{W}$ electrical steering efficiency were demonstrated. This system enables integrated CMOS-compatible beam steering capabilities for a variety of applications, ranging from LiDAR to free-space optical communications [34, 36].

Furthermore, this work represents the first demonstration of a monolithic rare-earth-doped laser source integrated into an active SOI photonics system. The successful realization of such a platform paves the way for future advanced monolithic silicon-photonics demonstrations, ranging from integrated communication links [30, 58] to on-chip optical synthesizers [26, 59].

For future improvements to this system, first, a laser source with a tunable wavelength output (similar to [27]) could be implemented to enable steering of the far-field spot in the antenna dimension (since the antennas in the phased array are based on grating principles, as the wavelength of the input light is tuned, the effective period of the antennas and, subsequently, the angle of the radiated light varies). Second, the relatively low slope efficiency of the current on-chip laser compared to previous reports [50] is largely attributed to the loss induced by the roughness at the bottom of the gain trench due to voids in the first-nitride cladding oxide. To improve the overall system performance, an updated oxide cladding recipe will be used to ensure higher quality gap fill, reduced trench roughness and loss, and improved laser efficiency. To further improve the overall system efficiency, a number of additional modifications could be implemented, including using a tighter pitch and improved design for the antennas in the phased array to reduce the power radiated to the higher-order grating lobes [36], refining the layer transitions for increased efficiency, and implementing advanced laser designs with enhanced grating performance to enable higher laser output powers [50]. Third, the input optical pump could be packaged with the integrated chip by leveraging recent advances in photonics packaging [66]. Fourth, to enable high-speed beam steering with lower drive power, the thermo-optic phase shifters in the phased array could be replaced with high-speed and low-power electro-optic phase shifters [36]; this would be a straightforward modification since customizable doping

masks are already present in the developed platform. Fifth, the CMOS compatibility of the system could be leveraged to enable either monolithic or heterogeneous integration with driving CMOS electronics (as discussed in Sec. 2.2) [9, 42, 43].

2.2 Integrated Optical Phased Arrays with 3D-Integrated Electronics

The following work was led by Taehwan Kim (UC Berkeley) and Pavan Bhargava (UC Berkeley) and done in collaboration with Christopher V. Poulton (MIT), Ami Yaacobi (MIT), Erman Timurdogan (MIT), Christopher Baiocco (SUNY Poly), Nicholas M. Fahrenkopf (SUNY Poly), Seth Kruger (SUNY Poly), Tat Ngai (SUNY Poly), Yukta Timalsina (SUNY Poly), Michael R. Watts (MIT), and Vladimir Stojanovic (UC Berkeley). A brief summary of the work is included in this section for completeness; additional details can be found in [9–11].

2.2.1 Introduction

As discussed in Sec. 2.1, integrated optical phased arrays have emerged as a promising solution for next-generation light detection and ranging (LiDAR) sensors for autonomous systems, since they enable optical beam steering in a compact form factor, at low costs, and in a non-mechanical way [36, 41, 67].

However, the majority of prior integrated-optical-phased-array demonstrations have been limited to systems controlled by off-chip discrete electronics [36, 41, 67]. This limits the scalability and practicality of these systems, especially as the number of antenna elements (and corresponding electronic control signals) increases to meet the small spot size, large directivity, and wide steering range requirements necessary for LiDAR applications.

To improve the scalability and practicality of these systems, monolithic integration of integrated optical phased arrays with CMOS driving electronics has been explored [42, 68]. However, monolithic integration results in (1) limitations on the performance of the photonic components due to constraints placed by CMOS design rules and available materials and (2) larger die footprints and reduced photonics fill factors due to placement and routing constraints.

In this section, the first beam-steering optical phased array heterogeneously inte-

grated with CMOS driving electronics [9,10] and the first single-chip coherent LiDAR with integrated optical phased arrays and CMOS receiver electronics [11], both in a novel 3D-integrated electronics-photonics platform, will be reviewed. This 3D integration scheme allows for (1) the photonics and electronics to be independently fabricated, which enables introduction of custom materials and processes for the photonics (such as Germanium for photodetectors) while simultaneously utilizing the most advanced CMOS nodes for the electronics, and (2) flexible and dense vertical interconnections between the photonics and electronics, which reduces wiring overhead, increases the photonics fill factor, and maintains bandwidth performance. These demonstrations are important steps towards scalable and practical commercialization of low-cost and high-performance integrated LiDAR sensors for autonomous systems.

2.2.2 Platform

The beam-steering optical phased array heterogeneously integrated with CMOS driving electronics and the single-chip coherent LiDAR with integrated optical phased arrays and CMOS receiver electronics were both fabricated at SUNY Poly in a novel 3D-integrated electronics-photonics platform [69], as shown in Fig. 2.9a.

In the developed platform, the photonic components were fabricated in a custom 300-mm-wafer silicon-photonics platform (as described in Sec. 2.1), while the electronic circuits were fabricated separately in a 65 nm bulk CMOS technology. The two 300-mm-diameter wafers were then oxide bonded and the silicon handle on the photonics wafer was removed using a global etch. Next, through-oxide vias (TOVs) and a back metal layer were formed to enable interconnection between the photonics and electronics and to define pads for wirebonding. Finally, the resulting wafer was diced and a diced chip was wire bonded to a ceramic package, as shown in Figs. 2.9b–c.

2.2.3 OPA Architecture and Experimental Results

The 3D-integrated platform was first used to demonstrate a beam-steering optical phased array heterogeneously integrated with CMOS driving electronics.

The integrated optical phased array utilizes a cascaded phase-shifter architecture [34], as shown in Fig. 2.10. At the input, an on-chip inverse-taper edge coupler couples light from an off-chip laser into an on-chip single-mode silicon bus waveguide. Cascaded evanescent couplers with increasing coupling lengths uniformly distribute the input light from the bus waveguide to 32 500- μm -long antennas with a 4 μm pitch. The antennas utilize a sidewall-grating-based geometry with apodized scattering strength to enable radiation out of the plane of the chip with a uniform

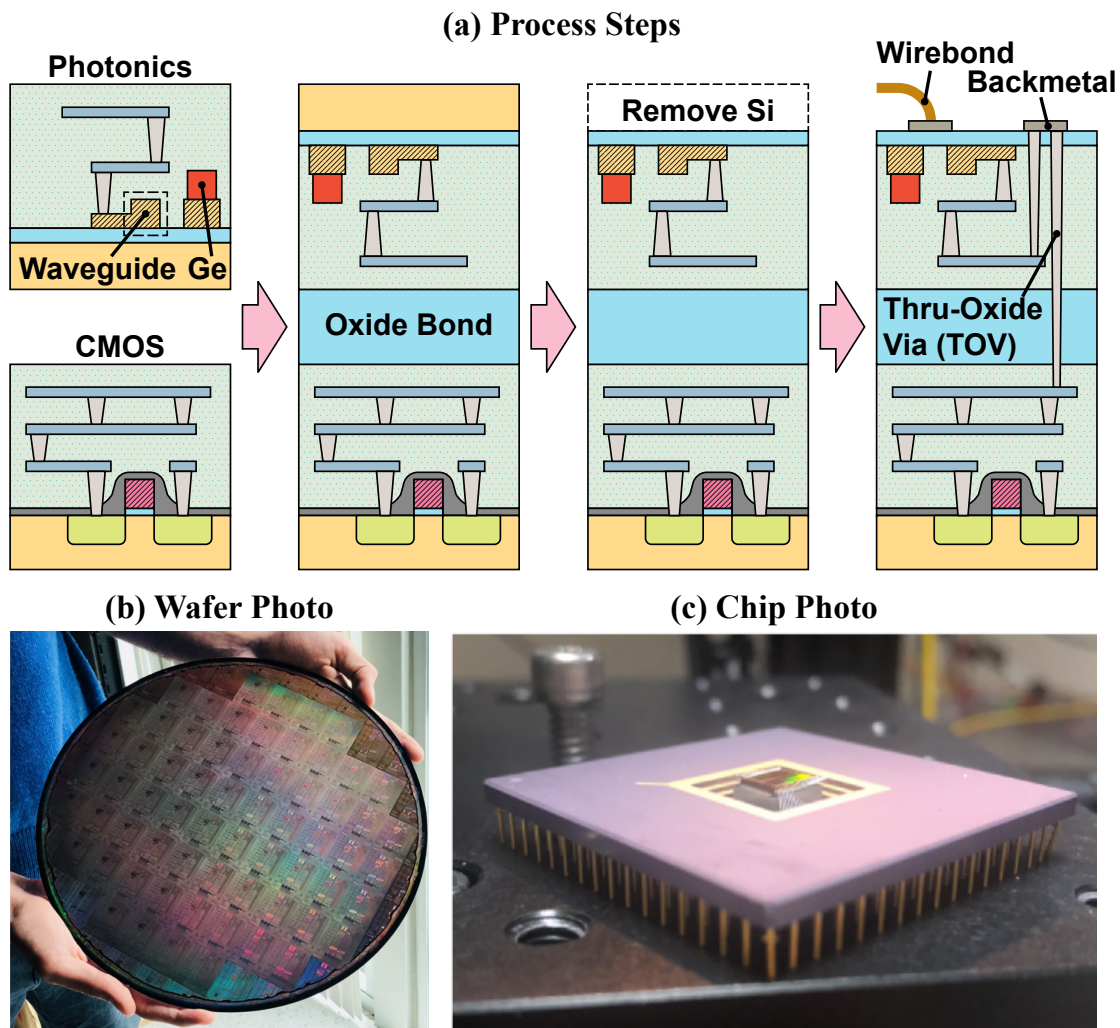


Figure 2.9: (a) Simplified layer schematics showing the key process steps of the 3D-integrated electronics-photonics platform (not to scale). Photographs of (b) the fabricated 3D-integrated 300-mm-diameter wafer and (c) the packaged 3D-integrated chip. (Figures from [9–11].)

emission profile and wavelength-controlled beam steering in the antenna dimension, ϕ . Thermal ridge-waveguide-based phase shifters are placed on the bus between the evanescent couplers to enable cascaded electronic phase control to the antennas for beam steering in the array dimension, θ . The phase shifters are controlled using inte-

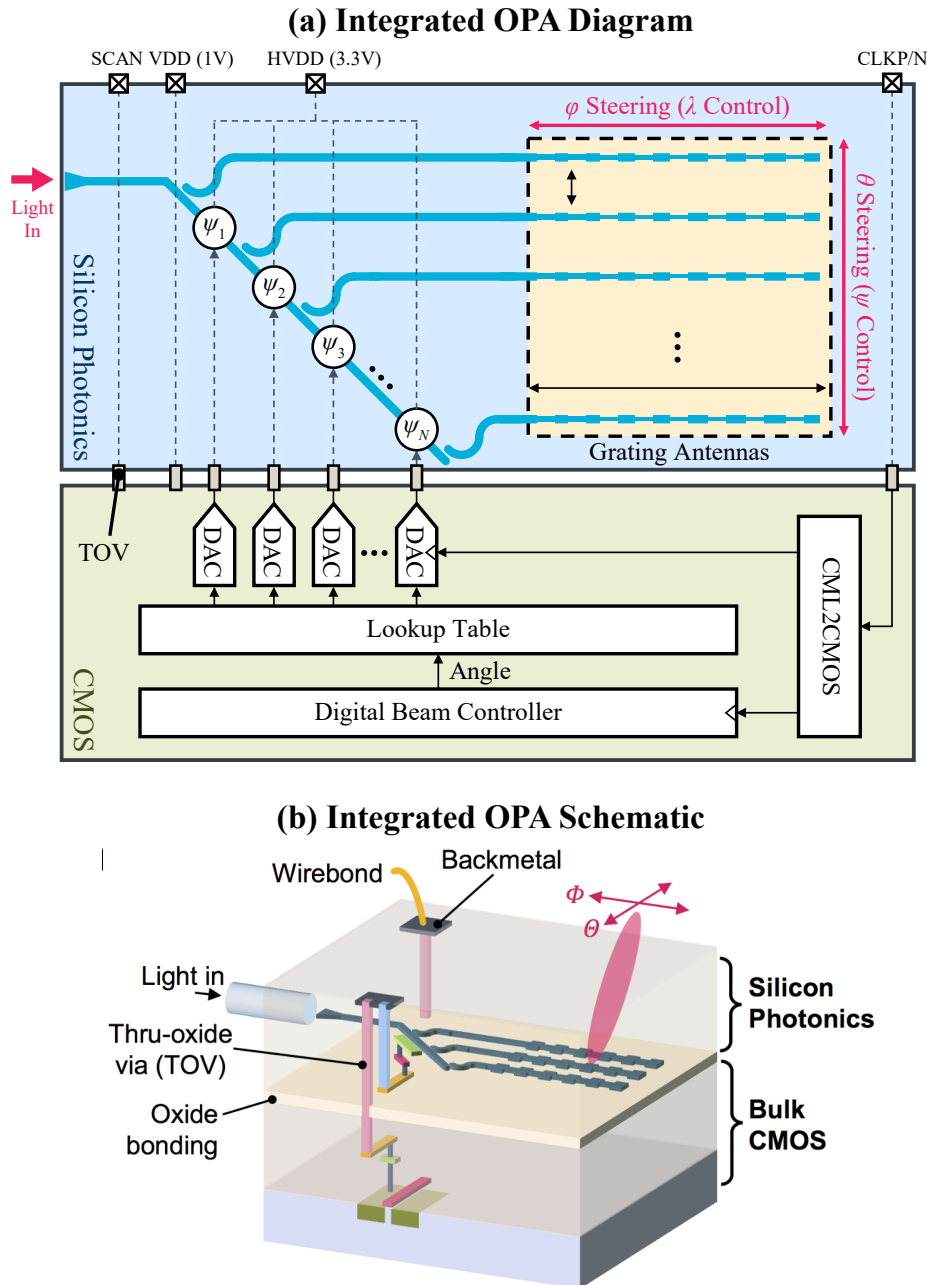


Figure 2.10: Simplified (a) diagram and (b) schematic (not to scale) of the cascaded-architecture integrated optical phased array with integrated CMOS driving electronics. (Figures from [9].)

grated CMOS driving electronics with individual digital-to-analog converters (DACs) for each phase shifter and an on-chip lookup table for storing the associated DAC codes.

To characterize the fabricated array, an off-chip tunable laser was coupled onto the chip, a free-space optical system was used to image the far field of the array onto an infrared camera, and the array was calibrated by optimizing the DAC codes for each phase shifter. The experimentally measured far-field patterns before and after calibration are shown in Figs. 2.11a–b. As shown, after calibration, the array forms a high-fidelity beam in the far field with a $0.60^\circ \times 0.15^\circ$ power full width at half maximum and 8.5 dB sidelobe suppression. Next, the DAC codes were updated and the wavelength of the input tunable laser was varied to demonstrate the two-dimensional

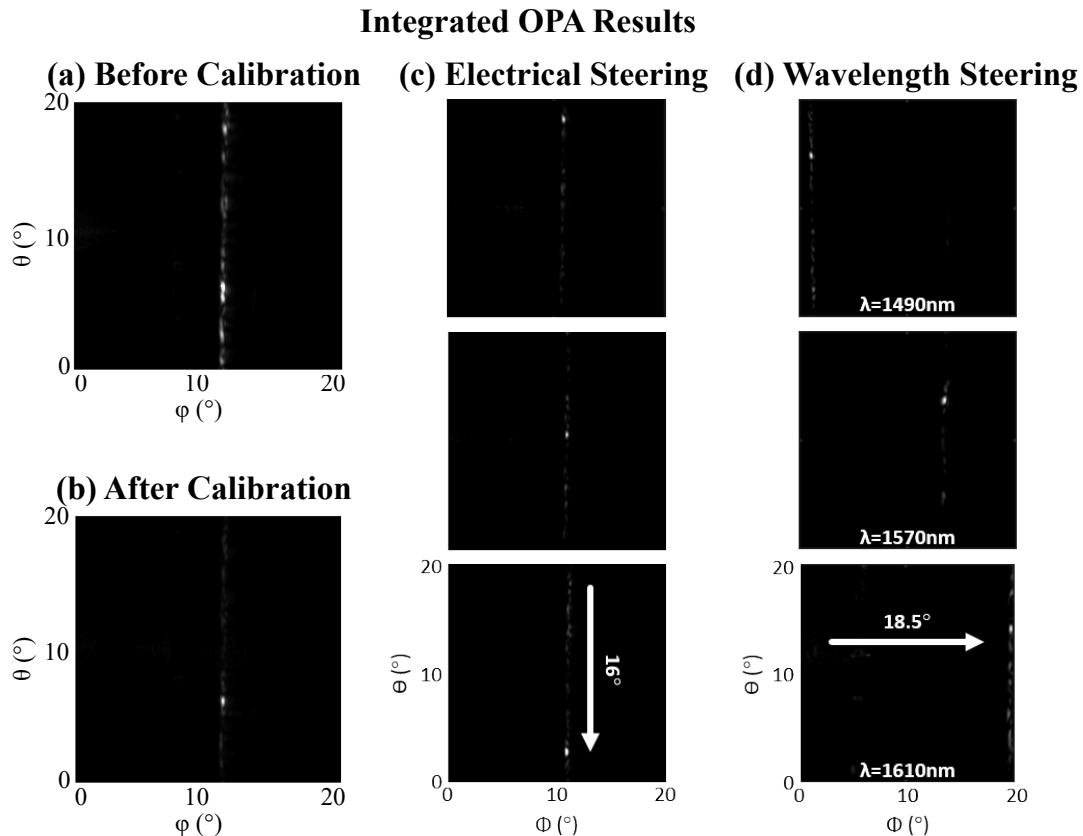


Figure 2.11: Measured far field above the packaged chip showing the main lobe of the integrated optical phased array (a) before and (b) after calibration. Experimental results showing beam steering in the (c) array dimension, θ , and (d) antenna dimension, ϕ . (Figures from [9].)

beam steering functionality of the array. Experimentally measured far-field patterns for a variety of DAC codes and input wavelengths are shown in Figs. 2.11c–d. As shown, beam steering of 16° and 18.5° was achieved in the array dimension, θ , and antenna dimension, ϕ , respectively.

2.2.4 LiDAR Architecture and Experimental Results

Next, the 3D-integrated platform was used to demonstrate a single-chip coherent LiDAR system with integrated optical phased arrays and CMOS receiver electronics.

The integrated coherent LiDAR system is based on a frequency-modulated continuous-

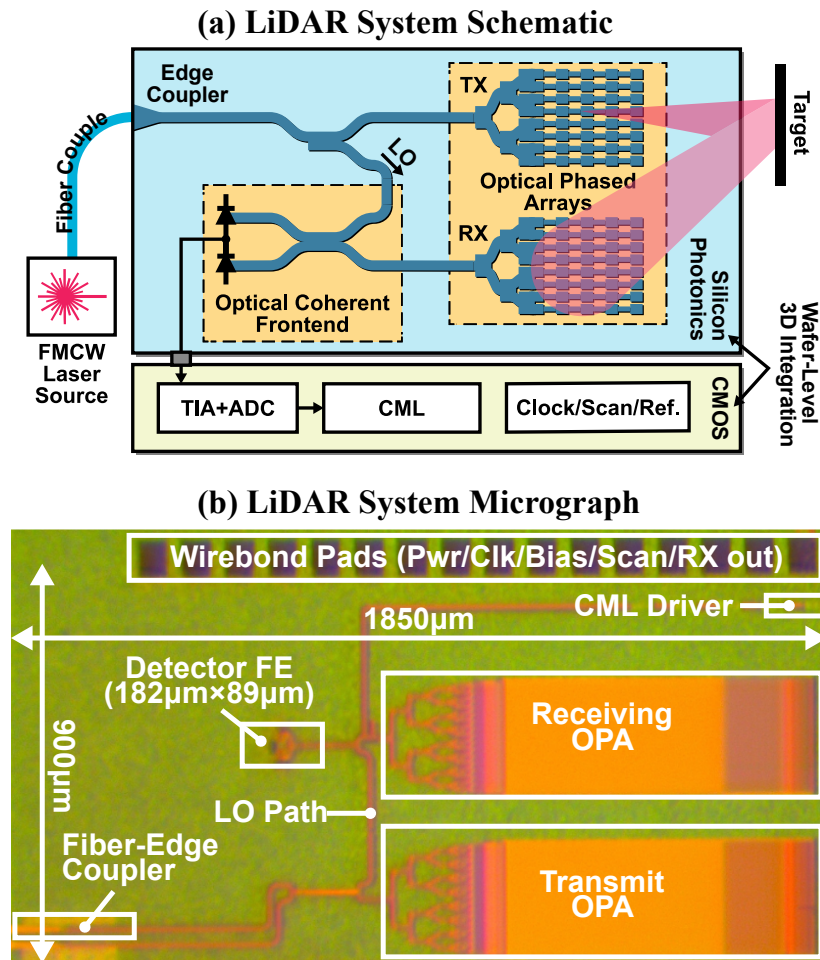


Figure 2.12: (a) Simplified diagram of the integrated coherent LiDAR system with integrated optical phased arrays and integrated CMOS receiver electronics. (b) Micrograph of the fabricated integrated coherent LiDAR system. (Figures from [11].)

wave (FMCW) operating modality [34], as shown in Fig. 2.12. At the input, an on-chip inverse-taper edge coupler couples light from an off-chip FMCW swept laser source (an external-cavity laser with injection current modulated using a triangular waveform with a 9 THz/s sweep rate) into an on-chip single-mode silicon waveguide. An adiabatic coupler then taps off half of the input light to serve as the local oscillator. The remainder of the light is emitted out of the plane of the chip into free space by a passive transmitting integrated optical phased array consisting of a 7-layer multi-mode-interference (MMI) splitter tree and 128 500- μm -long grating-based antennas with a 2 μm pitch [70]. The transmitted light is then reflected off of a target and received by a similar receiving passive integrated optical phased array. The received

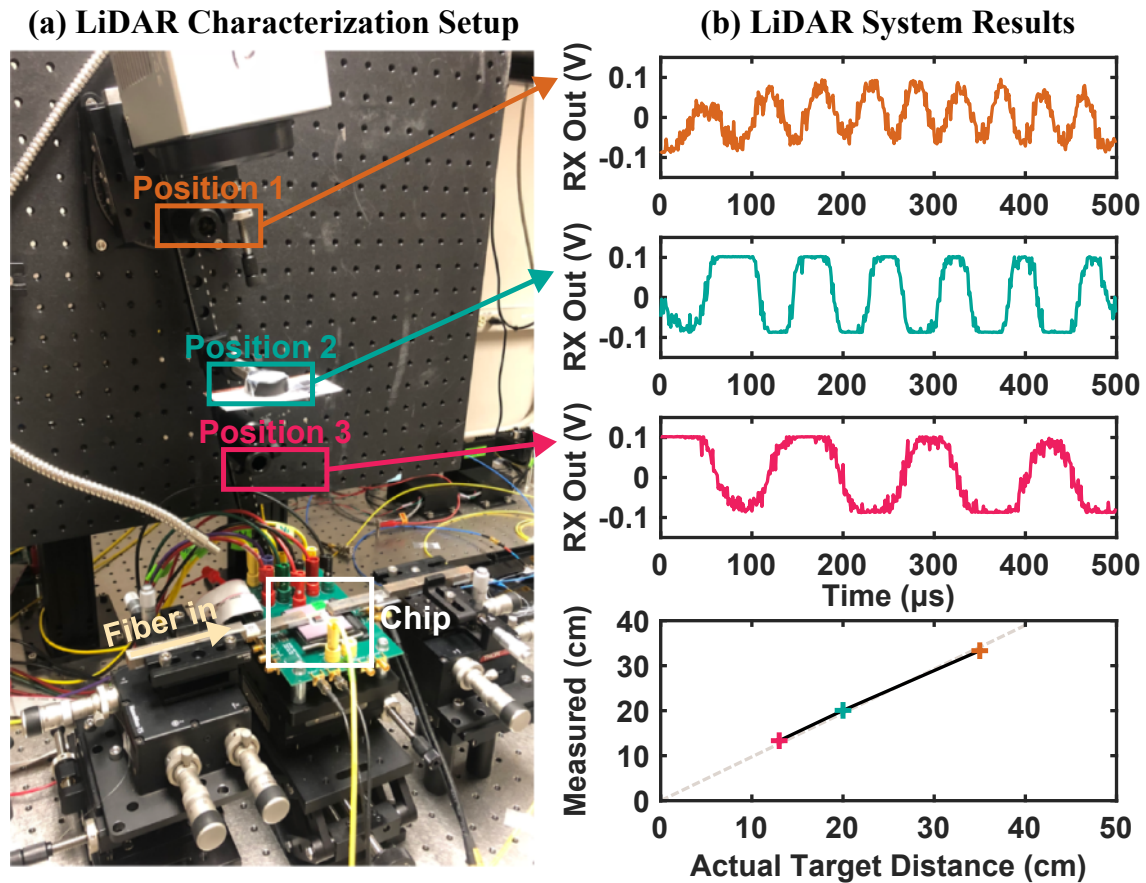


Figure 2.13: (a) Photograph of the LiDAR characterization setup showing the packaged integrated coherent LiDAR chip and three target positions. (b) Experimental results showing the raw receiver output signals and corresponding post-processed measured versus actual target distances for each of the three target positions. (Figures from [11].)

signal is then mixed with the local oscillator using a second adiabatic coupler and a germanium-based balanced photodetector. Finally, the output photocurrent is amplified and digitized by an integrated transimpedance amplifier and analog-to-digital converter.

To demonstrate the ranging functionality of the fabricated system, a target constructed out of reflective tape was placed at three different positions above the packaged integrated coherent LiDAR chip, as shown in Fig. 2.13a. The raw receiver output signals and corresponding post-processed measured versus actual target distances for each of the three target positions are shown in Fig. 2.13b.

2.2.5 Conclusion

In summary, a novel 3D-integrated electronics-photonics platform was developed that enables photonics and CMOS electronics to be independently optimized and scaled, while maintaining dense interconnections. This 3D-integrated platform was used to demonstrate the first beam-steering optical phased array heterogeneously integrated with CMOS driving electronics and the first single-chip coherent LiDAR with integrated optical phased arrays and CMOS receiver electronics. These demonstrations are important steps towards scalable and practical commercialization of low-cost and high-performance integrated LiDAR sensors for autonomous systems.

Chapter 3

Near-Field Integrated Optical Phased Arrays

Motivated by the initial application of LiDAR, integrated-optical-phased-array demonstrations to date have primarily focused on systems that form and steer beams in the far field of the array (as discussed in Ch. 2). However, there are many high-impact application areas that require near-field optical manipulation that would greatly benefit from the compact form factors and large standoff distances enabled by integrated optical phased arrays, such as optical trapping for biological characterization, trapped-ion quantum computing, laser-based 3D printing, and short-range LiDAR and data communications.

A variety of integrated optical phased arrays with novel components, architectures, and functionalities for optical manipulation in the near field will be reviewed. First, the first integrated optical phased arrays that focus radiated light to tightly-confined spots in the near field will be discussed [12, 13]; this focusing modality has the potential to advance a number of important application areas, such as optical trapping for biological characterization, trapped-ion quantum computing, laser-based 3D printing, and short-range LiDAR and data communications. Second, the first demonstration of a quasi-Bessel beam generated using an integrated optical phased array will be shown [14, 15]; owing to its elongated central beam output, this chip-based

Bessel-beam generator has applications in a range of fields, including multiparticle optical trapping, increased-depth-of-field microscopy, and adaptive free-space optical communications. Third, an active scalable two-dimensional integrated optical phased array architecture with cascaded butterfly-shaped pixels will be presented [16,17]; this novel architecture enables compact, in-line independent amplitude and phase control with power recycling for space- and power-efficient near-field operation.

3.1 Near-Field-Focusing Integrated Optical Phased Arrays

The following work was done in collaboration with Christopher V. Poulton (MIT), Manan Raval (MIT), and Michael R. Watts (MIT). This work has been published in [12, 13].

3.1.1 Introduction

As discussed in Ch. 2, integrated optical phased arrays [14, 34–37, 40, 41, 70–74] have emerged as a promising technology for many applications, such as light detection and ranging (LiDAR) [34], projection systems [35], and free-space optical data communications [36], due to their ability to manipulate and dynamically steer light in a compact form factor, at low costs, and in a non-mechanical way. Motivated by these initial applications, optical phased array demonstrations to date have primarily focused on systems that form and steer beams or project arbitrary radiation patterns in the far field of the array [34–37, 40, 41, 70–73].

However, many potential applications of optical phased arrays require focused spots in the near field of the array (as typically generated by bulk-optics lenses) instead of diffracting beams or patterns in the far field (as generated by standard phased arrays). For example, optical trapping and tweezing – the manipulation of particles through non-contact forces for biological characterization [75–77] and trapped ion quantum computing [78] – require tightly-focused spots since optical forces are formed due to intensity gradients. Similarly, high-resolution three-dimensional printing using laser-based additive manufacturing is dependent on high-intensity focused spots to enable small voxel sizes [79]. Furthermore, for short-range LiDAR or data communications with targets or receivers within the near-field of the transmitter array, focusing the signal on the object under test or receiver as opposed to forming a diffracting beam in the direction of the target would improve the overall system efficiency.

Typically, focusing beams have been generated using free-space methods, such as conventional and Fresnel bulk-optics lenses, focusing spatial light modulators [80], and metamaterial-based lenses [81], which generally provide diffraction-limited spots at a variety of designed focal lengths. However, these numerous potential applications would benefit from the waveguided compact form-factors [37], low-cost wafer-scale production [34], monolithically-integrated light sources [7], and high-speed dynamic steering capabilities [35] that focusing integrated optical phased arrays could provide while maintaining required performance with large aperture sizes (and, consequently, large focal lengths and small spot sizes) [70].

In this section, Fresnel-lens-inspired focusing integrated optical phased arrays are demonstrated for the first time. Foremost, the phase distributions necessary for generating focused beams are derived, and discussion and simulations detailing the effect of the array aperture and focal length on the full width at half maximum (FWHM) of the focal spot are included. Additionally, the effect of conventional linear steering on the focal length is shown and a modified non-linear steering phase is derived. Next, two architectures are proposed for experimentally demonstrating focusing integrated optical phased arrays. First, a one-dimensional (1D) splitter-tree-based phased array architecture [70] is modified to enable passive near-field focusing in two dimensions. The architecture consists of a 1D splitter tree to evenly distribute the input light to the antenna array, a novel phase bump device before each antenna to passively encode arbitrary phase distributions to the elements of the array and enable focusing in the array dimension, and the first millimeter-scale focusing grating-based antennas to enable focusing in the antenna dimension. This splitter-tree-based architecture is implemented to demonstrate a 512-antenna integrated phased array with a $1.024 \text{ mm} \times 0.9 \text{ mm}$ aperture that focuses light down to a $\sim 7 \text{ }\mu\text{m}$ spot 5 mm above the chip. Additionally, experimental data showing wavelength steering of the focal spot in the antenna dimension is shown and discussion on extension of the architecture to electronic control in the array dimension is presented. Next, a two-dimensional (2D) pixel-based architecture [71] is utilized to show a second type of passive focusing phased array with the potential for active electronic focusing in two dimensions.

This pixel-based architecture consists of a 2D grid of pixels with each pixel passively encoding the amplitude and phase of the light radiated by a compact antenna emitter using a directional coupler and a waveguide offset, respectively. Specifically, a 1024-antenna variant with 32 rows by 32 columns and a $0.32\text{ mm} \times 0.32\text{ mm}$ aperture is demonstrated that focuses light to a $\sim 21\text{ }\mu\text{m}$ spot 5 mm above the chip, and a 10,000-antenna variant with 100 rows by 100 columns and a $1\text{ mm} \times 1\text{ mm}$ aperture is demonstrated that focuses light to a $\sim 21\text{ }\mu\text{m}$ spot 10 mm above the chip. By using a CMOS-compatible platform for both architectures, the systems are naturally scalable to active demonstrations with wafer-scale 3D-bonded electronics [9] and monolithically-integrated lasers [7] (as discussed in Ch. 2) for a fully-integrated and steerable chip-based source of focused light.

3.1.2 Theory

In general, a phased array is a system comprised of an array of antennas that are fed with controlled phases and amplitudes (as shown in Fig. 3.1a) to generate arbitrary radiation patterns. If the antennas are spaced with a uniform pitch, d , and fed with a uniform amplitude and a linear phase distribution, the array creates a steerable, diffracting beam in the far field of the array. The near-field electric-field profile generated by this phased array can be approximated using a quasi-array-factor model for the near field (analogous to standard array-factor simulations in the far field):

$$E(x, y, z) = \sum_{n=1}^N E_n(x, y, z) \approx \sum_{n=1}^N A_n e^{-i(2\pi r_n/\lambda + \Phi_n)} \quad (3.1)$$

where N is the total number of antennas in the array, A_n is the amplitude applied to the n th antenna, Φ_n is the phase applied to the n th antenna, r_n is the distance from the n th antenna to the point under consideration at coordinate (x, y, z) , and λ is the propagation wavelength. Using this method, a standard array with $N = 512$, $d = 2\text{ }\mu\text{m}$, and $\lambda = 1550\text{ nm}$ is simulated; the generated intensity profile is shown in Fig. 3.2a.

In contrast, if a “lens-like” hyperbolic element phase distribution is applied, the ar-

ray will focus light into a tightly-confined spot in the near field above the array. This element phase is derived by calculating the relative delay necessary such that constructive interference of the wavefronts occurs at the focal point. First, the distance from each antenna to the focal point is calculated as:

$$L_n = \sqrt{f_z^2 + d^2 (N/2 + 1/2 - n)^2} \quad (3.2)$$

where f_z is the desired focal length. To enforce the focusing condition, the phase applied to each antenna should compensate for the differences in the corresponding optical path lengths such that the wavefronts at the focal point constructively interfere. This gives the desired feeding phase distribution

$$\Phi_n = \frac{2\pi}{\lambda} (L_1 - L_n). \quad (3.3)$$

Similarly to a Fresnel lens, this phase can be encoded modulo 2π , as shown in Figs. 3.1b–c. This wrapped phase encoding is utilized so that any potential fabrication-induced phase variations in the array will not compound over more than 2π . As such, the system is very robust to phase variations in the array dimension; variations will result in minimal power loss in the focal spot as opposed to causing displacement

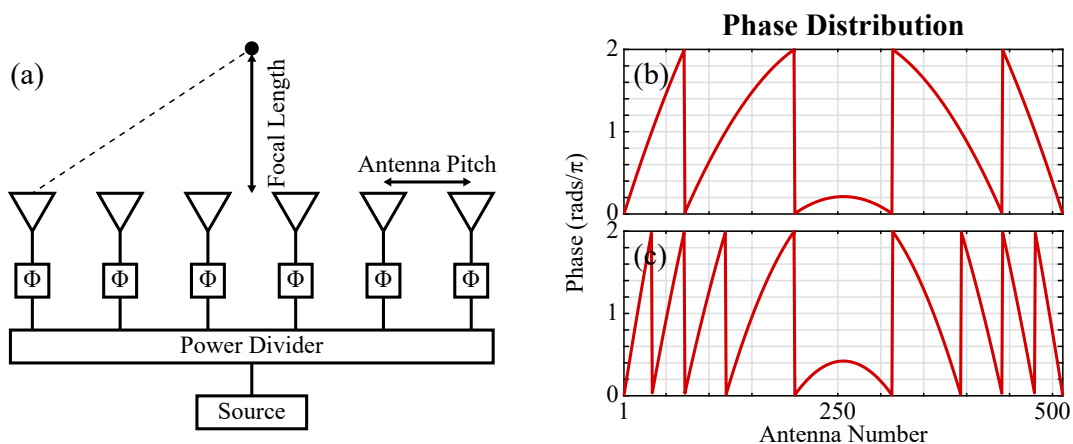


Figure 3.1: (a) Schematic of a generalized focusing phased array showing the antenna pitch and focal length. Element phase distribution for a focusing phased array with (b) 40 mm and (c) 20 mm focal length assuming 512 antennas, 2 μm antenna pitch, and 1550 nm wavelength.

of the spot. Additionally, the wrapped phase encoding requires less relative phase difference between antennas, which enables shorter, smaller, and more-fabrication-tolerant phase delay structures for both splitter-tree-based and pixel-based phased array architectures.

Figures 3.2b–d show the simulated intensity profiles generated by two focusing phased arrays with $N = 512$, $d = 2 \mu\text{m}$, $\lambda = 1550 \text{ nm}$, and varying focal lengths. As shown, by applying the derived element phase profiles, the arrays focus light to tightly-confined and highly-enhanced spots. Additionally, due to discretization of the continuous theory onto arrays with $d > \lambda/2$, higher-order grating lobes, which also exhibit focusing properties, are generated by the arrays at larger angles (not shown in the simulation windows).

For appreciable focusing, the desired focal length of a focusing array should be limited to the Fresnel region (i.e., the near field) of the phased array, $r_{\text{near}} \approx A^2/\lambda$ where $A = Nd$ is the array aperture size, as given by antenna theory. Consequently, by increasing the aperture size, the possible focal length of the array quadratically

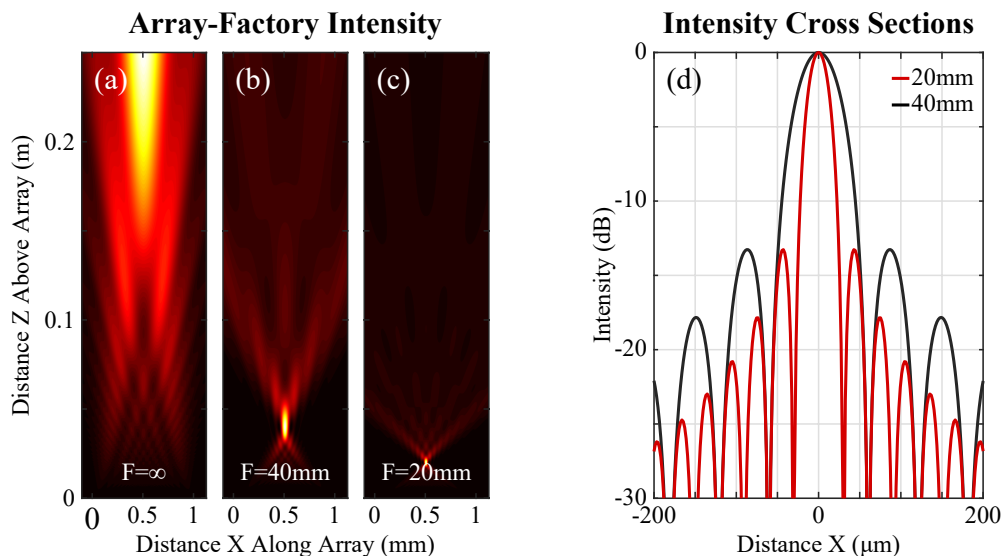


Figure 3.2: Simulated array-factor intensity above the array for a (a) non-focusing, (b) 40 mm focal length, and (c) 20 mm focal length phased array. (d) Simulated cross-sectional array-factor intensity at the focal plane for the 40 mm focal length (black) and 20 mm focal length (red) phased array. Simulated intensities are shown for an array with 512 antennas, $2 \mu\text{m}$ antenna pitch, and 1550 nm wavelength.

increases.

Additionally, for potential applications that require highly-enhanced and tightly-focused spots, a valuable figure of merit of a focusing array is the power FWHM of the resulting spot at the desired focal length. For example, for a 512-antenna array with $2\ \mu\text{m}$ antenna pitch at a $1550\ \text{nm}$ wavelength, as simulated in Figs. 3.2b–d, the FWHM is found to be $53.5\ \mu\text{m}$ and $26.6\ \mu\text{m}$ for focal lengths of $40\ \text{mm}$ and $20\ \text{mm}$, respectively.

Similarly to bulk lenses, the FWHM depends on the aperture size of the array and the focal length. As shown in Fig. 3.3a, as the array aperture size increases, the FWHM decreases with an inverse scaling. In contrast, as shown in Fig. 3.3b, as the desired focal length increases, the FWHM increases linearly. These relationships match with the well-known Rayleigh criterion derived from the Airy pattern, which describes the resolution limit of an imaging system as $R \approx \lambda f_z / A$ where R is the spatial resolution (analogous to the FWHM). As such, for maximally-enhanced focusing at long focal lengths, large aperture sizes are necessary.

One advantage of using integrated optical phased arrays for focused-light applications is that phased arrays allow for dynamic steering on-chip to enable high-speed arbitrary manipulation. In a standard phased-array system, a linear phase gradient

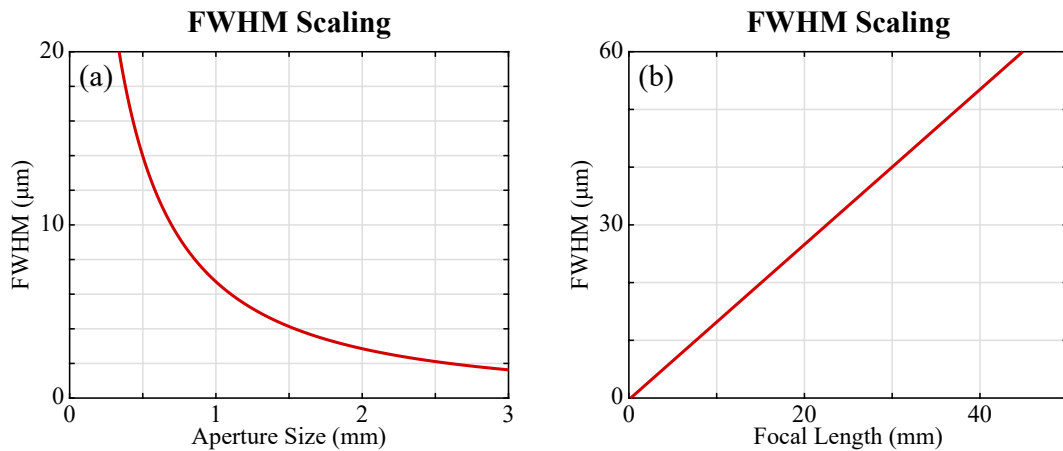


Figure 3.3: (a) Simulated power full width at half maximum (FWHM) versus aperture size for a focusing phased array with $5\ \text{mm}$ focal length and $1550\ \text{nm}$ wavelength. (b) Simulated power FWHM versus focal length for a focusing phased array with $1\ \text{mm}$ aperture size and $1550\ \text{nm}$ wavelength.

is applied to the antennas to steer the radiated beam in the far field [34,35,40,71,72]. However, when this conventional linear steering approach is applied to a focusing phased array, in addition to the desired steering in the array dimension, the steering induces an undesired offset to the focal length of the spot. As an example, an array with 512 antennas, 2 μm antenna pitch, 5 mm desired focal length, and 1550 nm wavelength is simulated, as shown in Fig. 3.4a. When this array is steered to a 1.5 mm offset in the array dimension using linear steering, as shown in Fig. 3.4b, the resulting focal spot is formed at $z = 4.19$ mm. For many applications, this steering-induced shift in the focal length can prove to be detrimental; for example, for optical trapping applications wherein the sample under test is often housed in a flat microfluidic channel [75], this effect can shift the focal spot out of the channel.

Instead, the desired horizontal offset should be encoded directly in the focusing phase as follows. First, the distance from each antenna to the focal point, initially given by Eq. (3.2), is modified as:

$$L_n = \sqrt{f_z^2 + [d(N/2 + 1/2 - n) + f_x]^2} \quad (3.4)$$

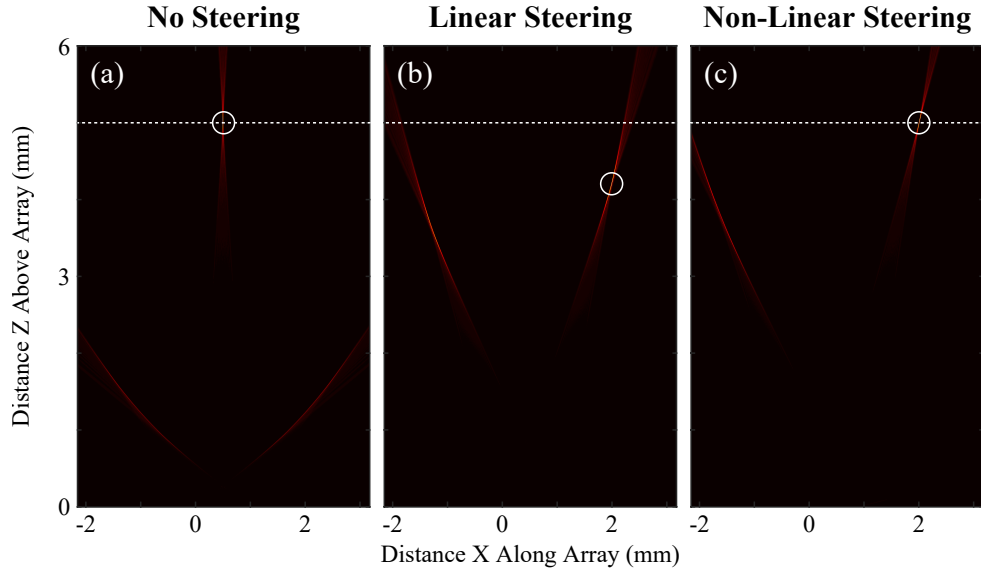


Figure 3.4: Simulated array-factor intensity above the array assuming (a) no steering, (b) linear steering, and (c) corrected non-linear steering. Simulated intensities are shown for an array with $f_x = 1.5$ mm offset, 512 antennas, 2 μm antenna pitch, 5 mm focal length, and 1550 nm wavelength.

where f_z is the desired focal length and f_x is the desired focal offset. The necessary element phase distribution then follows directly from Eq. (3.3). For comparison, the linear and non-linear steering phases are shown in Fig. 3.5 without 2π phase wrapping for clarity. By applying this non-linear steering approach for $f_x = 1.5$ mm, the focal spot is formed with the correct offset at the desired 5 mm focal length, as shown in Fig. 3.4c. Note that, similar to a standard beam-forming phased array, as the array is steered, the array’s effective area is changed, which, in turn, increases the FWHM of the focal spot from $6.6 \mu\text{m}$ to $7.6 \mu\text{m}$.

3.1.3 Splitter-Tree-Based Architecture and Experimental Results

As a proof of concept, a passive focusing integrated optical phased array is designed and fabricated, as shown in Fig. 3.6. The phased array architecture utilized in this demonstration is based on a one-dimensional silicon-based splitter tree (similar to the silicon-nitride tree architecture demonstrated in [70]) with additional novel phase components and focusing antennas added to enable focusing in the array and the antenna dimensions, respectively.

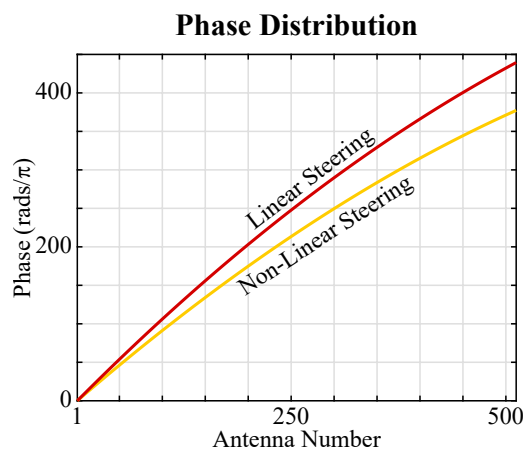


Figure 3.5: Element phase distribution for a focusing phased array with an $f_x = 1.5$ mm offset assuming linear steering (red) and corrected non-linear steering (yellow). Phase profiles are shown for an array with 512 antennas, $2 \mu\text{m}$ antenna pitch, 5 mm focal length, and 1550 nm wavelength.

The phased array and accompanying device test structures are fabricated in a CMOS-compatible foundry process at SUNY Poly on a 300-mm silicon-on-insulator (SOI) wafer with a 2- μm -thick buried oxide. The 220-nm-thick silicon device layer is patterned using 193 nm immersion lithography.

At the system input, an on-chip inverse-taper edge coupler is designed to efficiently couple light from a 6.5- μm -mode-field-diameter lensed fiber to a 400-nm-wide silicon waveguide with a ~ 2.5 dB measured coupling efficiency.

Next, a 9-layer splitter tree network is used to evenly distribute the input power to 512 waveguide arms with a final pitch of 2 μm . Within the network, a compact Y-junction is used as a symmetric 1-to-2-waveguide splitting device, as developed in [82]. The Y-junction devices are connected by either 90° bends or sinusoidal-shaped bends with 5 μm minimum bending radii to reduce bending radiation loss. The final waveguide pitch is limited to 2 μm to reduce undesired evanescent coupling between antennas in the array.

At the output of the splitter tree, a phase bump structure is placed on each waveguide arm to impart a static phase delay dependent on the maximum width of the device. The phase bump adiabatically increases the width of the waveguide from the nominal 400 nm width to a variable wider width using a sinusoidal shape, as shown in Fig. 3.7a. The length of the structure is chosen to be 6 μm to reduce undesired excitation of higher-order modes while keeping a compact form factor. As

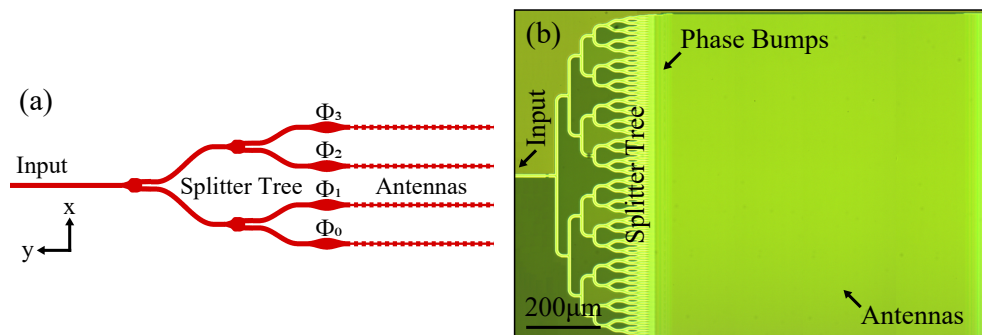


Figure 3.6: (a) Schematic of a splitter-tree-based focusing phased array with 4 antennas. (b) Micrograph of a fabricated splitter-tree-based focusing phased array with 512 antennas and 2 μm antenna pitch.

shown in Fig. 3.7b both numerically using a finite-difference time-domain (FDTD) solver and experimentally, as the width of the device is increased, the relative phase induced by the structure increases. As such, by choosing the appropriate widths for each phase bump, the correct phase profile, given by Eq. (3.3), is applied. Note that, due to the robustness of the wrapped phase encoding, the discrepancy between the simulated and measured phase shown in Fig. 3.7b (which can be attributed to discrepancy between the expected and actual fabricated silicon device layer thickness) does not have a significant effect on the resulting performance of the system.

Finally, after each phase bump, a 0.9-mm-long grating-based focusing antenna is placed on each arm to create a $1.024 \text{ mm} \times 0.9 \text{ mm}$ aperture size. The antenna utilizes a full-etch perturbation geometry, similar to [34], to enable radiation out of the plane of the chip, as shown in Fig. 3.8a. By manipulating the symmetric inward perturbation of each period of the antenna, the local scattering strength, defined as the power radiated by the antenna per unit length, can be controlled, as shown in Fig. 3.8b numerically and experimentally (the discrepancy between simulated and measured values can be attributed to rounding of the perturbations during fabrication without

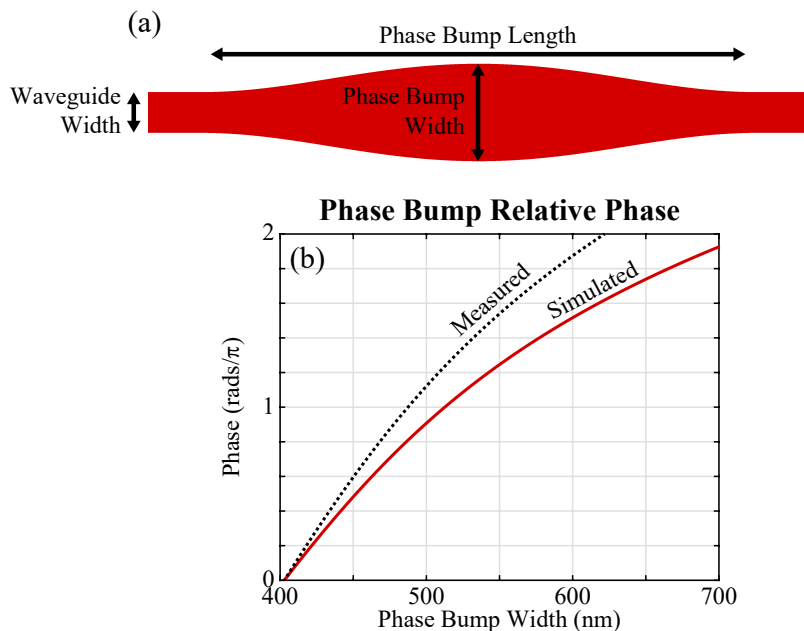


Figure 3.7: (a) Schematic of a phase bump device. (b) Simulated (red) and measured (black) relative phase versus phase bump width for the phase bump device.

optical-proximity-correction techniques). As such, the antenna is designed with uniform perturbations along the antenna length – i.e., constant scattering strength – to generate an exponentially-decaying intensity profile. Specifically, a 30 nm perturbation is chosen to minimize the excess power at the end of the 0.9-mm-long antenna while maintaining a large effective aperture.

Next, to enable focusing in the antenna dimension, the period of the antenna is adiabatically chirped along the antenna length. This process is similar to adiabatic synthesis of locally periodic vertical grating couplers with varying radiation

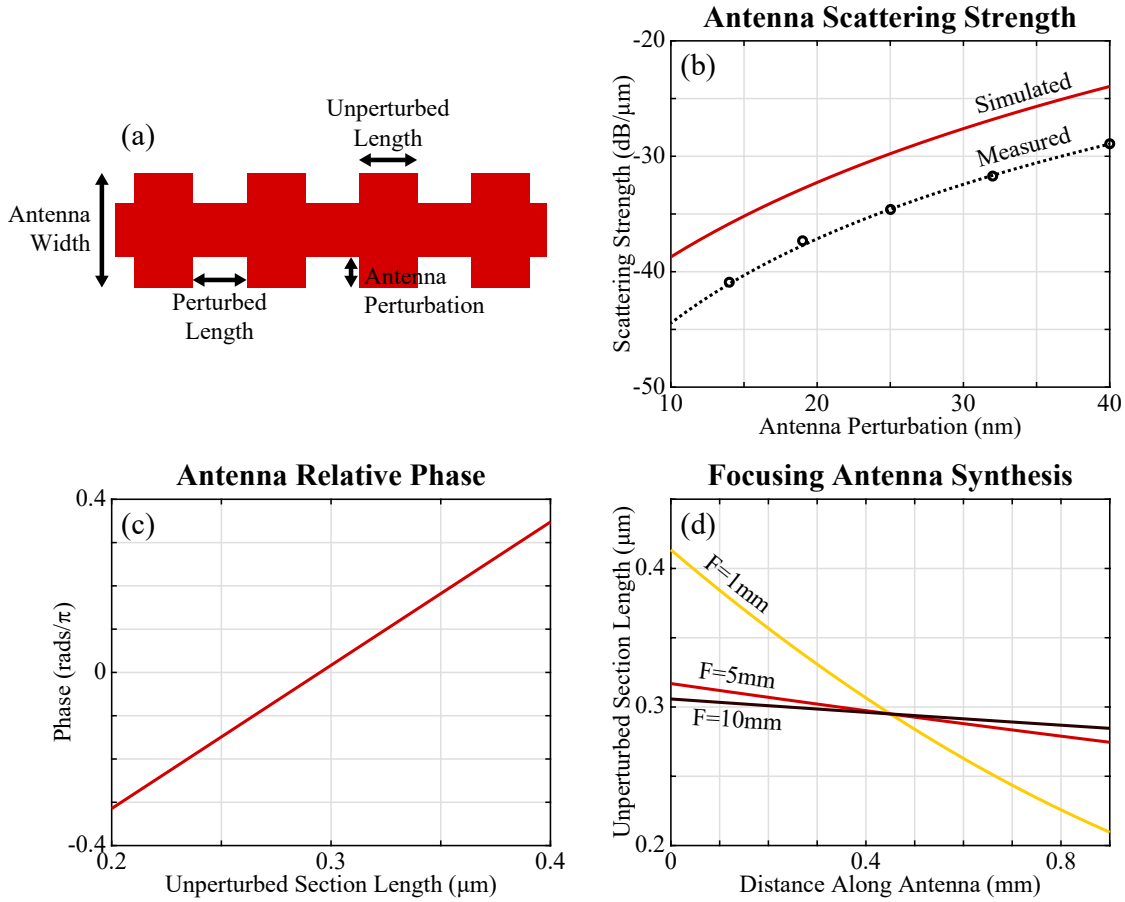


Figure 3.8: (a) Schematic of a grating-based antenna. (b) Simulated (red) and measured (black) scattering strength versus antenna perturbation for the grating-based antenna. (c) Simulated relative phase versus length of the unperturbed section of the grating-based antenna. (d) Synthesized unperturbed section length versus distance along the antenna necessary for focusing at 1 mm (yellow), 5 mm (red), and 10 mm (black) for a focusing antenna with a constant 30 nm perturbation and 310 nm perturbed length.

angles [83–85]. To implement this synthesis, the relative phase induced by a single period unit cell of the antenna is simulated in FDTD as the length of the wider, unperturbed section of the antenna is varied and the length of the narrower, perturbed section is kept at a constant 310 nm, as shown in Fig. 3.8c. These period unit cells are then chosen and concatenated such that the synthesized phase along the antenna follows the unwrapped phase given by Eq. (3.3). The synthesized lengths for focusing at 1 mm, 5 mm, and 10 mm are shown in Fig. 3.8d. Note that an unperturbed section length of 295 nm is chosen as the reference phase point during the synthesis since, at that point, the antenna radiates upwards with a slight angle. Although this introduces a slight angle offset to the beam in the antenna dimension, it ensures that the antenna does not induce undesired back reflections as dictated by the Bragg condition. Additionally, since the focusing antenna is synthesized using the unwrapped phase, it is more susceptible to compounded fabrication-induced phase errors, which can result in undesired variations in the focal spot location and size. Generally, fabrication variations will have a more significant effect on the spot size of antennas with shorter focal lengths and on the focal length of antennas with larger focal lengths.

To characterize the fabricated array, an optical system is used to simultaneously image the plane of the chip onto a visible camera and an InGaAs IR camera, as

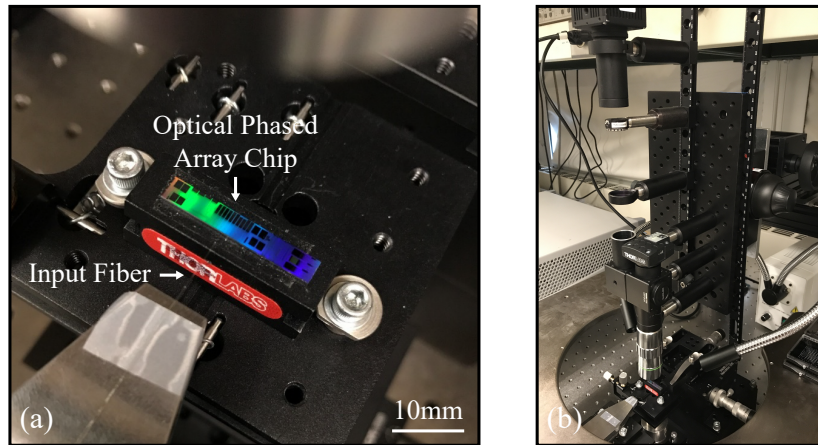


Figure 3.9: Photographs of (a) a fabricated integrated optical phased array chip on the scanning near-field characterization setup and (b) the scanning near-field characterization setup.

shown in Fig. 3.9. The height of the optical imaging system is then progressively scanned such that top-down views of the intensity at varying heights above the chip are recorded. These top-down views are then integrated in the antenna or the array dimension to visualize the cross-sectional intensity as a function of the distance above the chip.

The resulting cross-sectional intensity as a function of the distance above the chip and three top-down views are shown in Figs. 3.10a–e for the fabricated splitter-tree-based 2D-focusing phased array with 512 antennas, $2\ \mu\text{m}$ antenna pitch, 5 mm focal length, and 1550 nm wavelength. In the plane of the chip (Fig. 3.10e), the aperture is illuminated by the antennas. As the system scans to the expected focal plane 5 mm above the chip (Fig. 3.10d), the radiated light is tightly-focused in both the x and y dimensions. At this height, a FWHM of $\sim 6.4\ \mu\text{m}$ is measured in the array dimension, x , closely matching the simulated value of $6.6\ \mu\text{m}$. Similarly, a FWHM of $\sim 7.6\ \mu\text{m}$

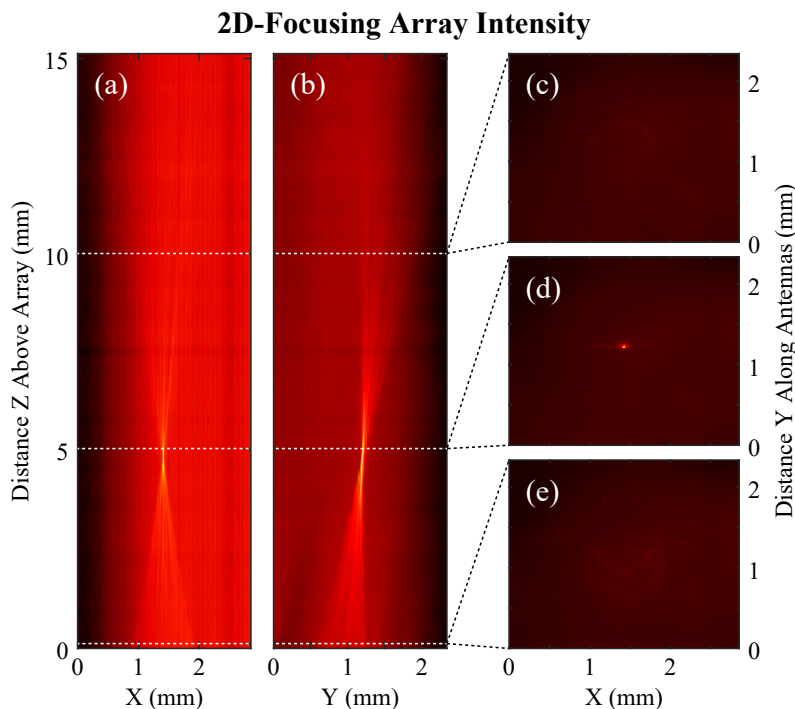


Figure 3.10: Measured cross-sectional intensity (in dB) above the chip for a 2D-focusing splitter-tree-based phased array in the (a) x plane and (b) y plane with top-down intensity shown (e) in the plane of the chip, (d) at the focal plane, and (c) above the focal plane. Intensities are shown for an array with 512 antennas, $2\ \mu\text{m}$ antenna pitch, 5 mm focal length, and 1550 nm wavelength.

is measured in the antenna dimension, y , matching the expected value of $7.6\ \mu\text{m}$. A sidelobe suppression of $\sim 9.5\ \text{dB}$ is measured with an approximately symmetric pattern in the array dimension and an asymmetric pattern in the antenna dimension due to the exponentially-decaying intensity profile of the antennas. Additionally, as expected, the angle in the antenna dimension is slightly offset. Finally, above the focal plane (Fig. 3.10c), the light is, once again, diffracted out. Next, using a pinhole shutter at the focal plane to block any grating lobes and stray light and a detector above the shutter, an on-chip input to main lobe efficiency of approximately $-12\ \text{dB}$ is measured (the losses can be attributed to waveguide propagation loss, Y-junction splitter losses, and antenna emission losses, including power radiated to the grating lobes).

For comparison, a similar 1D-focusing array is also fabricated. The array utilizes the same splitter-tree-based architecture with 512 antennas, $2\ \mu\text{m}$ antenna pitch,

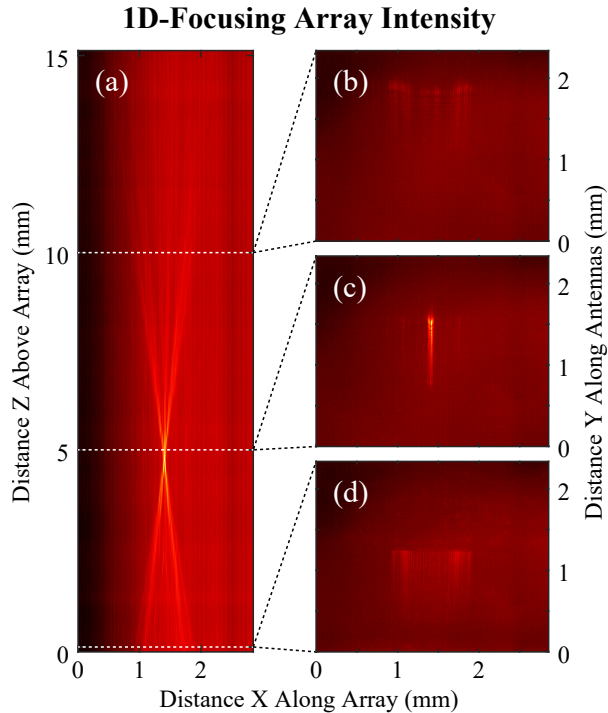


Figure 3.11: (a) Measured cross-sectional intensity (in dB) above the chip for a 1D-focusing splitter-tree-based phased array with top-down intensity shown (d) in the plane of the chip, (c) at the focal plane, and (b) above the focal plane. Intensities are shown for an array with 512 antennas, $2\ \mu\text{m}$ antenna pitch, $5\ \text{mm}$ focal length, and $1550\ \text{nm}$ wavelength.

5 mm focal length, and 1550 nm wavelength to focus in the array dimension; however, standard non-focusing antennas are used such that the system does not focus in the antenna dimension. The resulting cross-sectional intensity as a function of the distance above the chip and three top-down views are shown in Figs. 3.11a–d. In the plane of the chip (Fig. 3.11d), the aperture is illuminated by the antennas. As the system scans to the expected focal plane 5 mm above the chip (Fig. 3.11c), the light is tightly-focused in the array dimension to a FWHM of $\sim 6.4 \mu\text{m}$, which closely matches both the simulated and 2D-focusing results. Finally, above the focal plane (Fig. 3.11b), the light is, once again, diffracted out in the array dimension.

Similarly, both 1D- and 2D-focusing phased arrays are also fabricated with a 1 mm focal length. The resulting measured focal spots had FWHMs of $\sim 1.7 \mu\text{m}$ in the array dimension and $\sim 2.9 \mu\text{m}$ in the antenna dimension, compared to the simulated values of $1.4 \mu\text{m}$ and $1.5 \mu\text{m}$, respectively. These slight discrepancies can be attributed to experimental error in measuring such small spot sizes with the finite pixel size of the IR camera and compounding fabrication-induced phase errors in the focusing antennas.

Finally, the wavelength of the light coupled into the 5-mm-focal-length 2D-focusing array is swept to demonstrate wavelength steering in the antenna dimension. In theory, since the antennas are based on grating principles, as the wavelength of light is increased, the effective period of the antenna becomes smaller and the angle of the light radiated by the antenna varies such that the beam is steered closer to the input of the chip. Three cross-sectional intensities in the antenna dimension for wavelengths of 1550 nm, 1560 nm, and 1570 nm are shown in Figs. 3.12a–c. As expected, as the wavelength is increased, the radiation angle is shifted while still maintaining its focusing characteristics. To quantify this shift, the spatial offset of the beam in the antenna dimension is plotted as a function of the input wavelength, as shown in Fig. 3.12d.

Since the array is fabricated in a CMOS-compatible platform, it is naturally scalable to a dynamic arbitrarily-tunable system with active silicon-based phase shifters on each waveguide arm [34,35,37,41,72,73]. This extension of the system would enable

steering of the focal spot in the array dimension in addition to the wavelength steering capability in the antenna dimension. However, although the array-dimension tuning would be fully arbitrary, this architecture is fundamentally limited to 2D-focusing in only one focal plane since the wavelength steering is only capable of inducing a lateral offset. For applications where both focal length and offset tuning is required, a different architecture capable of scaling to non-linear electrical tuning in both dimensions (as described in Sec. 3.1.4) is necessary.

3.1.4 Pixel-Based Architecture and Experimental Results

Next, as a second method for experimentally demonstrating focusing integrated optical phased arrays, a passive focusing phased array using a two-dimensional pixel-based architecture is designed and fabricated, as shown in Fig. 3.13. By using the architecture developed in [71,86] and applying it to the focusing theory developed in Sec. 3.1.2, this system is capable of scaling to electrical phase control in both dimensions of the

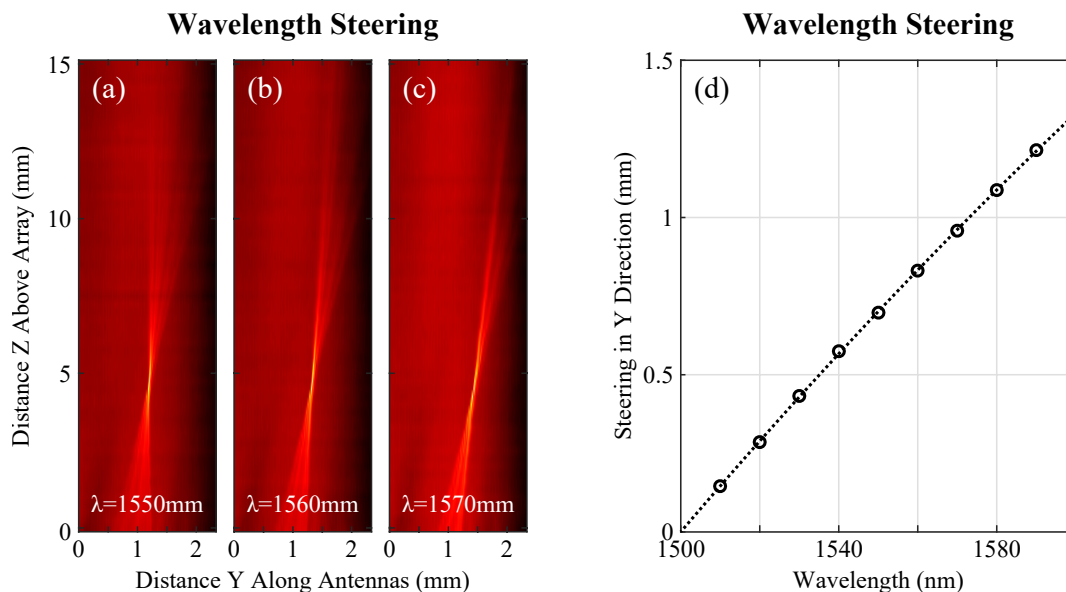


Figure 3.12: Measured cross-sectional intensity (in dB) above the chip for a 2D-focusing splitter-tree-based phased array at (a) 1550 nm, (b) 1560 nm, and (c) 1570 nm wavelengths. (d) Experimental results showing steering in the antenna dimension, y , versus wavelength. Results are shown for an array with 512 antennas, $2\ \mu\text{m}$ antenna pitch, and 5 mm focal length.

array to enable dynamic tuning of the spot’s focal length and offset, simultaneously.

The pixel-based phased array and accompanying device test structures are also fabricated in a CMOS-compatible foundry process at SUNY Poly on a 300-mm silicon-on-insulator (SOI) wafer with a 2- μm -thick buried oxide using 193 nm immersion lithography. However, a non-standard 380-nm-thick silicon device layer is used (compared to the standard 220 nm thickness used in [71, 86]), which requires redesign of all photonic components in the system.

At the system input, an on-chip inverse-taper edge coupler is designed to efficiently couple light from a 6.5- μm -mode-field-diameter lensed fiber to a 450-nm-wide silicon waveguide with a ~ 2.5 dB measured coupling efficiency. A set of M row pixels are then used to couple light from the input waveguide to M row waveguides. Next, on each row waveguide, M emitter pixels are used to couple light from the row waveguide to M compact antenna emitters. This creates an array aperture of $M \times M$ antennas, as shown in Fig. 3.13a. Notably, the row pixels and the emitter pixels are designed with the same topology (with the exception that the emitter pixels are terminated with antenna emitters) to enable arbitrary control of each antenna’s amplitude and phase [71].

Within each row and emitter pixel, a directional coupler is used for amplitude control [71]. By increasing the length of the coupling region of the device, the percentage of power coupled either from the input waveguide to the row waveguide or from the

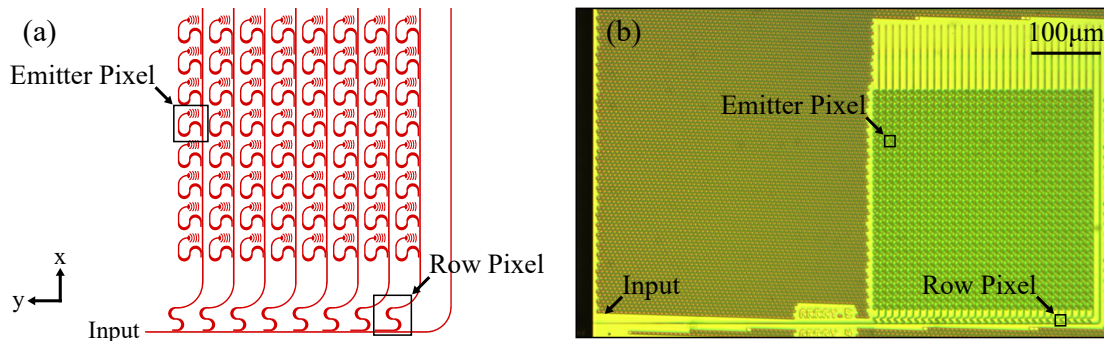


Figure 3.13: (a) Schematic of a pixel-based focusing phased array with 64 antennas. (b) Micrograph of a fabricated pixel-based focusing phased array with 1024 antennas and 10 μm antenna pitch.

row waveguide to the emitter is varied. Figure 3.14a shows this relationship as simulated in FDTD assuming a 380 nm waveguide height and a 120 nm gap between the coupler and the waveguide. To enable uniform emission from each antenna within the array, the power coupling coefficients for both the row pixels and the emitter pixels are set to

$$\eta_m = \frac{1}{M - m + N_{\text{phantom}} + 1} \quad (3.5)$$

where η_m is the coupling coefficient for both the m^{th} row pixel and the m^{th} emitter pixel within each row, M is the total number of rows and the total number of emitters in each row, m varies from 1 to M , and N_{phantom} is the number of desired “phantom” antennas [74,86]. This phantom antenna concept is introduced to reduce the necessary coupling coefficient of the last pixel. Although this results in some power being discarded at the end of the input waveguide and each row waveguide, it eliminates the need for the last directional coupler to have 100% coupling, which would require a relatively long coupling length and increase the pixel size [86]. For example, in this implementation, N_{phantom} is set to 3 such that the highest coupling coefficient needed is 25%.

Each directional coupler is followed by two compact adiabatic curves with a variable offset length between them to allow for arbitrary phase control to each row or

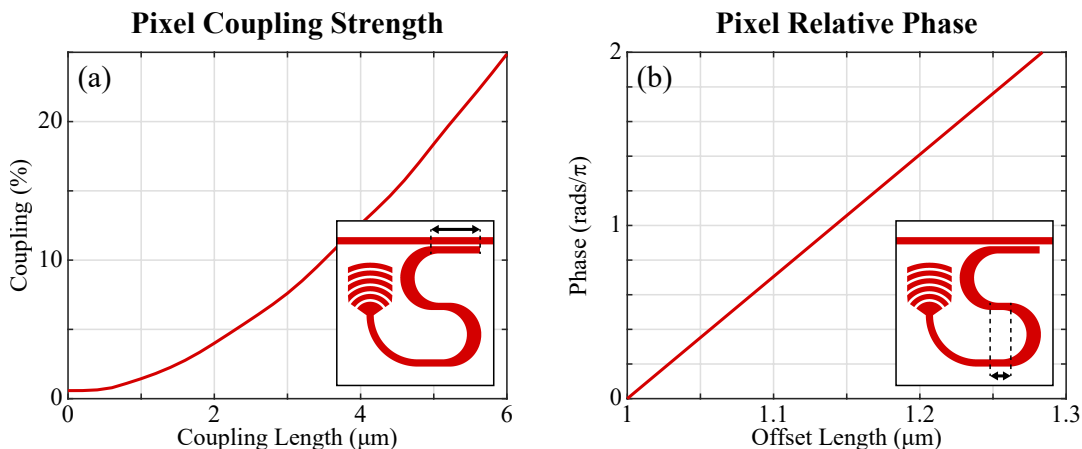


Figure 3.14: Simulated (a) coupling versus coupling waveguide length and (b) relative phase versus offset length for the pixel-based architecture unit cell. Schematics of the unit cell are included as insets with each variable length indicated.

emitter [71]. Figure 3.14b shows the resulting relative phase versus offset length as simulated in FDTD. For focusing in two dimensions, the offset lengths of each row and emitter pixel are set accordingly such that the correct phase profile, given by Eq. (3.3), is applied. Since the phase required for focusing in two dimensions is separable, the phases for focusing in each dimension can be independently applied – i.e., the phase profile for focusing in the y dimension is applied to the row pixels whereas the phase profile for focusing in the x dimension is applied to the emitter pixels. Additionally, the phase encodings are modified to compensate for the variable phase induced by the directional couplers, as discussed in [86].

Finally, a compact emitter antenna is placed in each emitter pixel to radiate the light out of the plane of the chip at a slight angle from vertical to reduce back reflections. The emitter design is similar to the design presented in [71]; however, its dimensions are optimized for the custom 380-nm-height silicon. Specifically, each emitter antenna consists of 5 fully-etched grating teeth with a 490 nm period and a 172 nm gap between teeth.

To characterize the array, the same scanning optical imaging system is used as in Sec. 3.1.3. The resulting cross-sectional intensity as a function of the distance above the chip and three top-down views are shown in Figs. 3.15a–e for the fabricated pixel-based 2D-focusing phased array with 1024 antennas (i.e., 32 rows by 32 columns), 10 μm antenna pitch, 5 mm focal length, and 1550 nm wavelength. Due to the 10 μm antenna pitch, multiple grating lobes are generated in the array factor in both the x and y dimensions. Two beams – the main beam and one of the first-order grating lobes – are seen in the camera’s field of view in the x dimension, as shown in Fig. 3.15a. As the system scans to the focal plane 5 mm above the chip (Fig. 3.15d), the main beam is tightly focused, as expected. At this height, FWHMs of $\sim 21.5 \mu\text{m}$ are measured in both the x and y dimensions, closely matching the simulated value of 21.4 μm . Sidelobe suppression of $\sim 8 \text{ dB}$ and $\sim 5 \text{ dB}$ is measured in the x and y dimensions, respectively. Additionally, using a pinhole shutter at the focal plane to block any grating lobes and stray light and a detector above the shutter, an on-chip input to main lobe efficiency of approximately -18.5 dB is measured (the losses can be

attributed to waveguide propagation loss, bending losses in the tight adiabatic bends, phantom antenna losses, and antenna emission losses, including power radiated to the grating lobes).

For comparison, two additional 1024-antenna pixel-based arrays are fabricated with 3 mm and 10 mm focal lengths. The measured FWHMs for all three arrays are plotted in Fig. 3.16 against the theory developed in Sec. 3.1.2 showing excellent agreement. As expected, the FWHM increases linearly with the focal length of the array.

Finally, a similar pixel-based array with 10,000 antennas (i.e., 100 rows by 100 columns) is fabricated. Since the aperture size of the array is significantly larger compared to the 1024 antenna array ($1\text{ mm} \times 1\text{ mm}$ versus $0.32\text{ mm} \times 0.32\text{ mm}$), the range of possible focal lengths is greatly increased due to the quadratic scaling of the near-field boundary compared to the aperture size. Similarly, the expected FWHMs

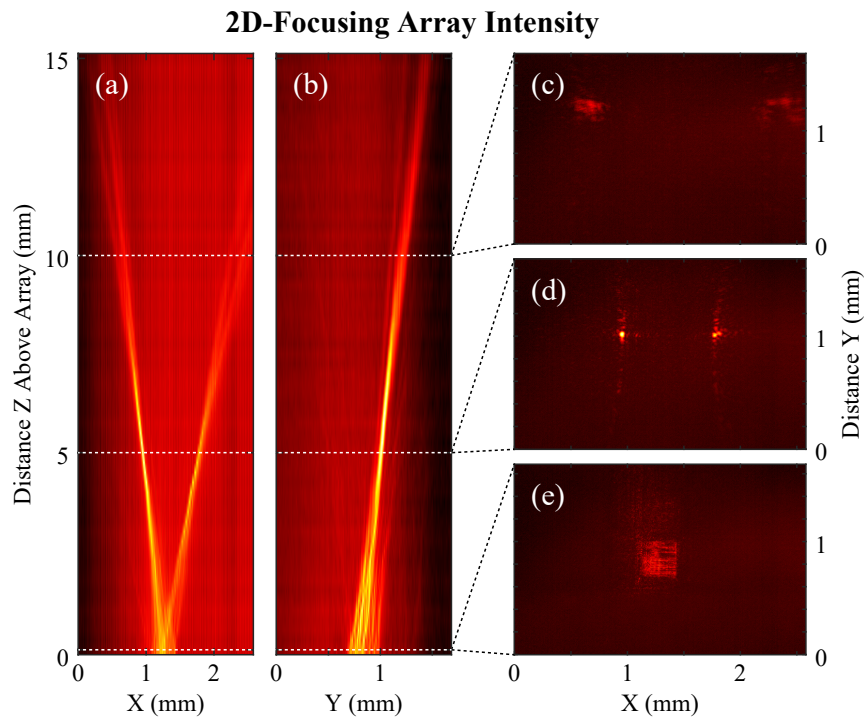


Figure 3.15: Measured cross-sectional intensity (in dB) above the chip for a 5-mm-focal-length pixel-based phased array in the (a) x plane and (b) y plane with top-down intensity shown (e) in the plane of the chip, (d) at the focal plane, and (c) above the focal plane. Intensities are shown for an array with 1024 antennas, $10\text{ }\mu\text{m}$ antenna pitch, and 1550 nm wavelength.

are much smaller due to the inverse relationship of the aperture size and the FWHM. As such, for the fabricated 10,000-antenna 10-mm-focal-length array, the measured FWHMs in the x and y dimensions are $\sim 23.3\ \mu\text{m}$ and $\sim 20.9\ \mu\text{m}$, respectively. However, due to the large number of antennas in the array, uniform distribution of power to each pixel in the array is more difficult since lower coupling coefficients and higher precision are needed. As such, these measured FWHMs are larger than the simulated value of $13.5\ \mu\text{m}$. In future implementations, lower coupling coefficients and higher precision could be achieved by varying the coupling gap, as proposed in [74,86].

Similar to the splitter-tree-based architecture, since the pixel-based array is also fabricated in a CMOS-compatible platform, it is naturally scalable to a dynamic arbitrarily-tunable system with active silicon-based phase shifters integrated in each pixel as demonstrated in [71]. This extension of the system would enable both two-dimensional steering of the focal spot using the non-linear steering formulation developed in Sec. 3.1.2 and complete control of the focal length of the spot.

3.1.5 Conclusion

In summary, this work presents the first demonstration of integrated optical phased arrays that focus radiated light to a tightly-confined spot in the near field. The

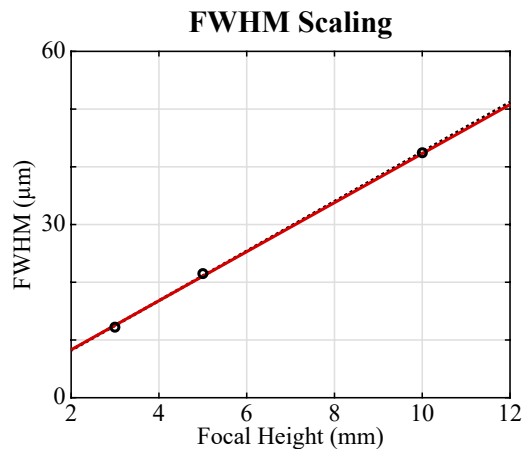


Figure 3.16: Simulated (red) and measured (black) power full width at half maximum (FWHM) versus focal length. Results are shown for pixel-based arrays with 1024 antennas, $10\ \mu\text{m}$ antenna pitch, and $1550\ \text{nm}$ wavelength.

phase profiles necessary for generating focused beams using phased arrays with non-linear steering have been developed and relevant variables and parameters have been presented and discussed. Furthermore, two architectures have been proposed for demonstrating passive focusing integrated optical phased arrays: a one-dimensional splitter-tree-based architecture with focusing antennas and a two-dimensional pixel-based architecture. Both architectures have been used to demonstrate a variety of aperture size and focal length arrays, including a 512-antenna splitter-tree-based array with a $\sim 7\ \mu\text{m}$ spot at a 5 mm focal length, a 1024-antenna pixel-based array with a $\sim 21\ \mu\text{m}$ spot at a 5 mm focal length, and a 10,000-antenna pixel-based array with a $\sim 21\ \mu\text{m}$ spot at a 10 mm focal length.

Since the arrays are fabricated in CMOS-compatible platforms, they are naturally scalable to active arbitrarily-tunable systems with varying advantages. While the splitter-tree-based architecture is limited to active focusing in only one focal plane, it requires a smaller number of active controls and its close antenna pitch reduces the number of grating lobes, which increases the steering range of the device. In comparison, the pixel-based architecture enables control of the lateral steering and focal length in both dimensions and could be arbitrarily tuned without the need for a wavelength-tunable laser source; however, its large pixel pitch limits the steering range and it requires a larger number of active controls.

In addition to this natural evolution to active systems, the demonstrations can be scaled to larger aperture sizes [70] to further reduce the focal spot size and enable larger focal lengths. Additionally, to improve the field profile at the focal plane, both architectures can be modified to emit with Gaussian amplitude profiles by either using a star coupler for the splitter-tree-based architecture [41] or by modifying the coupling coefficients in the pixel-based architecture [40]. Furthermore, using numerical methods and synthesis algorithms [83, 84], the splitter-tree-based arrays can be further improved by appropriately varying the perturbation strength of the array's focusing antennas to produce either a uniform or a Gaussian emission profile. Finally, to improve the efficiencies of both architectures, the element-factor patterns of the long grating-based antennas and compact emitter antennas could be further opti-

mized to reduce the power radiated to the grating lobes. Additionally, the pixel pitch of the pixel-based architecture could be reduced to lower the number of grating lobes by implementing a 1D splitting network with outputs that route to a 2D pixel-based emitter array [35]; however, this architecture would require individual phase control signals for each emitter to correctly apply the 2D-focusing phase.

The demonstrated on-chip focusing optical phased arrays have important applications in a variety of areas. For example, by enabling highly-enhanced tightly-focused beams with large focal lengths, these systems open up new possibilities for large-scale biological characterization and monitoring through optical trapping [75–77], especially for *in-vivo* experiments wherein relatively large spatial offsets are an advantage [77]. Furthermore, by enabling a chip-based source of highly-focused beams, these devices have applications in chip-scale laser lithography techniques ranging from trapping-based nano-assembly [87, 88] to selective laser melting additive manufacturing [79].

3.2 Bessel-Beam-Generating Integrated Optical Phased Arrays

The following work was done in collaboration with Christopher V. Poulton (MIT), Matthew J. Byrd (MIT), Manan Raval (MIT), and Michael R. Watts (MIT). This work has been published in [14,15].

3.2.1 Introduction

Bessel beams exhibit many interesting and useful properties [89–92], including propagation of a finite-width central beam without diffraction-induced spreading in the infinite aperture limit [89]. Due to their unique properties, Bessel beams have contributed to a variety of important applications and advances [93]. For example, they have enabled multi-plane, multi-particle optical trapping [94], reduction of scattering and increases in depth of field in microscopy [95,96], efficient laser lithography and fabrication [97], promotion of free-electron laser gain [98], improved laser corneal surgery [99], and adaptive free-space optical communications [100].

In practice, Bessel beams are experimentally approximated by introducing a truncated Gaussian envelope to the Bessel beam to generate a Bessel-Gauss beam with similar central-beam properties within the Bessel length limit [89–91]. Conventionally, Bessel-Gauss beams have been generated using a bulk optics approach wherein an Axicon lens (a conical glass prism) is illuminated with a truncated Gaussian beam to produce a Bessel-Gauss beam at the output [91]. Moreover, recent work has turned towards generation of Bessel beams in more compact form factors. For example, Bessel-Gauss beam generation has been demonstrated using spatial light modulators [101], Dammann gratings [102], slit-groove structures [103], and meta-surfaces [104,105]. However, these demonstrations do not provide full on-chip integration and most are fundamentally limited to static beam formation.

Integrated optical phased arrays, which manipulate and dynamically steer light with large aperture sizes [70] and the potential for 200 MHz rates [35], provide one

possible approach to generation of quasi-Bessel beams in a fully-integrated platform. However, current phased array demonstrations have primarily focused on systems which form and steer beams or project arbitrary radiation patterns in the far field (as discussed in Ch. 2) [35,37,41,70–72,106].

In this section, integrated optical phased arrays are proposed and demonstrated for the first time as a method for generating quasi-Bessel beams in a fully-integrated, compact-form-factor system. First, the phase and amplitude distributions necessary for generating phased-array-based Bessel-Gauss beams are developed analogous to bulk-optics Bessel implementations. Discussion and simulations detailing the effect of the array aperture and phase parameters on the full width at half maximum (FWHM) and Bessel length of the generated beam are included. Next, a splitter-tree-based phased array architecture [70] is modified to passively encode arbitrary phase and amplitude feeding of the array – necessary for Bessel-Gauss-beam generation – and experimental device characterization data is presented. Finally, the developed theory and system architecture are utilized to demonstrate a $0.64\text{ mm} \times 0.65\text{ mm}$ aperture integrated phased array that generates a quasi-one-dimensional (quasi-1D) Bessel-Gauss beam with a $\sim 14\text{ mm}$ Bessel length and $\sim 30\text{ }\mu\text{m}$ power FWHM. By using a CMOS-compatible platform, the system is naturally scalable to an active demonstration with wafer-scale 3D-bonded electronics [9] and monolithically-integrated lasers [7] (as discussed in Ch. 2) for a fully-integrated and steerable chip-based Bessel-beam generator.

3.2.2 Theory

In general, a phased array is a system comprised of an array of antennas that are fed with controlled phases and amplitudes to generate arbitrary radiation patterns. If the antennas are spaced with a uniform pitch, d , and fed with a Gaussian amplitude and a linear phase distribution (as shown in Fig. 3.17), the array generates a steerable, diffracting Gaussian beam in the far field of the array. This Gaussian element

amplitude distribution is given by

$$A_n = \exp\left(\frac{-4 \ln(2)(n - N/2 - 1/2)^2}{(NA_0)^2}\right) \quad (3.6)$$

where A_n is the amplitude applied to the n th antenna, N is the total number of antennas in the array, and A_0 is the variable amplitude parameter such that the FWHM of the Gaussian is given by NA_0 . The near-field electric-field profile generated by this phased array can be approximated by summing the electric-field components of each element in the array:

$$E(x, y, z) = \sum_{n=1}^N E_n(x, y, z) \approx \sum_{n=1}^N A_n e^{-i(2\pi r_n/\lambda + \Phi_n)} \quad (3.7)$$

where Φ_n is the phase applied to the n th antenna, r_n is the distance from the n th antenna to the point under consideration at coordinate (x, y, z) , and λ is the propagation wavelength. Using this method, the intensity profile generated by a Gaussian array with $A_0 = 1/2$, $N = 64$, and $d = 10 \mu\text{m}$ is simulated, as shown in Fig. 3.18a.

In contrast, if an ‘‘Axicon-like’’ element phase distribution is applied in addition to the Gaussian amplitude, the array will generate a quasi-Bessel beam in the near

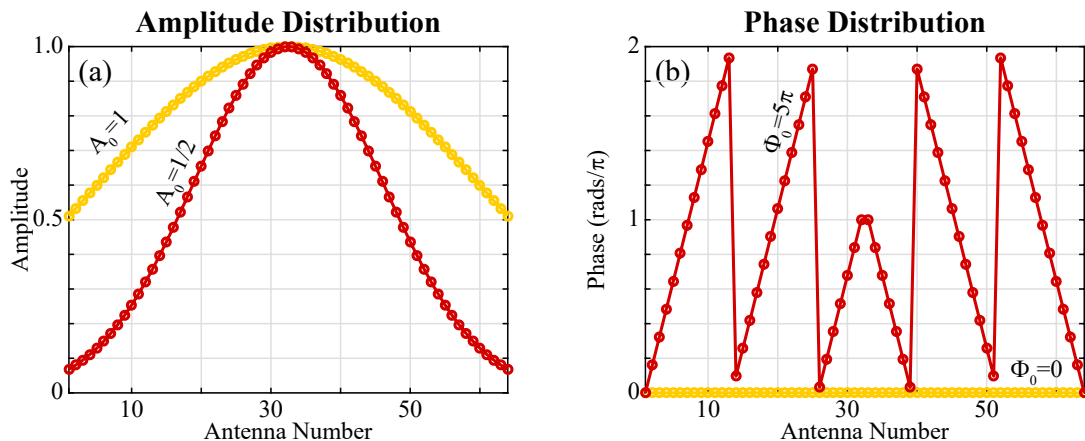


Figure 3.17: (a) Element amplitude distribution for a Gaussian-amplitude phased array with $A_0 = 1/2$ (red) and $A_0 = 1$ (yellow). (b) Element phase distribution for a standard (yellow) and Bessel (red) phased array with $\Phi_0 = 0$ and $\Phi_0 = 5\pi$, respectively. Phase and amplitude profiles and simulated intensities are shown for an array with 64 antennas, $10 \mu\text{m}$ antenna pitch, and 1550nm wavelength.

field of the array. This Axicon phase is given by

$$\Phi_n = \Phi_0 \frac{-|n - N/2 - 1/2| + N/2 - 1/2}{N/2 - 1} \quad (3.8)$$

where Φ_n is the phase applied to the n th antenna and Φ_0 is the variable phase parameter. This phase can be encoded modulo 2π , as shown in Fig. 3.17b. The simulated intensity profiles generated by three 1D Bessel-beam arrays with varying parameters, Φ_0 and A_0 , are shown in Figs. 3.18b–d. As shown in Fig. 3.18d, if the FWHM of the Gaussian element amplitude distribution is too large compared to the aperture size of the array, the integrity of the Bessel-Gauss beam is compromised – the beam formed in Fig. 3.18d is degraded compared to a similar beam in Fig. 3.18c. Additionally, due to discretization of the continuous Bessel theory on an array with $d > \lambda/2$, twelve higher-order grating lobes, which also exhibit Bessel properties, are generated by the array at larger angles (not shown in the simulation window).

For potential applications, two valuable figures of merit of a quasi-Bessel-beam-generating array are the power FWHM of the central radiated beam and the Bessel

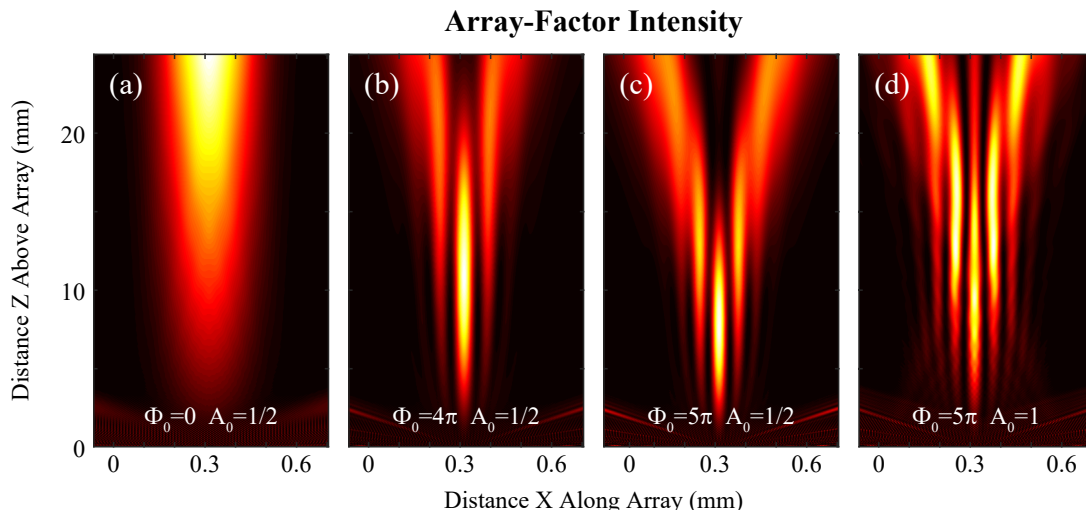


Figure 3.18: Simulated array-factor intensity above the array for a (a) Gaussian array with $\Phi_0 = 0$ and $A_0 = 1/2$, (b) Bessel array with $\Phi_0 = 4\pi$ and $A_0 = 1/2$, (c) Bessel array with $\Phi_0 = 5\pi$ and $A_0 = 1/2$, and (d) distorted Bessel array with $\Phi_0 = 5\pi$ and $A_0 = 1$. Simulated intensities are shown for an array with 64 antennas, $10\ \mu\text{m}$ antenna pitch, and $1550\ \text{nm}$ wavelength.

length. Here, the FWHM is calculated in the plane where the power of the central beam is maximally enhanced, and the Bessel length is defined to the point above the array at which the central beam is overcome by the second-order beams and the Bessel approximation breaks down. Similar to bulk implementations, these variables depend on the aperture size of the array and the maximum variation of the Axicon phase, Φ_0 . As shown in Figs. 3.19a–b, as the array aperture size increases, the FWHM increases linearly while the Bessel length exhibits quadratic growth. In contrast, as shown in Figs. 3.19c–d, both the FWHM and the Bessel length are related to the phase parameter, Φ_0 , through power-law scalings. As such, when considering the

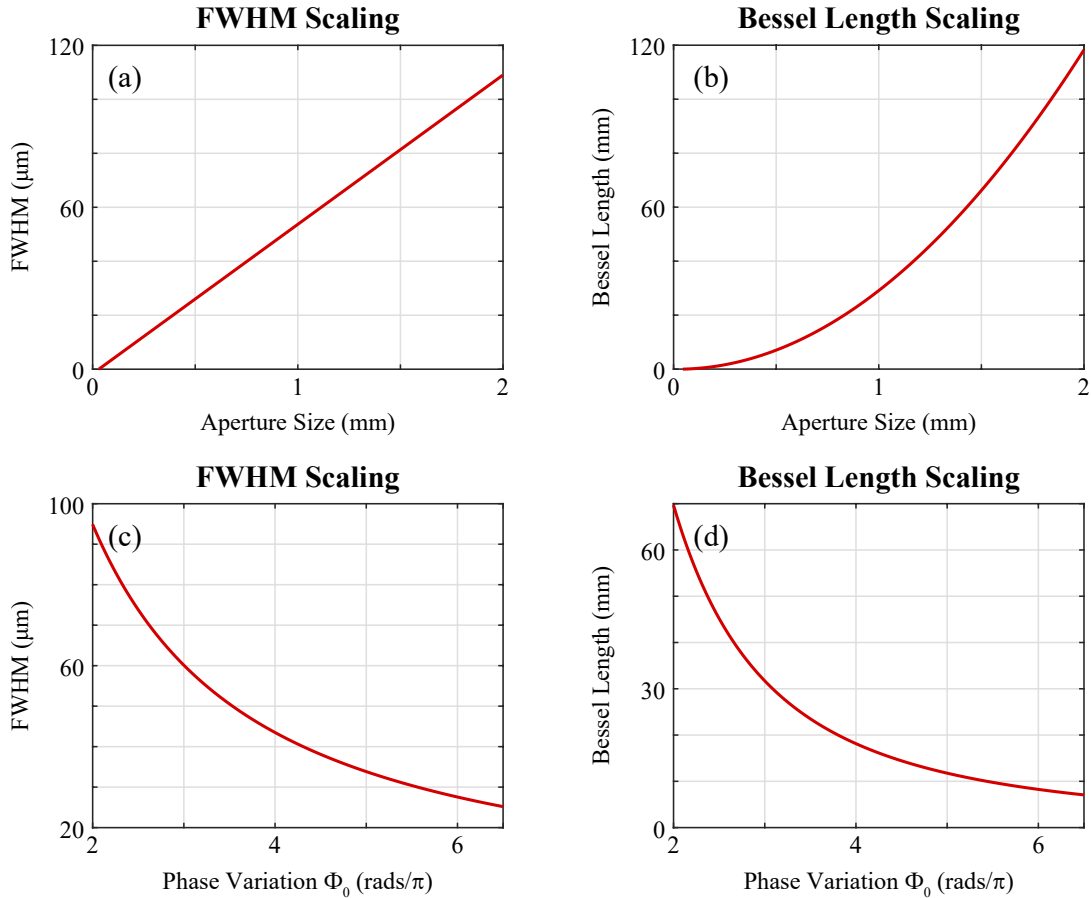


Figure 3.19: Simulated (a) power full width at half maximum (FWHM) and (b) Bessel length versus array aperture size for an array with $\Phi_0 = 5\pi$, $A_0 = 1/2$, and 1550 nm wavelength. Simulated (c) FWHM and (d) Bessel length versus maximum element phase variation, Φ_0 , for an array with 64 antennas, 10 μm antenna pitch, $A_0 = 1/2$, and 1550 nm wavelength.

application space of the device, it is important to consider the trade-offs between a long Bessel length versus a small FWHM. For example, if the device is proposed for simultaneous optical trapping of multiple micron-scale particles at varying heights, both a small FWHM and a long Bessel length are desired.

3.2.3 Architecture

As a proof of concept, a passive quasi-1D Bessel-Gauss-beam-generating integrated optical phased array is designed and fabricated, as shown in Fig. 3.20. The array transmits a Bessel-Gauss beam in the array axis and an exponentially decaying beam in the antenna axis (generation of quasi-1D Bessel beams has been explored [103]). The phased array architecture utilized in the demonstration is based on a silicon-nitride splitter tree [70] with additional components added to enable arbitrary passive control of both the feeding phase and amplitude.

The phased array and accompanying device test structures are fabricated in a CMOS-compatible foundry process at SUNY Poly on a 300-mm-diameter silicon wafer with 6 μm buried oxide thickness. A 200-nm-thick silicon-nitride device layer with a 1.95 refractive index at a 1550 nm wavelength is deposited using a plasma-enhanced chemical vapor deposition process and patterned using 193 nm immersion lithography.

At the input, an on-chip inverse-taper edge coupler is used to efficiently couple light from a 6.5- μm -mode-field-diameter lensed fiber to a 1.5- μm -wide silicon-nitride waveguide.

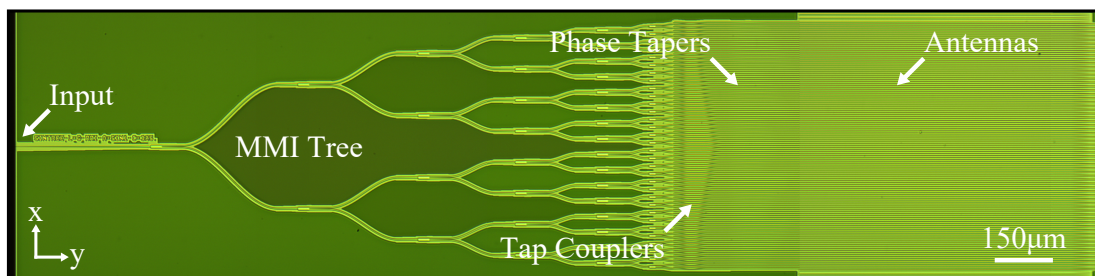


Figure 3.20: Micrograph of the fabricated quasi-Bessel-beam-generating phased array with 64 antennas and 10 μm antenna pitch.

Next, a 6-layer multi-mode-interference (MMI) splitter tree network is used to evenly distribute the input power to 64 waveguide arms with a final pitch of $10\ \mu\text{m}$. As shown in Fig. 3.21a, an MMI is a symmetric 1-to-2-waveguide splitting device based on self-imaging principles [107]. To ensure even splitting with high-efficiency, a finite-difference time-domain (FDTD) solver is used to rigorously simulate the device and optimize its geometry for low insertion loss and coupling into the symmetric mode output. As shown in Fig. 3.21b, by setting the MMI length to $28.7\ \mu\text{m}$ with a $7\ \mu\text{m}$ MMI width and $2.5\text{-}\mu\text{m}$ -wide input and output waveguides, the simulated and measured insertion losses at the design wavelength are found to be $0.04\ \text{dB}$ and less than $0.1\ \text{dB}$, respectively [70].

At the output of the MMI splitter tree, a tap coupler structure (shown in Fig. 3.22a) is placed on each waveguide arm to couple a percentage of the light from each waveguide to a tap port while the remainder of the light in the thru port is routed off the chip (this approach results in inherent power loss which could be mitigated by using a star-coupler [41] or cascaded [71, 106] architecture). As shown in Fig. 3.22b,

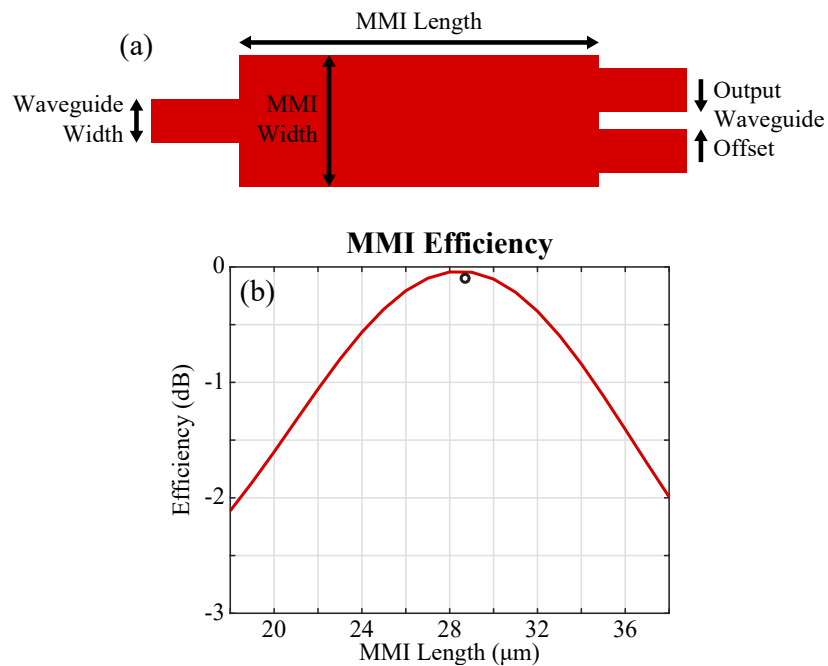


Figure 3.21: (a) Schematic of a multi-mode-interference (MMI) splitter. (b) Simulated (red) and measured (black) efficiency versus MMI device length [70].

by increasing the length of the coupling region while assuming a 500 nm coupling gap, the input power is sinusoidally coupled from the thru port into the tap port of the device. As such, the length of each tap coupler in the array is chosen to enable a Gaussian feeding amplitude, given by Eq. (3.6), to the antennas. Although the variation in these coupler lengths induces a non-uniform phase shift on the output ports, the effect on the phase is minimal due to the small waveguide dispersion of the low-index-contrast waveguides and given the non-compounding nature of the splitter-tree-based architecture compared to cascaded implementations [71, 106].

On the output tap port of each coupler device, a phase taper structure (shown in Fig. 3.23a) is placed to impart a static phase delay dependent on the length of the device's wide section. As shown in Fig. 3.23b, as the length of the 2.2- μm -wide section of the structure is increased while the 185 μm total length is kept constant, the relative phase induced by the structure increases linearly as predicted by waveguide theory. As such, by choosing the appropriate wide-section lengths for each phase taper, the correct phase profile, given by Eq. (3.8), is applied. Due to the modulo

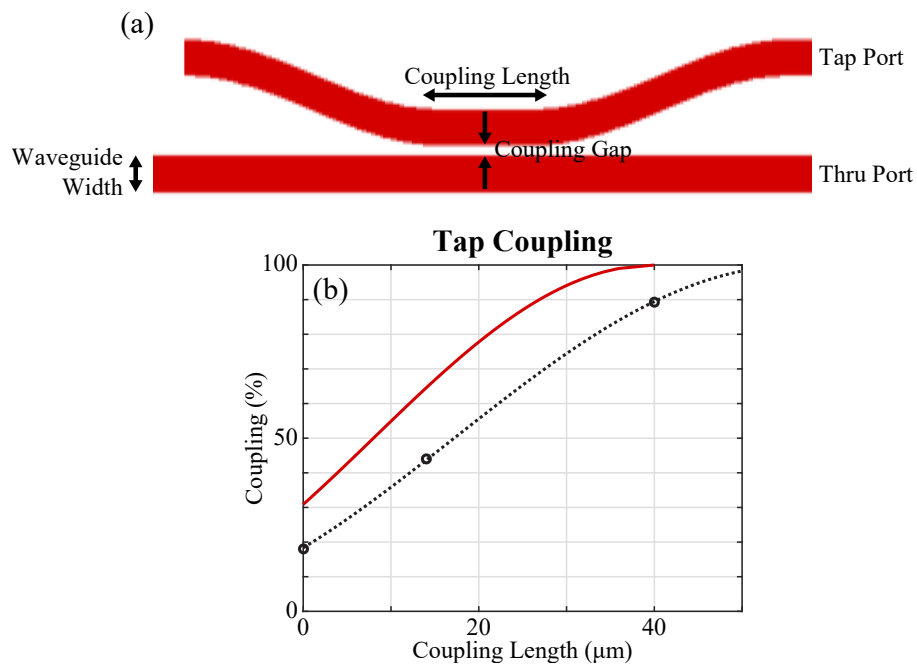


Figure 3.22: (a) Schematic of a tap coupler device. (b) Simulated (red) and measured (black) coupling versus coupling length assuming a 500 nm coupling gap.

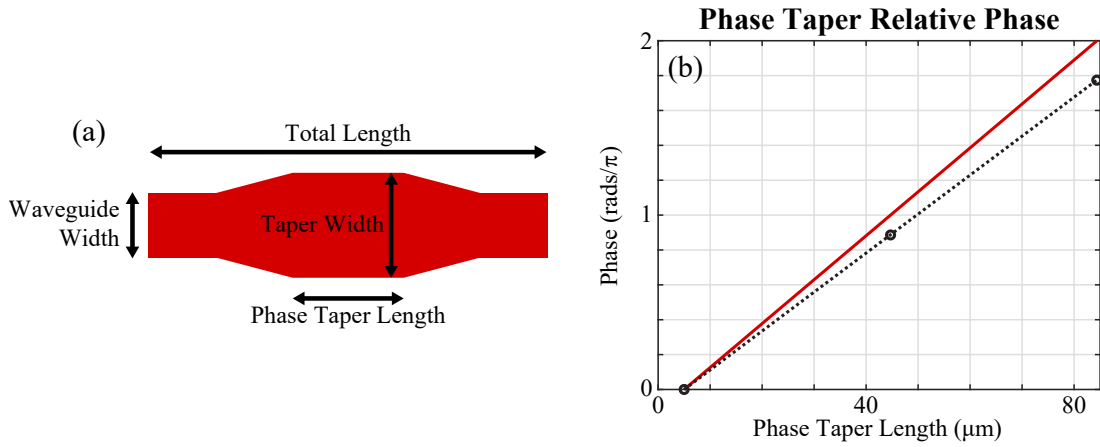


Figure 3.23: (a) Schematic of a phase taper device. (b) Simulated (red) and measured (black) relative phase versus length of the 2.2- μm -wide section of the phase taper.

2π phase encoding and the non-compounding architecture, the system is robust to fabrication-induced phase variations.

Finally, after each phase taper, a 650- μm -long grating-based antenna (shown in Fig. 3.24a) is placed on each arm to create a 0.64 mm \times 0.65 mm aperture size. The antennas are designed to radiate perpendicularly out of the plane of the chip and

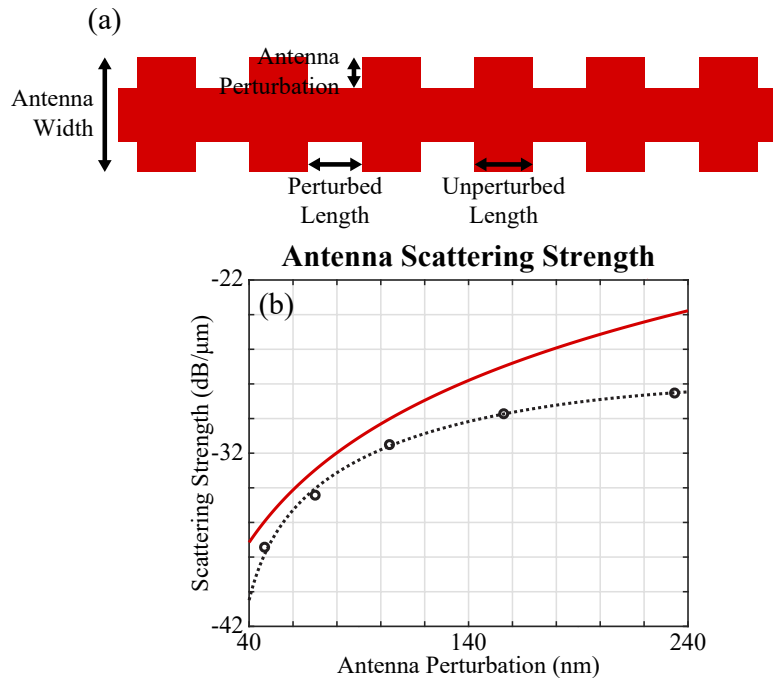


Figure 3.24: (a) Schematic of a grating-based antenna. (b) Simulated (red) and measured (black) scattering strength versus antenna perturbation.

exponentially along the antenna length [70]. By varying the symmetric inward perturbation of the antenna, as shown in Fig. 3.24b, the rate of this exponential radiation – i.e. the scattering strength defined as the power radiated by the antenna per unit length – can be controlled. As such, a 200 nm perturbation and 1027 nm period are chosen to reduce the excess power at the end of the 650- μm -long antennas.

3.2.4 Experimental Results

To characterize the fabricated array, an optical system is used to simultaneously image the plane of the chip onto a visible camera and an InGaAs IR camera. The height of the optical imaging system is then progressively scanned such that top-down views of

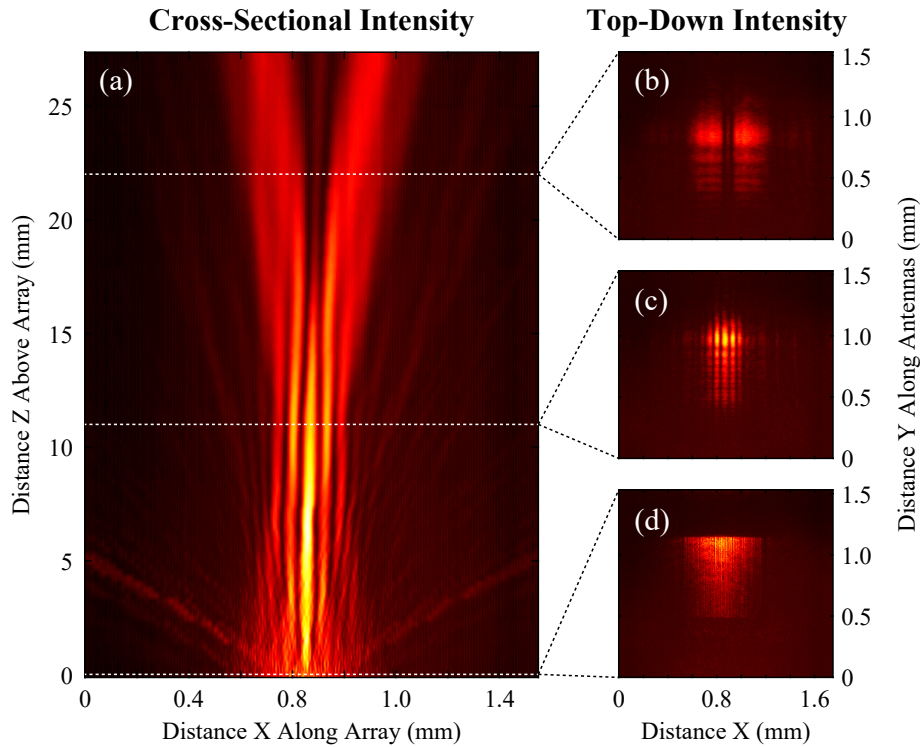


Figure 3.25: (a) Measured cross-sectional intensity (in dB) above the chip for a quasi-Bessel-beam-generating phased array with top-down intensity shown (d) in the plane of the chip ($z = 0$ mm), (c) within the Bessel region of the emitted beam ($z = 11$ mm), and (b) after breakdown of the Bessel region ($z = 22$ mm). Intensities are shown for an array with 64 antennas, 10 μm antenna pitch, $\Phi_0 = 5\pi$, $A_0 = \sqrt{2}/2$, and 1550 nm wavelength.

the intensity at varying heights above the chip are recorded. These top-down views are then integrated in the antenna axis to visualize the cross-sectional intensity as a function of the distance above the chip.

The resulting cross-sectional intensity as a function of the distance above the chip and three top-down views are shown in Figs. 3.25a–d for the fabricated quasi-Bessel-beam-generating array with $\Phi_0 = 5\pi$ and $A_0 = \sqrt{2}/2$. In the plane of the chip (Fig. 3.25d), the aperture is illuminated by the antennas. As the system scans through the Bessel region of the beam (Fig. 3.25c), a characteristic 1D Bessel-Gauss beam is observed with an elongated yet narrow central beam. In this region, a central-beam FWHM of $\sim 30\ \mu\text{m}$ is measured along the Bessel length, closely matching the simulated value of $30.7\ \mu\text{m}$. Finally, above the Bessel length (Fig. 3.25b), the central beam is destroyed, the Bessel breaks down, and the light begins diffracting outwards. The measured Bessel length of $\sim 14\ \text{mm}$ is slightly longer than the simulated value of $11.4\ \text{mm}$. This deviation can be attributed to the imperfect performance of the tap couplers (as shown in Fig. 3.22b) which deforms the feeding amplitude profile of the device.

Next, an $18\text{-}\mu\text{m}$ -diameter gold wire is placed in the path of the central beam along the antenna axis $7.5\ \text{mm}$ above the chip. The resulting cross-sectional intensity as a function of the distance above the chip and three top-down views are shown in Figs. 3.26a–d. As shown in Fig. 3.26d, the wire obstructs the central beam. However, the central beam reforms after a shadow-zone length and continues to propagate with its characteristic elongated profile even after obstruction, as shown in Fig. 3.26b.

3.2.5 Conclusion

In summary, this work presents the first proposal and demonstration of integrated optical phased arrays that generate quasi-Bessel beams in the near field of the array. The phases and amplitudes necessary for Bessel-Gauss beam generation and relevant variables and parameters have been presented and discussed. A new arbitrary phase- and amplitude-controlled splitter-tree-based architecture has been developed and experimental device results have been shown. The array architecture has been used

to experimentally demonstrate a quasi-Bessel-beam-generating array closely matching simulation with a ~ 14 mm Bessel length and ~ 30 μm power FWHM. Due to the elongated properties of Bessel-Gauss beams, this on-chip system has important applications ranging from multi-particle optical trapping to scalable laser lithography.

Since the array is fabricated in a CMOS-compatible platform, it is naturally scalable to an active fully-integrated system with angular-steering capabilities through interfacing with active silicon-based phase shifters [108]. Additionally, two-dimensional Bessel-Gauss-beam generation can be achieved either by appropriately shaping the phase and amplitude characteristics of the antennas in the splitter-tree-based array (through apodization of the period and perturbation strength along the antennas [84]) or by using a two-dimensional emitter-based architecture [71]. Furthermore, the loss

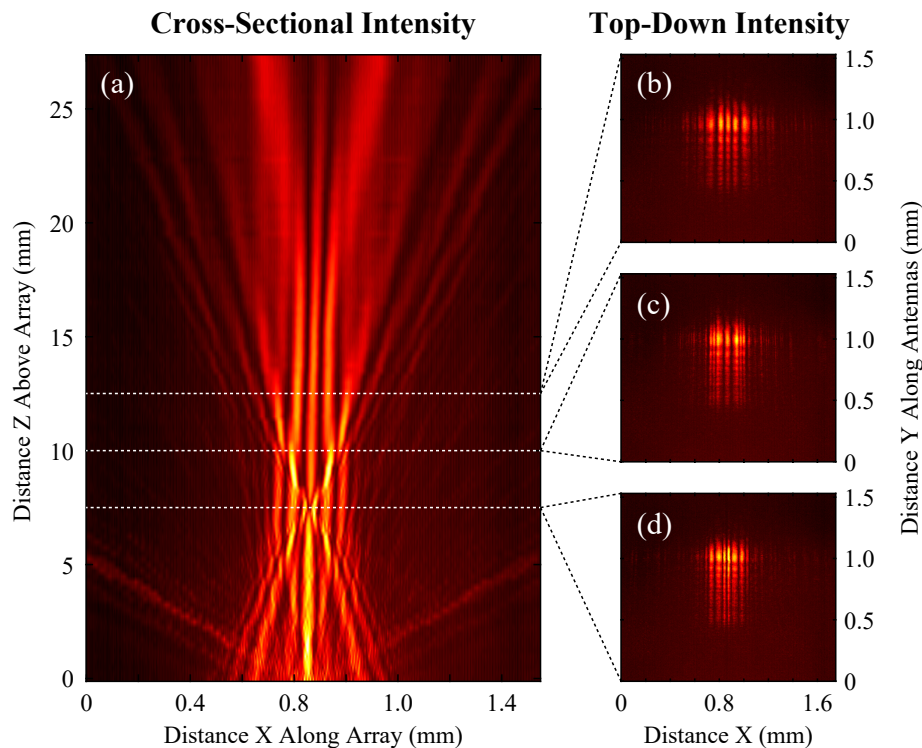


Figure 3.26: (a) Measured cross-sectional intensity (in dB) above the chip for a quasi-Bessel beam generated by a phased array when obstructed by a gold wire. Top-down intensities are shown (d) in the plane of the obstacle ($z = 7.5$ mm), (c) within the shadow zone of the obstacle ($z = 10$ mm), and (b) after reformation of the central beam ($z = 12.5$ mm). Intensities are shown for an array with 64 antennas, 10 μm antenna pitch, $\Phi_0 = 5\pi$, $A_0 = \sqrt{2}/2$, and 1550 nm wavelength.

naturally induced by the tap coupler amplitude approach in the array can be eliminated by using either a star coupler that simultaneously splits the signal and imparts a Gaussian amplitude profile [41] or a cascaded bus architecture with serial taps [71, 106]. Finally, the demonstration can be scaled to larger aperture sizes to enable longer Bessel lengths; for example, assuming the 4 mm aperture previously demonstrated in this platform [70], a 0.48 m Bessel length could be demonstrated.

3.3 Butterfly-Pixel-Based Integrated Optical Phased Arrays

The following work was done in collaboration with Matthew J. Byrd (MIT), Manan Raval (MIT), and Michael R. Watts (MIT). This work has been published in [16,17].

3.3.1 Introduction

As discussed in Ch. 2, integrated optical phased arrays [14, 19, 40, 42] have emerged as a promising technology for many applications, such as light detection and ranging (LiDAR) and free-space optical data communications, due to their ability to manipulate and dynamically steer light in a compact form factor, at low costs, and in a non-mechanical way. Motivated by these initial applications, optical phased array demonstrations to date have primarily focused on systems that utilize dynamic phase control to form and steer far-field beams [40].

However, there are many advantages to introducing dynamic amplitude control to integrated optical phased arrays (in addition to standard phase functionality). For example, amplitude apodization can be used to suppress sidelobes for far-field beam forming [40], and amplitude encoding is required for generation of unique beams and patterns, such as Bessel beams [14] and holographic images [19] (as discussed in Sec. 3.2 and Sec. 4.4, respectively).

Integrated optical phased array architectures with independent amplitude and phase control have been explored [42]. However, these previous demonstrations have generally utilized amplitude components with large form factors, resulting in either in-line control with large antenna pitches and significant higher-order grating lobes or out-of-line control with highly-space-inefficient architectures [42]. Additionally, these standard amplitude components have generally been power inefficient, utilizing either tap couplers with “dump” ports [14] or power attenuators [42].

In this section, a scalable two-dimensional integrated optical phased array architecture with cascaded butterfly-shaped pixels is introduced that enables compact, in-line

independent amplitude and phase control with power recycling for space- and power-efficient operation. Additionally, proof-of-concept experimental data is presented for the key components of the system, confirming the amplitude-control functionality of the architecture.

3.3.2 Architecture and Experimental Results

The integrated optical phased array butterfly architecture consists of an input silicon bus waveguide, a set of butterfly couplers that distribute the input light from the bus waveguide to a set of row waveguides, and a set of cascaded butterfly pixels with compact, in-line antennas that constitute each row of the array, as shown in Fig. 3.27.

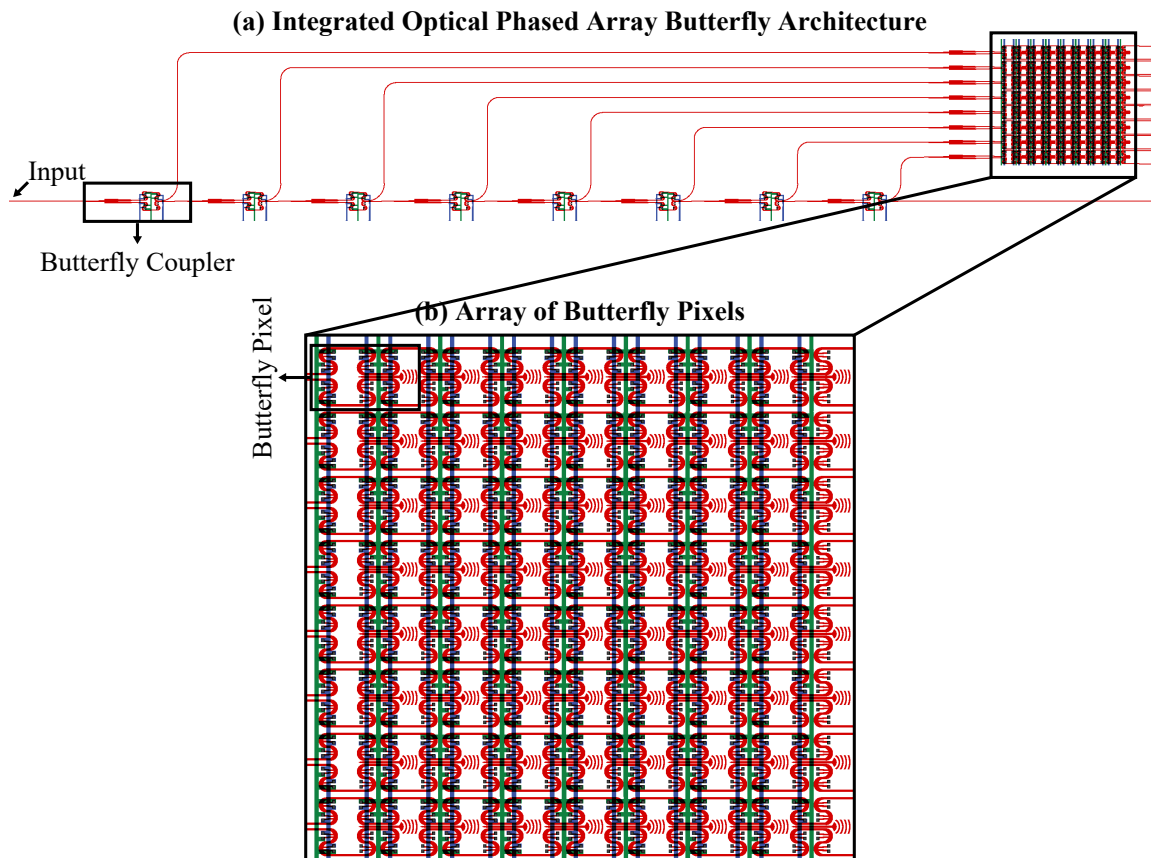


Figure 3.27: (a) Simplified schematic of the integrated optical phased array butterfly architecture with inset showing (b) an 8×8 array of butterfly pixels. In the schematics, the red, green, blue, and black shapes represent the silicon waveguides, bottom metal, top metal, and vias, respectively (doping layers and other process layers are not shown for clarity).

Each butterfly coupler is based on a Mach-Zehnder interferometer (MZI) with two sets of doped waveguide-embedded thermal phase shifters (similar to the shifters used in [40]) on both the top and bottom arms, as shown in Fig. 3.28a. A “phase” signal line for each butterfly coupler is connected to the first set of shifters in both the top and bottom arm while an “amplitude” signal line is connected to the second set of shifters in only the top arm. This enables independent control of the amplitude and phase of the light coupled to the tap port of each coupler and, consequently, arbitrary encoding of the light to each row of the array. (The amplitude-control functionality of a fabricated butterfly coupler was confirmed experimentally, as shown in Fig. 3.28c.)

Similarly, each butterfly pixel is also based on an MZI with two sets of thermal phase shifters for independent amplitude and phase control; however, instead of be-

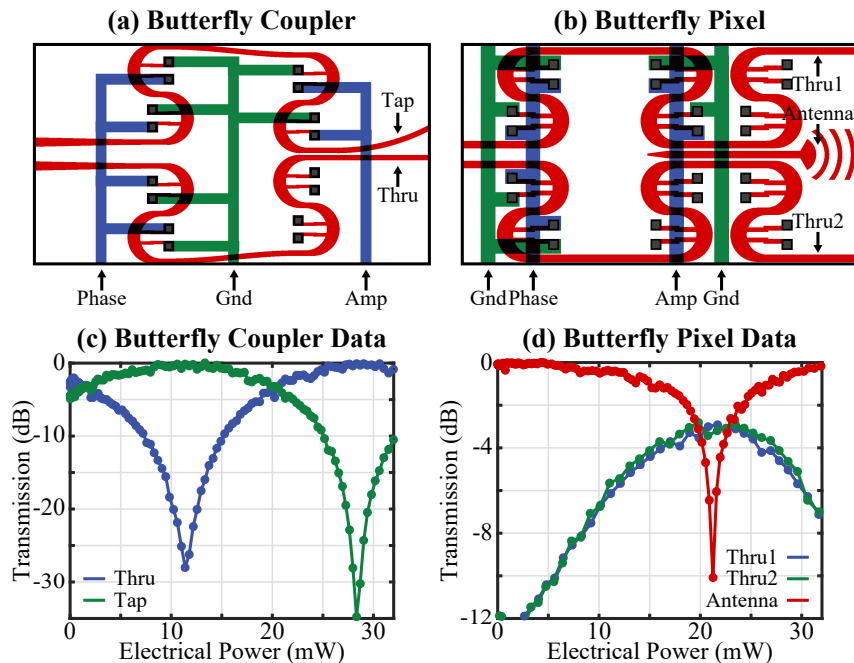


Figure 3.28: Simplified schematics of (a) a butterfly coupler and (b) a butterfly pixel. In the schematics, the red, green, blue, and black shapes represent the silicon waveguides, bottom metal, top metal, and vias, respectively (doping layers and other process layers are not shown for clarity). (c) Experimentally measured transmission into the thru (blue) and tap (green) waveguides versus applied amplitude-line electrical power for the fabricated butterfly coupler. (d) Experimentally measured transmission into the thru waveguides (blue/green) and radiation out of the antenna (red) versus applied amplitude-line electrical power for the fabricated butterfly pixel.

ing terminated with a typical directional coupler, the pixel MZI is terminated with a symmetric three-waveguide coupler (similar to the three-waveguide coupler used in [109]), as shown in Fig. 3.28b. This enables the pixel to connect directly to the subsequent pixel without an additional splitter while also coupling directly to a compact emitter antenna. In the array, all of the “amplitude” signal lines and all of the “phase” signal lines for the pixels in each column are wired together to reduce routing and control complexity while maintaining arbitrary row and column array encoding. (The amplitude-control functionality of a fabricated butterfly pixel was confirmed experimentally, as shown in Fig. 3.28d.)

3.3.3 Conclusion

A scalable two-dimensional integrated optical phased array architecture with cascaded butterfly-shaped pixels has been developed and proof-of-concept experimental data has been presented for the key components of the system. The architecture implements independent amplitude and phase control with no “dump” port in the MZI configuration such that all power can be routed to the antennas with proper amplitude encoding (i.e. power recycling amongst pixels), resulting in a power-efficient architecture. Additionally, the compact, in-line pixel approach enables space efficiency on-chip (important for commercial applications and scaling to larger array sizes) while maintaining reasonable pixel size for reduced higher-order grating lobes. In future work, a scaled-up demonstration of this architecture will be experimentally shown and applied to generate unique amplitude and phase encodings for dynamic far-field sidelobe suppression [40] and complex pattern generation [14, 19].

Chapter 4

Visible-Light Integrated Photonics for Augmented Reality

Augmented-reality head-mounted displays that display information directly in the user's field of view have many wide-reaching applications in defense, medicine, engineering, gaming, etc. However, current commercial head-mounted displays are bulky, heavy, and indiscreet. Moreover, these current displays are not capable of producing holographic images with full depth cues; this lack of depth information results in users experiencing eyestrain and headaches that limit long-term and wide-spread use of these displays (an effect known as the vergence-accommodation conflict).

In this chapter, recent advances in the development of VIPER (Visible Integrated Photonics Enhanced Reality), a novel integrated-photonics-based holographic display, will be reviewed. The VIPER display consists of a single discreet transparent chip that sits directly in front of the user's eye and projects visible-light 3D holograms that only the user can see. It presents a highly-discreet and fully-holographic solution for the next generation of augmented-reality displays.

First, a variety of novel integrated visible-light components, required for the VIPER display, will be demonstrated. The first integrated visible-light liquid-crystal-based phase [20, 21] and amplitude [22, 23] modulators (with device lengths an order of magnitude smaller than traditional inefficient thermo-optic visible-light modula-

tors) will be shown in Sec. 4.1 and Sec. 4.2, respectively. Additionally, the first actively-tunable visible-light integrated optical phased array [24] will be presented in Sec. 4.3 (prior visible-light integrated optical phased arrays have been limited to passive demonstrations).

Next, the VIPER display will be introduced in Sec. 4.4. First, a novel transparent 300-mm-wafer foundry platform on glass for visible-light integrated photonics will be presented [18]. Second, a novel large-scale passive VIPER display that generates a holographic image of a wire-frame cube using 1024 optical-phased-array-based pixels passively encoded to emit light with the appropriate amplitudes and phases will be discussed [18,19]. Third, a novel active VIPER display consisting of cascaded compact active optical-phased-array-based pixels will be shown [18].

4.1 Integrated Visible-Light LC-Based Phase Modulators

The following work was done in collaboration with Milica Notaros (MIT), Manan Raval (MIT), and Michael R. Watts (MIT). This work has been published in [20,21].

4.1.1 Introduction

Integrated photonics systems at visible wavelengths have many wide-reaching potential applications, including dynamic displays and projection systems (such as the VIPER display discussed in Sec. 4.4), underwater optical communications and LiDAR, and optogenetics [19, 110]. Generally, integrated visible-light systems have been demonstrated in silicon-nitride platforms since silicon nitride has a low absorption coefficient within the visible spectrum and is CMOS compatible. However, silicon nitride has a low thermo-optic coefficient and does not exhibit any significant electro-optic properties, which makes integrated phase tuning at visible wavelengths a challenge.

As a solution, nematic liquid crystal (LC), with strong birefringence in the visible spectrum, can be integrated into photonic platforms and used to enable phase modulation. Integrated liquid-crystal-based devices, including slot waveguide phase shifters [111], ring resonators [112, 113], and switches and tuners [114], have been previously explored. However, these demonstrations have been largely limited to infrared wavelengths.

In this section, an integrated visible-light liquid-crystal-based phase modulator is developed and experimentally demonstrated. 36π phase shift is achieved within $\pm 3V$ in a 500- μm -long modulation region.

4.1.2 Theory and Packaging

As shown in Fig. 4.1a, the integrated liquid-crystal-based phase modulator consists of a silicon-nitride waveguide to weakly confine and guide the light, liquid crystal

deposited into an oxide trench above the waveguide to enable strong interaction between the optical mode and the liquid-crystal media, metal electrodes for applying an electric field across the liquid-crystal region, and a top glass chip with a mechanical alignment layer to anchor the liquid-crystal molecules.

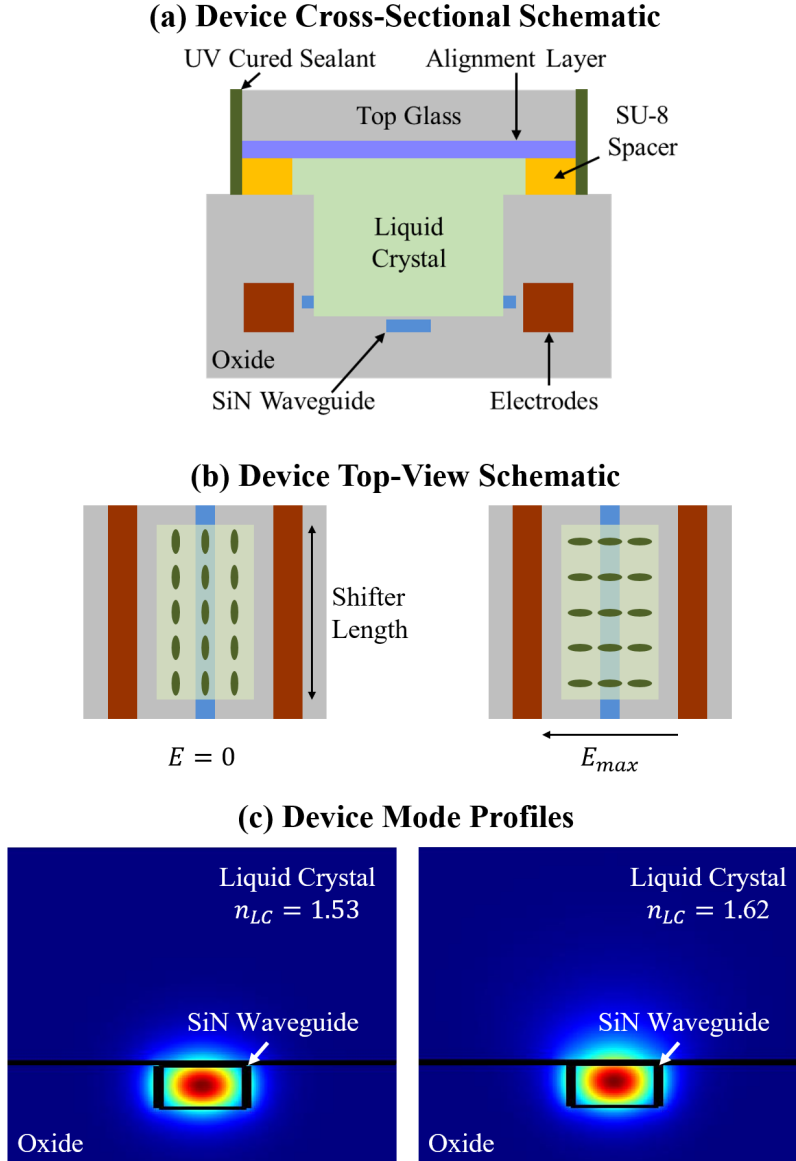


Figure 4.1: (a) Cross-sectional schematic of the integrated liquid-crystal-based phase modulator (not to scale). (b) Top-view schematic of the integrated liquid-crystal-based phase modulator showing the liquid-crystal molecule alignment with no electric field applied versus with maximum electric field applied (not to scale). (c) Simulated mode profiles of the fundamental transverse-electric mode in the integrated liquid-crystal-based phase modulator for a liquid-crystal index of $n_{LC} = 1.53$ versus $n_{LC} = 1.62$.

In the device, phase modulation was achieved by leveraging the birefringence of the liquid crystal. In a nematic liquid-crystal media, the index of refraction varies based on the orientation of the liquid-crystal molecules. Thus, by applying an electric field across the liquid-crystal region to orient the molecules in the direction of the applied field, as shown in Fig. 4.1b, the index of the liquid-crystal media can be actively tuned, resulting in a change in the effective refractive index of the optical mode in the waveguide, as shown in Fig. 4.1c. The resulting relative phase shift due to this change in effective refractive index is given by

$$\Delta\Phi = \frac{2\pi L\Delta n_{\text{eff}}}{\lambda_0}, \quad (4.1)$$

where L is the length of the liquid-crystal region, Δn_{eff} is the change in effective refractive index, and λ_0 is the free-space operating wavelength.

The device was fabricated in a 300-mm wafer-scale CMOS-compatible process at SUNY Poly. A cross-sectional schematic of the device as fabricated by SUNY Poly is shown in Fig. 4.2a. The 160-nm-thick silicon-nitride waveguide is recessed within the silicon dioxide cladding, a trench is etched above the waveguide using a second silicon-nitride etch-stop layer, and metal electrodes are placed along both sides of the trench. Further fabrication and packaging were then done at the MIT fabrication facilities as back-end steps. First, an anisotropic dry etch was performed to etch away some of the excess oxide on top of the waveguide, as shown in Fig. 4.2b. Bringing the trench closer to the top of the waveguide is an important fabrication step, because it enables the optical mode in the device to maximally interact with the liquid crystal, hence allowing for the largest phase shift for a set modulator length. Second, an SU-8 resist spacer layer was deposited around the device, as shown in Fig. 4.2c. Third, a glass chip, with a polyimide alignment layer on the bottom side, was epoxied on top of the spacer layer, as shown in Fig. 4.2d. The alignment layer anchors the liquid-crystal molecules when no electric field is applied. Fourth, 5CB nematic liquid crystal was injected into the formed cavity via capillary action and the cavity was sealed off with UV-cured epoxy, as shown in Fig. 4.2e.

4.1.3 Experimental Results

To enable characterization of the device, the liquid-crystal-based phase modulator was fabricated in an integrated Mach-Zehnder-interferometer (MZI) test structure,

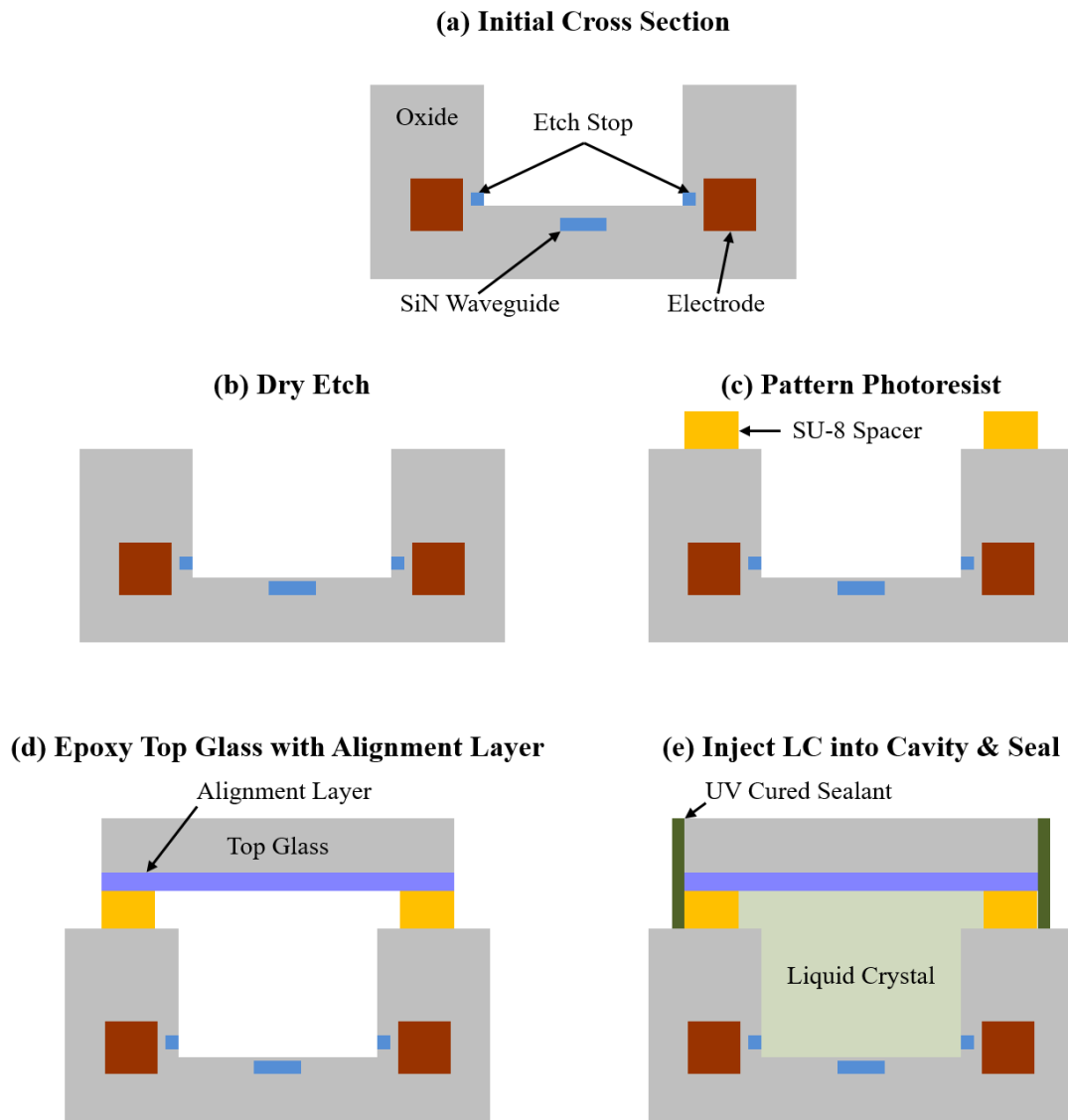


Figure 4.2: Cross-sectional schematic of the liquid-crystal-based phase modulator (a) as received from SUNY Poly with an initial cross section consisting of an SiN waveguide, empty trench, and electrodes, (b) after in-house dry etch to bring the trench closer to the top of the waveguide, (c) after patterning of the SU-8 photoresist spacer layer, (d) after the top glass chip with an alignment layer is epoxied on top of the spacer layer, and (e) after the liquid crystal is injected into the cavity and sealed with the UV-cured epoxy (not to scale).

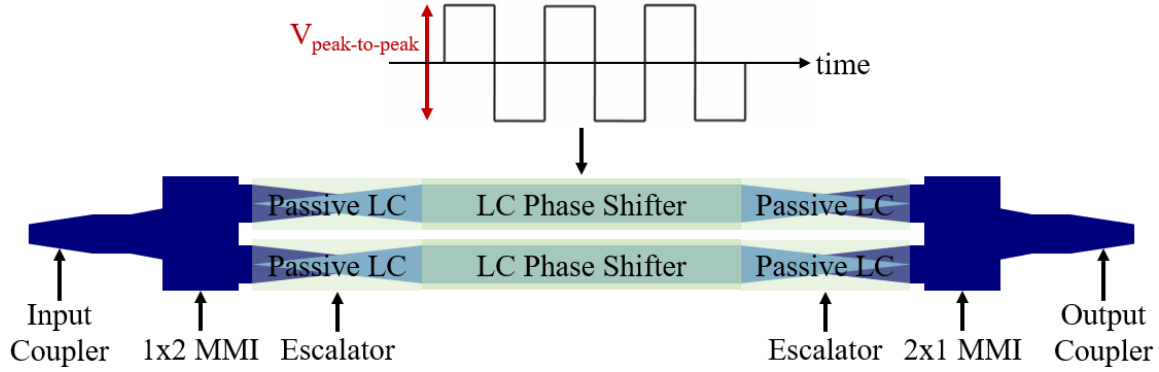


Figure 4.3: Simplified schematic of the integrated MZI test structure and modulation scheme showing major components (not to scale).

as shown in Fig. 4.3. A 632.8-nm-wavelength helium-neon laser was coupled into the chip from an input fiber into the integrated silicon-nitride waveguide using an input edge coupler. A 1×2 multimode interference (MMI) splitter was used to transition from a single waveguide to the two arms of the MZI. A 500- μm -long liquid-crystal-based phase modulator was placed in each arm of the MZI. Finally, a 2×1 MMI was used to combine the two arms of the MZI back into a single waveguide and a second edge coupler was used to couple the light from the chip into an output fiber that was fed into a power meter. A photograph of the fabricated and packaged chip and the experimental setup is shown in Fig. 4.4.

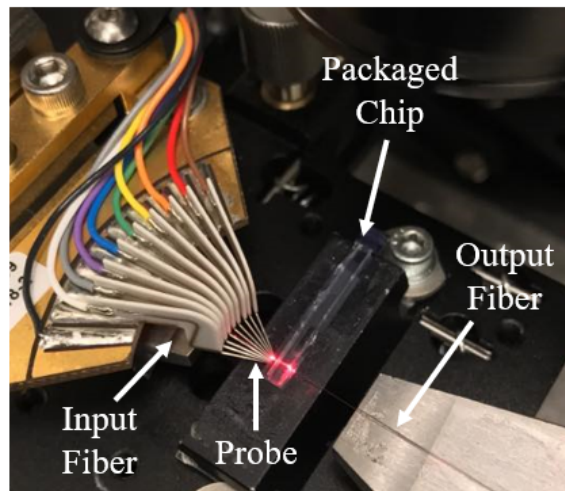


Figure 4.4: Photograph of the fabricated and packaged integrated liquid-crystal-based phase modulator chip and experimental setup.

To characterize the device, electronic probes were used to apply a 10 kHz square wave with a variable peak-to-peak voltage across the electrodes of the phase modulator in one arm of the MZI, as shown in Fig. 4.3. (Note that no voltage was applied across the second phase modulator in the MZI; the liquid-crystal molecules in this modulator were maintained in a constant orientation by the alignment layer.) As shown in Fig. 4.5, as the peak-to-peak voltage applied to the liquid-crystal modulator was varied, phase modulation was achieved, which manifested as amplitude modulation at the output of the MZI test structure. Using this method, 36π phase shift was achieved within $\pm 3\text{ V}$ in the 500- μm -long modulation region. This result corresponds to a 2π phase shifter length of only 28 μm .

4.1.4 Conclusion

In this section, an integrated visible-light liquid-crystal-based phase modulator was developed and experimentally demonstrated. 36π phase shift was achieved within $\pm 3\text{ V}$ in a 500- μm -long modulation region. This device enables compact and low-power integrated visible-light modulation for a variety of applications, ranging from

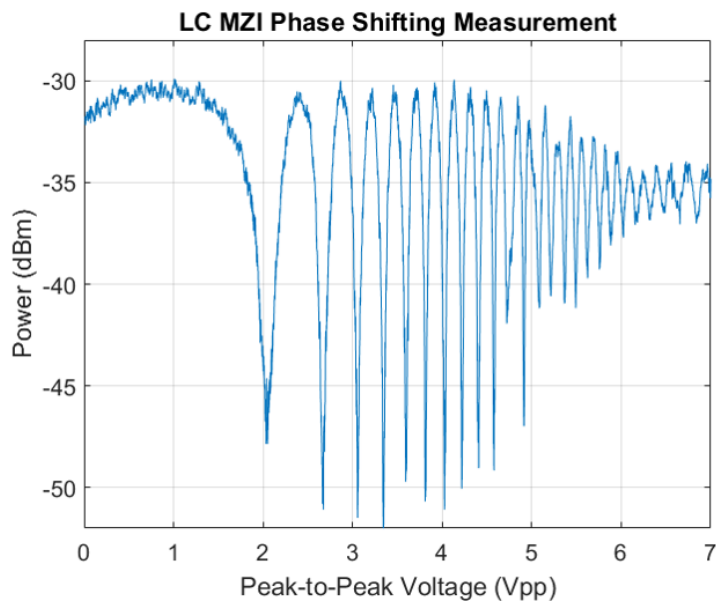


Figure 4.5: Experimental results for the integrated liquid-crystal-based phase modulator showing normalized output power versus peak-to-peak voltage applied to one arm of the MZI test structure.

optogenetics to underwater optical communications and LiDAR [110]. In Sec. 4.4, this integrated visible-light liquid-crystal-based phase modulator will be applied to the VIPER display to enable a dynamic visible-light near-eye holographic display for augmented-reality applications.

4.2 Integrated Visible-Light LC-Based Variable-Tap Amplitude Modulators

The following work was done in collaboration with Milica Notaros (MIT), Manan Raval (MIT), and Michael R. Watts (MIT). This work has been published in [22,23].

4.2.1 Introduction

As discussed in Sec. 4.1, integrated photonics systems at visible wavelengths have many wide-reaching potential applications, including dynamic displays and projection systems (such as the VIPER display discussed in Sec. 4.4), underwater optical communications and LiDAR, and optogenetics [19,110]. Generally, integrated visible-light systems have been demonstrated in silicon-nitride platforms since silicon nitride has a low absorption coefficient within the visible spectrum and is CMOS compatible. However, silicon nitride has a low thermo-optic coefficient and does not exhibit any significant electro-optic properties, which makes integrated phase and amplitude tuning at visible wavelengths a challenge.

As a solution, nematic liquid crystal, with strong birefringence in the visible spectrum, can be integrated into photonic platforms and used to enable modulation. Integrated liquid-crystal-based demonstrations to date have largely focused on liquid-crystal-based phase shifters [21,111,114]. Although amplitude modulation has been achieved by directly integrating these phase shifters in a Mach-Zehnder-interferometer configuration (as shown in Sec. 4.1), this type of configuration has a large form factor since it requires a splitter at both the input and output of the device, phase shifters in each arm of the interferometer, and transitions connecting the liquid-crystal region to the splitters.

In this section, an integrated visible-light liquid-crystal-based variable-tap amplitude modulator is proposed and experimentally demonstrated. The device leverages the birefringence of liquid crystal to actively tune the coupling coefficient between a bus and a tap waveguide and, hence, vary the amplitude of light coupled into the

tap. This small-form-factor variable-tap device provides a compact and low-power solution to visible-light amplitude modulation and will enable high-density integrated visible-light systems.

4.2.2 Theory and Design

The liquid-crystal-based variable-tap amplitude modulator consists of two vertically stacked silicon-nitride waveguides, below an oxide trench filled with liquid crystal, with integrated metal electrodes on either side of the liquid-crystal region, as shown in Fig. 4.6. Light is coupled from a 160-nm-thick bus waveguide, directly beneath the liquid-crystal region, to a 160-nm-thick tap waveguide situated 410 nm below the bus.

The amplitude of the light coupled into the tap waveguide depends on the coupling coefficient between the two waveguides (affected by the mode overlap and difference in

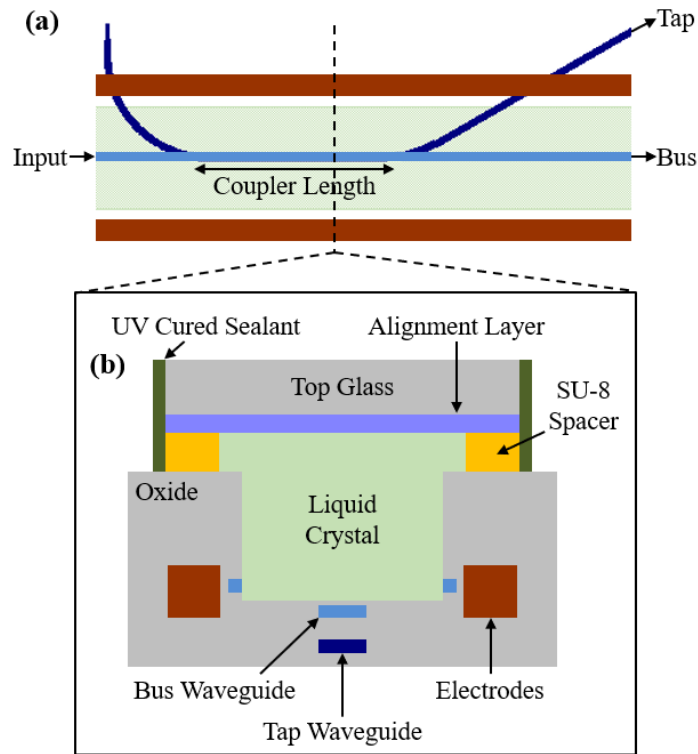


Figure 4.6: (a) Simplified schematic of the liquid-crystal-based variable-tap amplitude modulator. (b) Cross section of the coupling region after packaging (not to scale).

propagation constants). Since the bus waveguide is situated directly underneath the liquid-crystal trench, the confinement and propagation constant of the bus-waveguide mode are highly dependent on the refractive index of the liquid crystal. The liquid-crystal index can be varied from 1.53 to approximately 1.6 by applying an electric field across the liquid-crystal region via the integrated electrodes (as discussed in Sec. 4.1). As the liquid-crystal index increases, the mode in the bus waveguide becomes less confined and is pulled up into the liquid-crystal region, as shown in Fig. 4.1c. This results in less mode overlap with the tap waveguide and a change in effective index of the bus mode (i.e. change in propagation constant), resulting in amplitude modulation of the light coupled into the tap.

To enable optimal device performance, the coupler length and tap waveguide width were chosen to ensure maximum modulation contrast for a given bus waveguide width. First, the coupler length was chosen such that no light is coupled into the tap at the high liquid-crystal index (to take advantage of the bus mode pulling up into the liquid crystal at the higher index). To determine the appropriate length, the tap power versus coupler length was simulated for a variety of tap waveguide widths, as shown in Fig. 4.7a. For example, for a bus width and tap width of 320 nm and 390 nm, respectively, the appropriate coupler length was determined to be 17 μm . Second, the

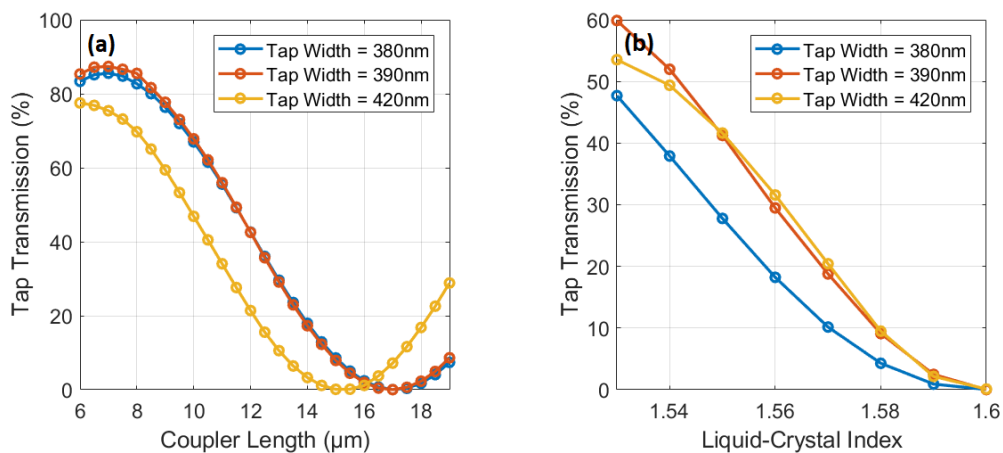


Figure 4.7: (a) Simulated tap transmission versus coupler length for various tap waveguide widths. (b) Simulated tap transmission versus liquid-crystal refractive index for various tap waveguide widths.

tap width was chosen for maximum amplitude variation. To determine the optimal tap width, the tap power versus liquid-crystal index was simulated for each tap width and corresponding coupler length to determine the change in tap transmission, as shown in Fig. 4.7b. For example, for a bus width of 320 nm, the optimal tap width was found to be 390 nm, which results in amplitude variation from 60% to 0%.

4.2.3 Experimental Results

As a proof of concept, a liquid-crystal-based variable-tap amplitude modulator was fabricated in a 300-mm wafer-scale CMOS-compatible process at SUNY Poly and packaged with 5CB nematic liquid crystal using back-end fabrication steps at MIT (as discussed in Sec. 4.1). The final device cross section is shown in Fig. 4.6b. To characterize the fabricated device, a 632.8-nm-wavelength helium-neon laser was coupled onto the chip, electronic probes were used to apply a 10-kHz square wave with a variable peak-to-peak voltage across the electrodes, and the power at the tap output was monitored using a power meter, as shown in Fig. 4.4. To demonstrate the functionality of the device, the peak-to-peak voltage was modulated with a 1-Hz sinusoidal envelope signal (speed limited by the detection equipment), which resulted in ~ 4 dB amplitude modulation at the tap output, as shown in Fig. 4.8.

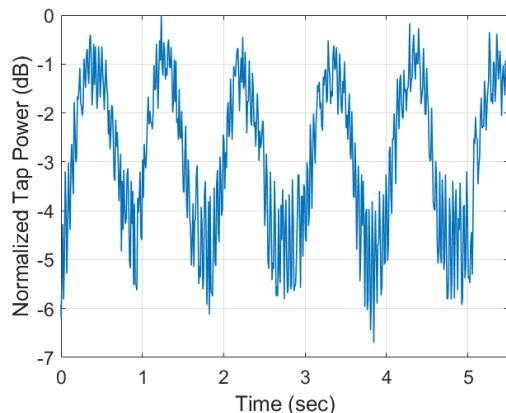


Figure 4.8: Experimental results showing tap power output under 1-Hz modulation (speed limited by the detection equipment).

4.2.4 Conclusion

In this section, a novel integrated visible-light liquid-crystal-based variable-tap amplitude modulator was proposed and experimentally demonstrated. The device leverages the birefringence of liquid crystal to actively tune the coupling coefficient between a bus and a tap waveguide and, hence, vary the amplitude of light coupled into the tap. A design procedure for optimal modulation was identified, a proof-of-concept device was fabricated, and initial experimental amplitude-modulation results were shown. This compact variable tap enables low-power and small-form-factor amplitude modulation for high-density integrated systems at visible wavelengths spanning a variety of applications, ranging from optogenetics to underwater optical communications and LiDAR [110]. In Sec. 4.4, this integrated visible-light liquid-crystal-based variable-tap amplitude modulator will be applied to the VIPER display to enable a dynamic visible-light near-eye holographic display for augmented-reality applications.

4.3 Integrated Visible-Light LC-Based Integrated Optical Phased Arrays

The following work was done in collaboration with Milica Notaros (MIT), Manan Raval (MIT), and Michael R. Watts (MIT). This work has been published in [24].

4.3.1 Introduction

As discussed in Ch. 2, integrated optical phased arrays [35, 41, 67] have emerged as a promising technology for many applications, such as light detection and ranging (LiDAR) and free-space optical data communications, due to their ability to manipulate and dynamically steer free-space light in a compact form factor, at low costs, and in a non-mechanical way. However, optical phased array demonstrations to date have primarily focused on the infrared wavelength regime, although there are many potential wide-reaching applications of optical phased arrays that require visible light operation, including dynamic displays and projection systems (such as the VIPER display discussed in Sec. 4.4), underwater optical communications and LiDAR, and optogenetics.

Recently, visible-light integrated optical phased arrays have been demonstrated in silicon-nitride platforms [19, 70, 115]; however, these systems have been limited to passive demonstrations. Since silicon nitride has a low thermo-optic coefficient and does not exhibit any significant electro-optic properties, integrated phase tuning at visible wavelengths is a challenge. As a solution, nematic liquid crystal, with strong birefringence in the visible spectrum, can be integrated into silicon-nitride platforms to enable visible-light phase modulation with low powers and short lengths (as discussed in Sec. 4.1).

In this section, liquid-crystal-based integrated optical phased arrays are proposed and experimentally demonstrated for the first time as a method for low-power and compact visible-light beam steering. A cascaded integrated optical phased array architecture with a liquid-crystal-based phase-shifting region is developed and used to

experimentally demonstrate beam steering at a 632.8 nm wavelength with a $0.7^\circ \times 2.3^\circ$ power full width at half maximum and 10.5° steering range within ± 3.5 V.

4.3.2 Architecture

As a proof of concept, a visible-light integrated optical phased array was designed, fabricated in a CMOS-compatible foundry process at SUNY Poly, and packaged with liquid crystal using a back-end fabrication process at MIT. The integrated phased array consists of a silicon-nitride-based cascaded-phase-shifter architecture that linearly controls the relative phase applied to an array of antennas, as shown in Fig. 4.9a.

At the input, an on-chip inverse-taper edge coupler couples light from an off-chip laser into an on-chip single-mode silicon-nitride waveguide. A 100- μm -long escalator device (an adiabatic layer transition structure) then couples the input light from the single-mode waveguide into the liquid-crystal-based phase-shifter bus region, as shown in Fig. 4.9b. Next, evanescent tap couplers, placed with a pitch of 20 μm and with

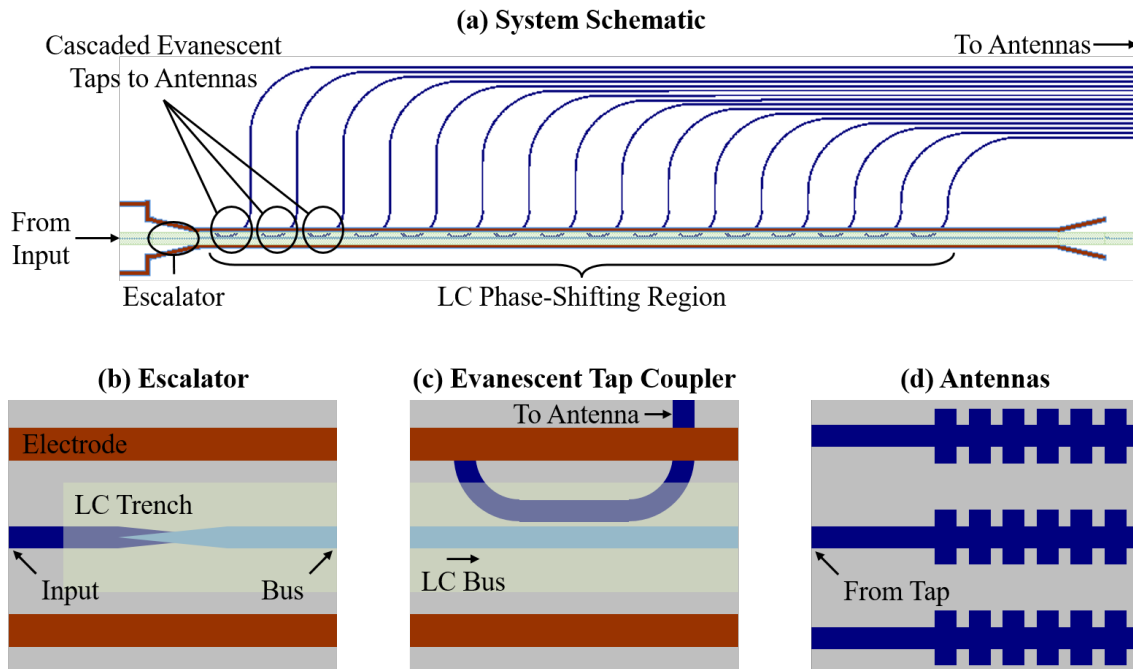


Figure 4.9: (a) Partial schematic of the liquid-crystal-based integrated optical phased array showing major components. Simplified schematics of the (b) layer-transition escalator, (c) evanescent tap coupler, and (d) grating-based antennas used in the liquid-crystal-based integrated optical phased array.

increasing coupling lengths, uniformly distribute the light from the bus region to 16 grating-based 400- μm -long antennas with a 2 μm pitch, shown in Figs. 4.9c–d.

To enable one-dimensional far-field beam steering, the system utilizes the birefringence of liquid-crystal media to enable cascaded phase control to the array of antennas. In a nematic liquid-crystal medium, the index of refraction varies based on the orientation of the liquid-crystal molecules. Thus, by applying an electric field across the liquid-crystal region to orient the molecules in the direction of the applied field, the index of the liquid-crystal media can be actively tuned, resulting in a linear phase shift to the antennas. To enable this functionality, the liquid-crystal-based phase-shifting region consists of a silicon-nitride waveguide to weakly confine and guide the light, liquid crystal deposited into an oxide trench above the waveguide to enable strong interaction between the optical mode and the liquid-crystal media, metal electrodes for applying an electric field across the liquid-crystal region, and a top glass chip with a mechanical alignment layer to anchor the liquid-crystal molecules. Additional details on the liquid-crystal-based phase shifter are provided in Sec. 4.1.

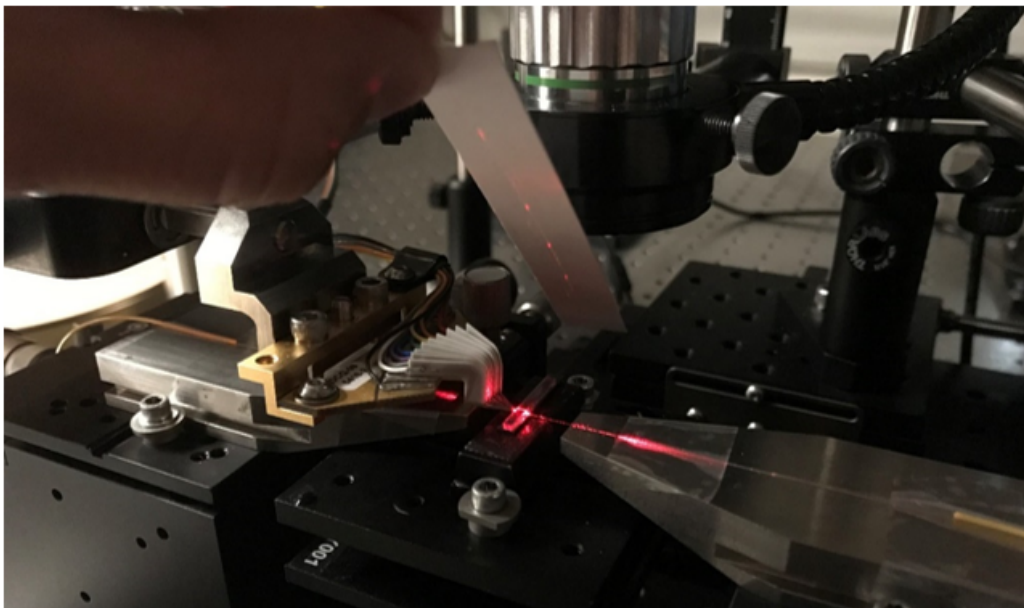


Figure 4.10: Photograph of the packaged optical-phased-array chip, experimental setup, and output radiated light.

4.3.3 Experimental Results

To characterize the fabricated array, a 632.8-nm-wavelength helium-neon laser was coupled onto the chip and an optical system was used to image the far field of the phased array onto a visible-light camera. A photograph of the experimental setup is shown in Fig. 4.10, and the experimentally measured far-field pattern and cross sections of the far-field main lobe are shown in Figs. 4.11a–b. As expected, the array forms a beam in the far field with a $0.7^\circ \times 2.3^\circ$ power full width at half maximum, 8 dB sidelobe suppression, and second-order grating lobes at $\pm 28^\circ$. Next, electronic probes were used to apply a 10 kHz square wave with variable peak-to-peak voltage across the

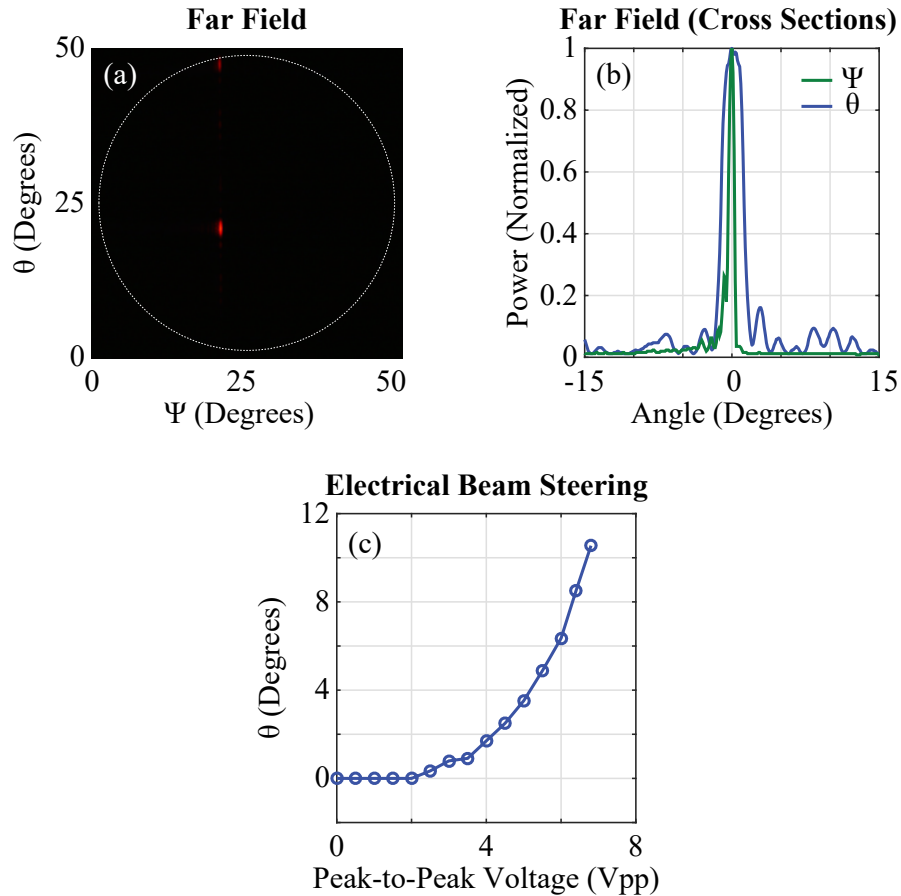


Figure 4.11: (a) Measured far field above the chip showing the main lobe of the phased array. (b) Intensity cross sections of the far-field main lobe in the array dimension (θ) and antenna dimension (Ψ). (c) Experimental results showing beam steering in the array dimension (θ) versus applied peak-to-peak voltage.

electrodes of the liquid-crystal-based phase-shifting region to steer the beam in the array dimension (θ). As shown in Fig. 4.11c, the system enables 10.5° of visible-light beam steering within ± 3.5 V.

4.3.4 Conclusion

This work presents the first proposal and demonstration of liquid-crystal-based integrated optical phased arrays. A cascaded integrated optical phased array architecture with a liquid-crystal-based phase-shifting region was developed and used to experimentally demonstrate visible-light beam steering with a $0.7^\circ \times 2.3^\circ$ power full width at half maximum and 10.5° steering range within ± 3.5 V. This system has many important applications, ranging from optogenetics to underwater optical communications and LiDAR [110]. In Sec. 4.4, this liquid-crystal-based integrated optical phased array will be applied to the VIPER display to enable a dynamic visible-light near-eye holographic display for augmented-reality applications.

4.4 Integrated-Photonics-Based Holographic Displays for Augmented Reality

The following work was done in collaboration with Milica Notaros (MIT), Thomas Dyer (SUNY Poly), Manan Raval (MIT), Christopher Baiocco (SUNY Poly), and Michael R. Watts (MIT). This work has been partially published in [18,19].

4.4.1 Introduction

In many situations, including military operations and medical interventions, access to real-time information can be a key determinant for success. Traditionally, this information has been displayed in real time using head-down or head-up displays. However, recently, there have been extensive efforts in developing head-mounted displays (HMDs) that are capable of relaying information directly in the user's field of view (FOV). These head-mounted displays enable the user to remain engaged with their surroundings while referencing information to real-world objects and events for an augmented-reality experience.

Typical commercially-available augmented-reality head-mounted displays employ an optical relay system for each eye, wherein an image produced by a microdisplay is magnified using a system of lenses to generate an image superimposed on the external scene at a single virtual focal plane in the user's FOV [116], as shown in Fig. 4.12a. However, the bulk-optics components utilized in these typical head-mounted displays result in large, heavy, and indiscreet head-mounted displays. Additionally, typical head-mounted displays employ low-luminance microdisplays (approximately



Figure 4.12: Simplified diagram of (a) a typical HMD approach using an optical relay system versus (b) the direct-view near-eye VIPER approach.

1000 cd/m²), which render the systems inadequate for use in ambient daylight conditions, and optical relay systems with limited FOVs (limited to <40° compared to the 60° near-peripheral FOV of the human eye). Finally, typical head-mounted displays magnify the microdisplay image such that it appears at a single virtual focal plane (they are not capable of producing holographic images with full depth cues); this lack of depth information results in users experiencing eyestrain and headaches that limit long-term and wide-spread use of these displays (an effect known as the vergence-accommodation conflict). Although there have been a number of recent proposals and initial passive demonstrations of near-eye displays that utilize holographic image projection to emit full phase fronts and resolve the vergence-accommodation conflict [117,118], there is still a growing need for a dynamic, discrete, mobile, large-FOV, high-brightness augmented-reality head-mounted display with full binocular and monocular depth cues.

In this section, VIPER (Visible Integrated-Photonics Enhanced-Reality), a novel integrated-photonics-based visible-light near-eye holographic display, is proposed and experimentally demonstrated as a scalable solution to address this need. The VIPER display consists of a single discrete transparent chip, fabricated in a 300-mm-wafer foundry process, that sits directly in front of the user’s eye, as shown in Fig. 4.13, to enable a direct-view near-eye display approach, as shown in Fig. 4.12b. The display is comprised of a grid of on-chip visible-light optical phased arrays, as shown in

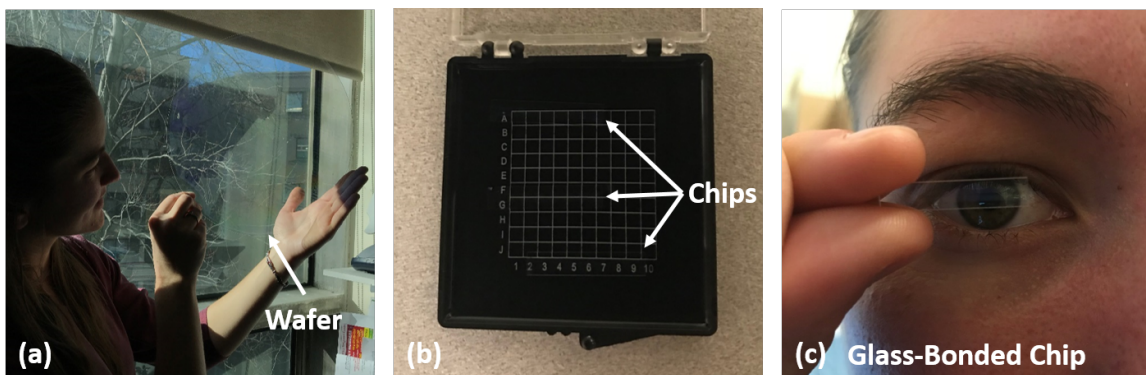


Figure 4.13: Photographs showing (a) a 300-mm-diameter glass-bonded VIPER wafer, (b) three glass-bonded VIPER chips, and (c) a glass-bonded VIPER chip in the near-eye modality.

Fig. 4.14a, that are encoded to emit light with the appropriate amplitudes and phases such that a virtual holographic image is formed that only the user can see, as shown in Fig. 4.14b. It presents a highly-discreet and fully-holographic solution for the next generation of augmented-reality displays.

4.4.2 Passive Architecture and Experimental Results

As an initial proof of concept demonstration, a passive VIPER display was designed at MIT and fabricated in a CMOS-compatible foundry process at SUNY Poly. The display is based on a grid of coherent visible-light integrated optical phased arrays that act as the pixels in the display, as shown in Fig. 4.15. At the input, an on-

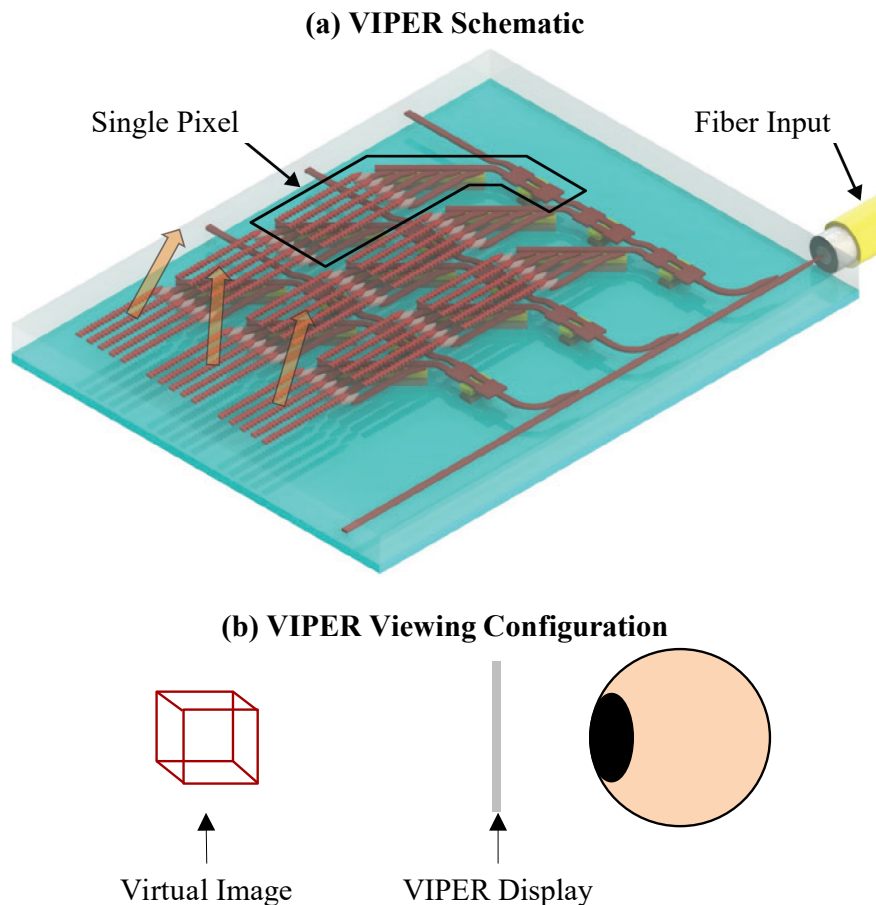


Figure 4.14: (a) Simplified schematic of the VIPER display showing the input optical fiber, active distribution network, and grid of optical-phased-array-based pixels. (b) Viewing configuration for the VIPER display showing the virtual holographic image formed behind the display.

chip inverse-taper edge coupler couples light from an off-chip laser into an on-chip single-mode silicon-nitride waveguide. A 5-stage multi-mode-interference splitter tree evenly distributes the input power to 32 rows with a final pitch of $32\ \mu\text{m}$. On each row, 32 compact optical-phased-array-based pixels are placed with a pixel pitch of $32\ \mu\text{m}$. Each pixel consists of (1) a phase taper structure [14] on the row waveguide to encode the absolute phase of the light emitted by each pixel, (2) an evanescent tap to couple light from the row waveguide to the pixel bus based on the desired pixel amplitude encoding, and (3) evanescent taps with increasing coupling lengths to uniformly distribute light from the pixel bus to 6 grating-based antennas with spatial offsets [115] to enable a linear phase gradient encoding for each pixel.

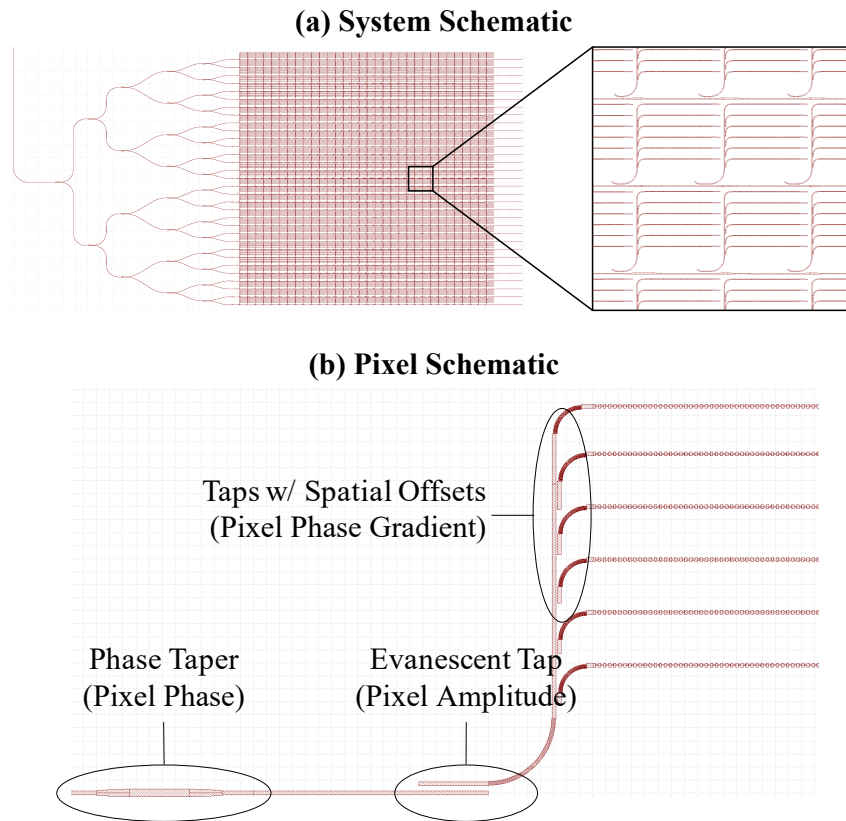


Figure 4.15: (a) Schematic of the passive VIPER display with 32×32 pixels, $32\ \mu\text{m}$ pixel pitch, 6 antennas per a pixel, and $4\ \mu\text{m}$ antenna pitch. (b) Schematic of a single optical-phased-array-based pixel of the passive VIPER display showing the phase taper for pixel absolute phase encoding, evanescent tap for pixel amplitude encoding, and pixel-to-antenna taps with varying spatial offsets for pixel phase gradient encoding.

To generate an example virtual image of a wire-frame cube using the passive VIPER display, a holographic encoding procedure was used to determine the absolute phase, amplitude, and phase gradient encodings for each pixel. Specifically, the holographic phase and amplitude distributions necessary for generating the desired image on the retinal plane were closely approximated by discretizing these distributions into local one-dimensional phase gradients with arbitrary amplitudes and absolute phases. These discretized phase and amplitude distributions were then iteratively optimized using the Gerchberg-Saxton algorithm [74] to accurately generate the desired virtual image. The resulting image and corresponding amplitude, absolute phase, and phase gradient encodings – simulated assuming a 632.8 nm operating wavelength, 1 m virtual object distance, 12 mm eye relief, and 20 mm human eye focal length – are shown

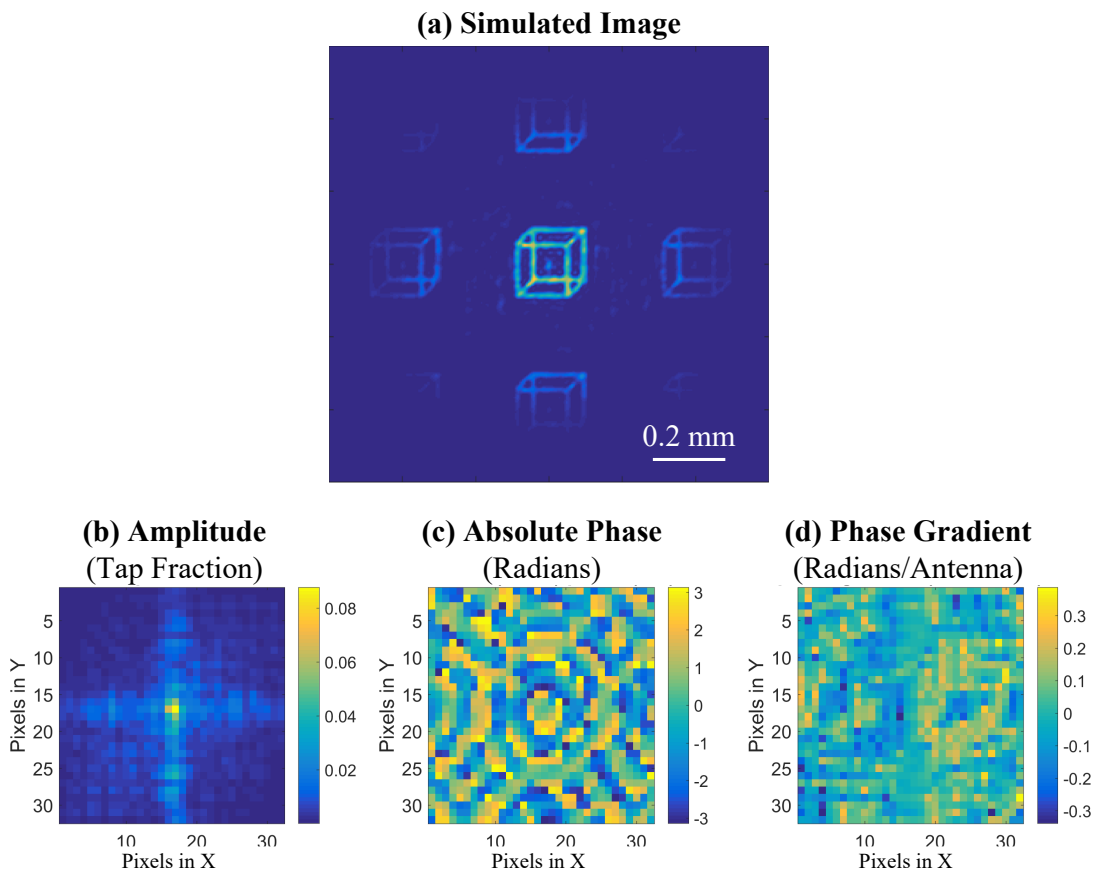


Figure 4.16: (a) Simulation of the virtual image projected by the passive VIPER display and corresponding (b) amplitude, (c) absolute phase, and (d) phase gradient encodings, assuming a 632.8 nm operating wavelength, 1 m virtual object distance, 20 mm human eye focal length, and 12 mm eye relief.

in Fig. 4.16.

To characterize the fabricated passive VIPER display, a 632.8-nm-wavelength helium-neon laser was coupled onto the chip and an optical imaging system, consisting of a 20-mm-focal-length lens and a visible-light camera, was used to emulate the functionality of the human eye (photographs of the experimental setup and fabricated chip are shown in Figs. 4.17a–b). As expected, the display generates the desired wire-frame image at a single focal plane with a virtual object distance around 1 m

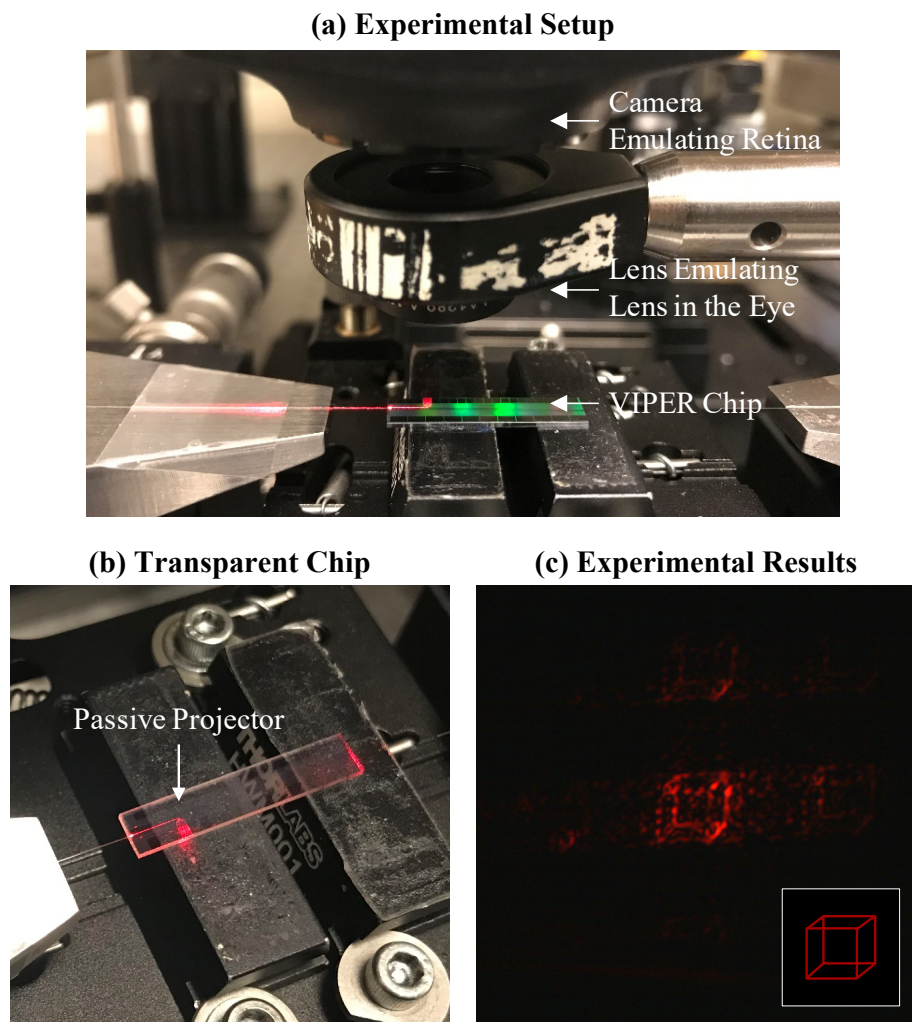


Figure 4.17: Photograph of (a) the VIPER characterization setup showing the input optical fiber, photonic chip, lens emulating the lens in the eye, and camera emulating the retina, and (b) the transparent holographic-display chip. (c) Experimental measurement of the virtual image projected by the passive VIPER display with a ~ 1 m virtual object distance, 20 mm focal length lens, and 12 mm eye relief.

and an emulated eye relief around 12 mm, as shown in Fig. 4.17c.

4.4.3 Active Architecture and Experimental Results

Next, an active video version of the VIPER display was developed by leveraging the integrated liquid-crystal-based components discussed in Sec. 4.1–4.3. Similar to the passive VIPER display, the active display is based on a grid of coherent visible-light integrated optical phased arrays that act as the pixels in the display, as shown in Fig. 4.18; however, in the active display, the amplitude and phase encodings for each

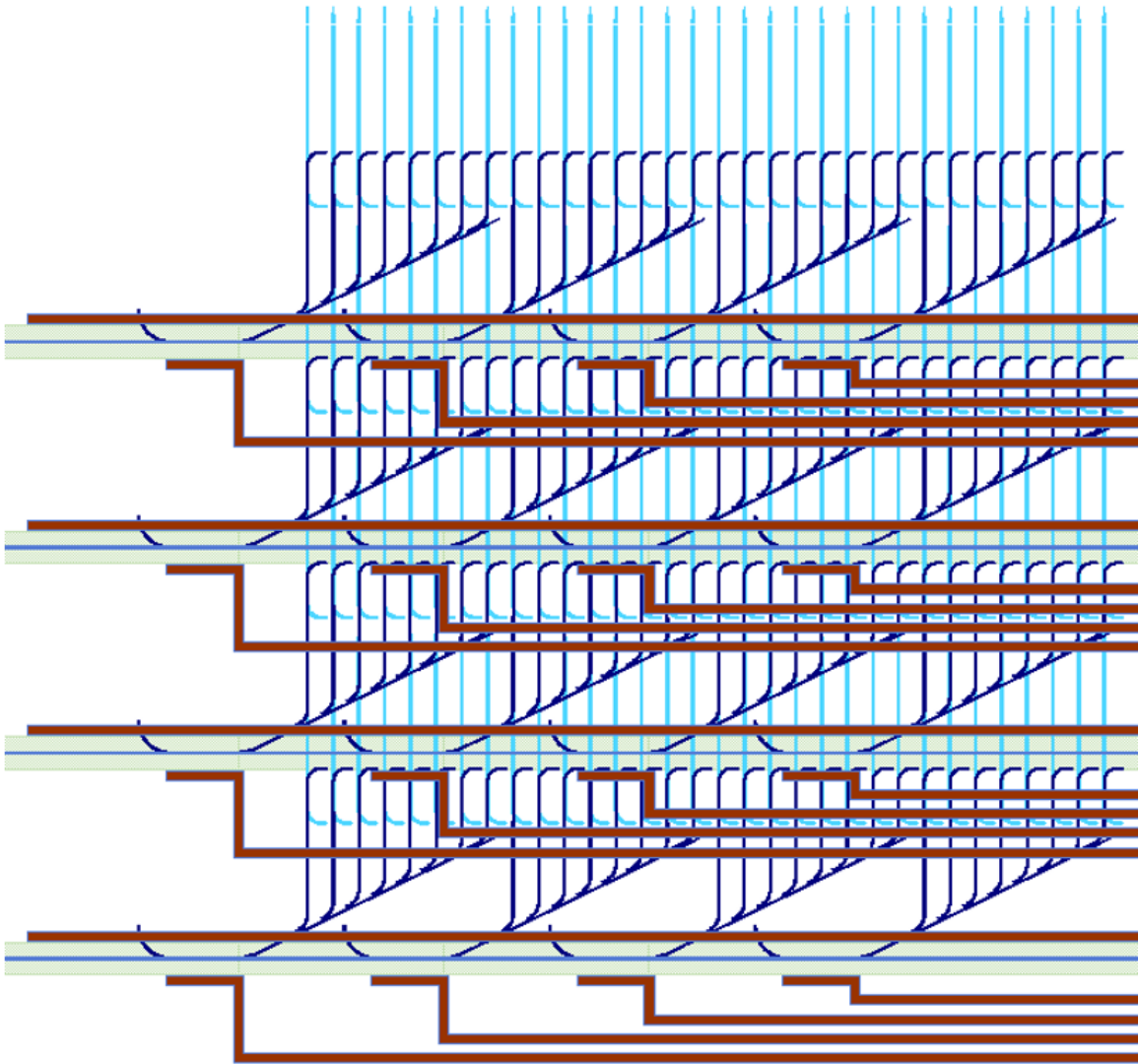


Figure 4.18: Partial schematic of the active VIPER display with 4×4 pixels, $32 \mu\text{m}$ pixel pitch, 8 antennas per a pixel, and $4 \mu\text{m}$ antenna pitch.

pixel are dynamically controlled using liquid-crystal-based components.

At the input, an on-chip inverse-taper edge coupler couples light from an off-chip laser into an on-chip single-mode silicon-nitride waveguide. A 2-stage multi-mode-interference splitter tree evenly distributes the input power to 4 rows with a final pitch of $32\ \mu\text{m}$. On each row, 4 compact optical-phased-array-based pixels are placed with a pixel pitch of $32\ \mu\text{m}$ for a total of 16 pixels in the display.

Figure 4.19 shows a schematic of one of the pixels in the active VIPER display. Each pixel consists of (1) a liquid-crystal-based phase shifter [21] on the row waveguide to modulate the absolute phase of the light emitted by each pixel, (2) a liquid-crystal-based variable tap [23] to modulate the amplitude of light coupled from the row waveguide to each pixel bus, and (3) a liquid-crystal-based pixel bus with compact cascaded pixel-bus-to-antenna taps to distribute the light from the pixel bus to 8

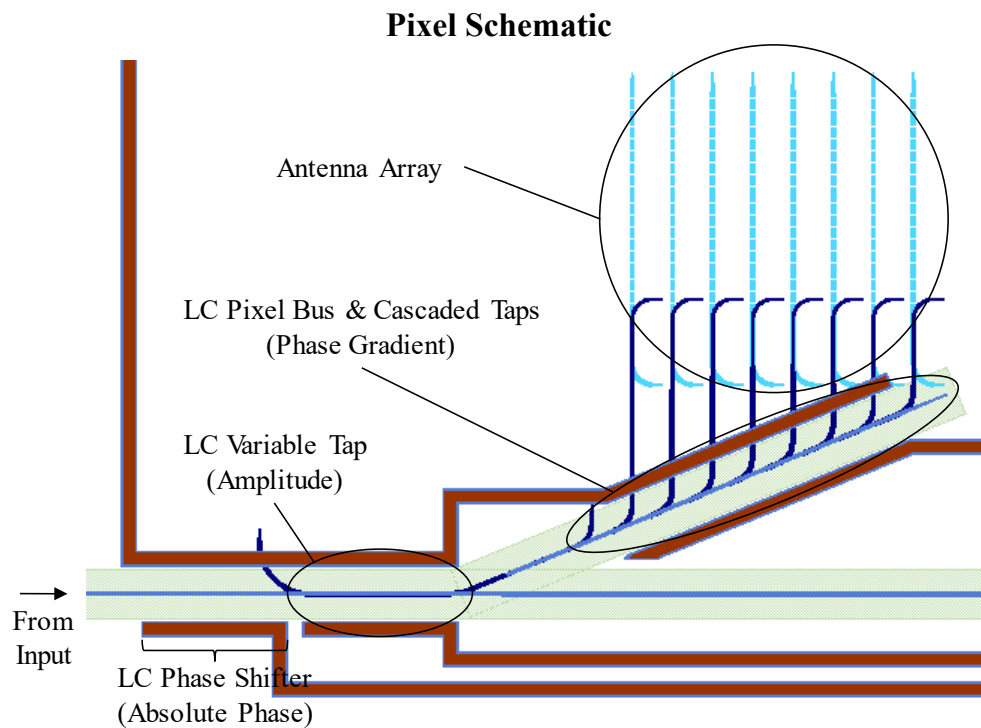


Figure 4.19: Schematic of a single optical-phased-array-based pixel of the active VIPER display showing major components, including the liquid-crystal-based phase shifter for pixel absolute phase encoding, liquid-crystal-based variable tap for pixel amplitude encoding, and liquid-crystal-based pixel bus with compact cascaded pixel-bus-to-antenna taps for pixel phase gradient encoding.

grating-based antennas and modulate the linear phase gradient of the light emitted by each pixel [24].

To characterize the fabricated display, electronic probes were used to apply a 10 kHz square wave with variable peak-to-peak voltage to the active components in one of the pixels in the display. As shown in Figs. 4.20a–b, amplitude modulation from the “off” state to the “on” state with a contrast ratio of approximately 100:1 was achieved within ± 4.5 V and phase gradient modulation of 0.65π per antenna was achieved within ± 4.75 V.

Finally, as an initial demonstration of the video functionality of the active VIPER display, the display was encoded to spell out the letters in the word “LIGHT”. An optical system was then used to image the near field of the chip as the display switched between letters, as shown in Fig. 4.20c.

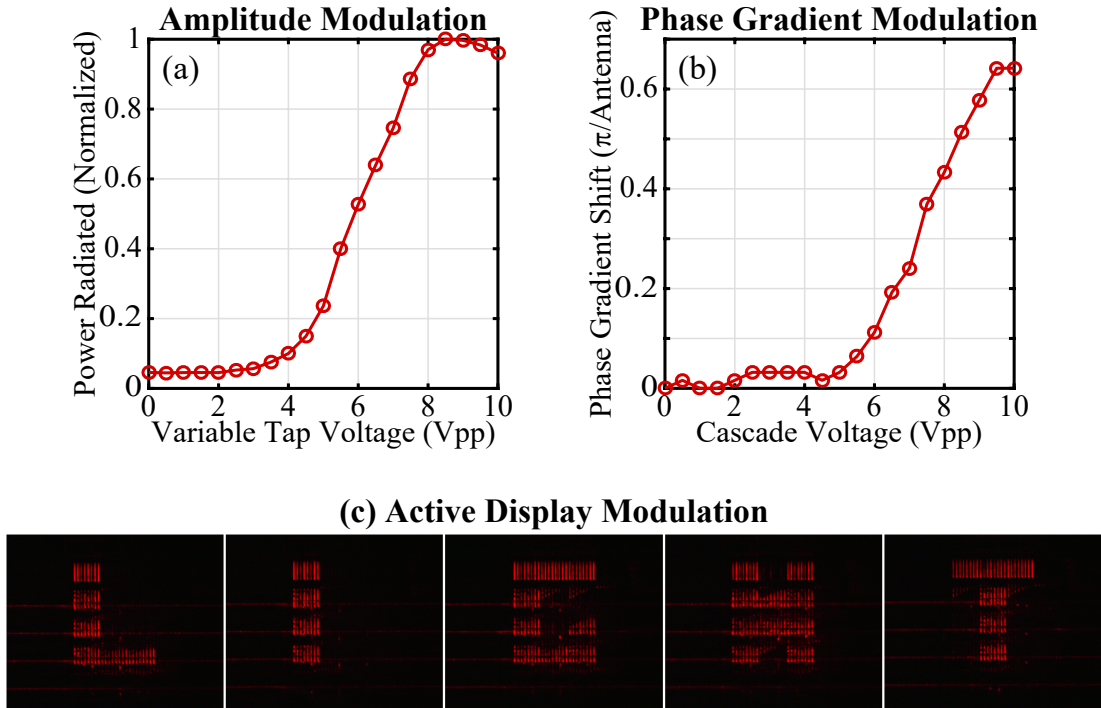


Figure 4.20: Experimental results for a single active VIPER pixel showing (a) power radiated out of the pixel versus applied peak-to-peak variable tap voltage and (b) pixel phase gradient shift versus applied peak-to-peak cascade voltage. (c) Experimental results showing five images of the near field of the multi-pixel active VIPER display; in this experiment, the display was encoded to spell out the letters in the word “LIGHT”.

4.4.4 Conclusion

This work presents the first proposal and demonstration of an integrated-photonics-based visible-light near-eye holographic display. First, a novel transparent 300-mm-wafer foundry platform on glass for visible-light integrated photonics was demonstrated. Next, a passive phased-array-pixel-based architecture and a holographic image encoding methodology were developed and used to experimentally demonstrate virtual image projection of a wire-frame cube with a 32×32 pixel display, 1 m distance to the virtual object, and 12 mm eye relief. Finally, a corresponding active architecture consisting of cascaded compact active optical-phased-array-based pixels was developed and used to experimentally demonstrate initial active video display functionality.

In the future, a custom thin-film-transistor electronics backplane could be developed to enable integrated control of the active VIPER display and scaling up to a large-scale video-hologram demonstration. Furthermore, the architecture of the VIPER display could be further developed to support multi-color functionality. Finally, gain material could be integrated into the VIPER foundry platform to enable on-chip lasers for the VIPER display.

The VIPER system has the potential to enable the next generation of augmented-reality head-mounted displays – with highly-efficient components for daytime operation, compact form factors for discreet and mobile use, and vergence-accommodation-conflict resolution for long-term wear – with a wide range of applications, including military, medical, engineering, and gaming.

Chapter 5

Conclusion

In summary, in this thesis, novel integrated-optical-phased-array devices, systems, results, and applications were presented with a focus on augmented-reality displays and LiDAR sensing [1–6].

In Ch. 2, beam-steering optical phased arrays for LiDAR were shown, including the first beam-steering optical phased array powered by a monolithically-integrated on-chip rare-earth-doped laser [7,8], the first beam-steering optical phased array controlled using heterogeneously-integrated CMOS driving electronics [9,10], and the first single-chip coherent LiDAR with integrated optical phased arrays and CMOS receiver electronics [11]. These demonstrations are important steps towards practical commercialization of low-cost and high-performance integrated LiDAR sensors for autonomous vehicles.

In Ch. 3, integrated optical phased arrays for optical manipulation in the near field were developed, including the first near-field-focusing integrated optical phased arrays [12,13], the first quasi-Bessel-beam-generating integrated optical phased arrays [14,15], and a novel active butterfly architecture for independent amplitude and phase control [16,17]. These near-field modalities have the potential to advance a number of application areas, such as optical trapping for biological characterization, trapped-ion quantum computing, and laser-based 3D printing.

In Ch. 4, a novel transparent integrated-phased-array-based holographic display

was proposed as a highly-discreet and fully-holographic solution for the next generation of augmented-reality head-mounted displays; novel passive near-eye displays that generate holograms [18, 19], the first integrated visible-light liquid-crystal-based phase [20,21] and amplitude [22,23] modulators, and the first actively-tunable visible-light integrated optical phased arrays [24] were presented.

(Note that discussions on remaining challenges and future work for each system are included separately within the conclusions of each section of this thesis.)

Bibliography

- [1] J. Notaros, M. Raval, M. Notaros, and M. R. Watts, “VIPER: Visible integrated photonics enhanced reality,” in *DARPA D60 Symposium*, Defense Advanced Research Projects Agency, 2018.
- [2] J. Notaros, M. Notaros, M. Raval, C. V. Poulton, M. J. Byrd, N. Li, Z. Su, E. S. Magden, E. Timurdogan, T. Dyer, C. Baiocco, T. Kim, P. Bhargava, V. Stojanovic, and M. R. Watts, “Integrated optical phased arrays for LiDAR, communications, augmented reality, and beyond,” in *Applied Industrial Optics*, Optical Society of America, 2020.
- [3] J. Notaros, M. Notaros, M. Raval, C. V. Poulton, M. J. Byrd, N. Li, Z. Su, E. S. Magden, E. Timurdogan, T. Dyer, C. Baiocco, T. Kim, P. Bhargava, V. Stojanovic, and M. R. Watts, “Integrated optical phased arrays: LiDAR, communications, augmented reality, and beyond,” in *Photonic Networks and Devices*, Optical Society of America, 2020.
- [4] J. Notaros, M. Notaros, M. Raval, C. V. Poulton, M. J. Byrd, N. Li, Z. Su, E. S. Magden, E. Timurdogan, T. Dyer, C. Baiocco, T. Kim, P. Bhargava, V. Stojanovic, and M. R. Watts, “Integrated optical phased arrays: LiDAR, communications, augmented reality, and beyond,” in *Silicon Photonics XV*, vol. 11285, pp. 11285–18, International Society for Optics and Photonics, 2020.
- [5] J. Notaros, M. Notaros, M. Raval, C. V. Poulton, M. J. Byrd, N. Li, Z. Su, E. S. Magden, E. Timurdogan, T. Dyer, C. Baiocco, T. Kim, P. Bhargava, V. Stojanovic, and M. R. Watts, “Integrated optical phased arrays: LiDAR, augmented reality, and beyond,” in *Integrated Photonics Research, Silicon and Nanophotonics*, pp. IM4A–2, Optical Society of America, 2019.
- [6] J. Notaros, C. V. Poulton, M. Raval, M. Notaros, N. Li, M. J. Byrd, Z. Su, E. S. Magden, E. Timurdogan, and M. R. Watts, “Integrated optical phased arrays: Architectures and applications,” in *2019 Photonics North (PN)*, pp. 1–1, IEEE, 2019.
- [7] J. Notaros, N. Li, C. V. Poulton, Z. Su, M. J. Byrd, E. S. Magden, E. Timurdogan, C. Baiocco, N. M. Fahrenkopf, and M. R. Watts, “CMOS-compatible optical phased array powered by a monolithically-integrated erbium laser,” *Journal of Lightwave Technology*, vol. 37, no. 24, pp. 5982–5987, 2019.

- [8] J. Notaros, N. Li, C. V. Poulton, Z. Su, M. J. Byrd, E. S. Magden, and M. R. Watts, “CMOS-compatible optical phased arrays with monolithically-integrated erbium lasers,” in *CLEO: Science and Innovations*, pp. STu4B–2, Optical Society of America, 2018.
- [9] T. Kim, P. Bhargava, C. V. Poulton, J. Notaros, A. Yaacobi, E. Timurdogan, C. Baiocco, N. Fahrenkopf, S. Kruger, T. Ngai, Y. Timalsina, M. R. Watts, and V. Stojanovic, “A single-chip optical phased array in a wafer-scale silicon photonics/CMOS 3D-integration platform,” *IEEE Journal of Solid-State Circuits*, vol. 54, no. 11, pp. 3061–3074, 2019.
- [10] T. Kim, P. Bhargava, C. V. Poulton, J. Notaros, A. Yaacobi, E. Timurdogan, C. Baiocco, N. Fahrenkopf, S. Kruger, T. Ngai, Y. Timalsina, M. R. Watts, and V. Stojanovic, “A single-chip optical phased array in a 3D-integrated silicon photonics/65nm CMOS technology,” in *2019 IEEE International Solid-State Circuits Conference-(ISSCC)*, pp. 464–466, IEEE, 2019.
- [11] P. Bhargava, T. Kim, C. Poulton, J. Notaros, A. Yaacobi, E. Timurdogan, C. Baiocco, N. Fahrenkopf, S. Kruger, T. Ngai, Y. Timalsina, M. R. Watts, and V. Stojanovic, “Fully integrated coherent LiDAR in 3D-integrated silicon photonics/65nm CMOS,” in *2019 Symposium on VLSI Circuits*, pp. C262–C263, IEEE, 2019.
- [12] J. Notaros, C. V. Poulton, M. Raval, and M. R. Watts, “Near-field-focusing integrated optical phased arrays,” *Journal of Lightwave Technology*, vol. 36, no. 24, pp. 5912–5920, 2018.
- [13] J. Notaros, C. V. Poulton, M. Raval, M. J. Byrd, D. Coolbaugh, and M. R. Watts, “Fresnel-lens-inspired focusing phased arrays for optical trapping applications,” in *CLEO: Science and Innovations*, p. STh1M.3, Optical Society of America, 2017.
- [14] J. Notaros, C. V. Poulton, M. J. Byrd, M. Raval, and M. R. Watts, “Integrated optical phased arrays for quasi-Bessel-beam generation,” *Optics Letters*, vol. 42, no. 17, pp. 3510–3513, 2017.
- [15] J. Notaros, C. V. Poulton, M. J. Byrd, M. Raval, and M. R. Watts, “Bessel-beam-generating integrated optical phased arrays,” in *CLEO: Science and Innovations*, pp. SM3I–5, Optical Society of America, 2018.
- [16] J. Notaros, M. J. Byrd, M. Raval, and M. R. Watts, “Integrated optical phased array butterfly architecture for independent amplitude and phase control.” in preparation.
- [17] J. Notaros, M. J. Byrd, M. Raval, and M. R. Watts, “Integrated optical phased array butterfly architecture for independent amplitude and phase control,” in *Integrated Photonics Research, Silicon and Nanophotonics*, pp. IM4A–4, Optical Society of America, 2019.

- [18] J. Notaros, M. Notaros, M. Raval, T. Dyer, C. Baiocco, and M. R. Watts, “Integrated-photonics-based holographic display for augmented reality.” in preparation.
- [19] J. Notaros, M. Raval, M. Notaros, and M. R. Watts, “Integrated-phased-array-based visible-light near-eye holographic projector,” in *CLEO: Science and Innovations*, pp. STu3O–4, Optical Society of America, 2019.
- [20] M. Notaros, J. Notaros, M. Raval, and M. R. Watts, “Integrated visible-light liquid-crystal-based phase modulator.” in preparation.
- [21] M. Notaros, M. Raval, J. Notaros, and M. R. Watts, “Integrated visible-light liquid-crystal phase modulator,” in *Frontiers in Optics*, pp. FW6B–5, Optical Society of America, 2018.
- [22] M. Notaros, J. Notaros, M. Raval, and M. R. Watts, “Integrated liquid-crystal-based variable-tap device for visible-light amplitude modulation.” in preparation.
- [23] M. Notaros, J. Notaros, M. Raval, and M. R. Watts, “Integrated visible-light liquid-crystal variable-tap amplitude modulator,” in *Integrated Photonics Research, Silicon and Nanophotonics*, pp. ITh2C–6, Optical Society of America, 2019.
- [24] J. Notaros, M. Notaros, M. Raval, and M. R. Watts, “Liquid-crystal-based visible-light integrated optical phased arrays,” in *CLEO: Science and Innovations*, pp. STu3O–3, Optical Society of America, 2019.
- [25] M. Xin, N. Li, N. Singh, A. Ruocco, Z. Su, E. S. Magden, J. Notaros, D. Vermeulen, E. P. Ippen, M. R. Watts, and F. X. Kärtner, “Optical frequency synthesizer with an integrated erbium tunable laser,” *Light: Science & Applications*, vol. 8, no. 1, pp. 1–8, 2019.
- [26] M. Xin, N. Li, N. Singh, A. Ruocco, Z. Su, E. S. Magden, J. Notaros, D. Vermeulen, E. P. Ippen, M. R. Watts, and F. X. Kärtner, “An optical frequency synthesizer using an integrated erbium tunable laser,” in *CLEO: Science and Innovations*, pp. SW4G–6, Optical Society of America, 2019.
- [27] N. Li, D. Vermeulen, Z. Su, E. S. Magden, M. Xin, N. Singh, A. Ruocco, J. Notaros, C. V. Poulton, E. Timurdogan, C. Baiocco, and M. R. Watts, “Monolithically integrated erbium-doped tunable laser on a CMOS-compatible silicon photonics platform,” *Optics Express*, vol. 26, no. 13, pp. 16200–16211, 2018.
- [28] N. Li, D. Vermeulen, Z. Su, E. S. Magden, A. Ruocco, N. Singh, J. Notaros, M. Xin, C. V. Poulton, E. Timurdogan, C. Baiocco, and M. R. Watts, “CMOS-compatible tunable vernier ring laser using erbium doped waveguide on a silicon photonics platform,” in *CLEO: Science and Innovations*, pp. SW3B–4, Optical Society of America, 2018.

- [29] F. X. Kärtner, P. T. Callahan, K. Shtyrkova, N. Li, N. Singh, M. Xin, R. Koustuban, J. Notaros, E. S. Magden, D. Vermeulen, E. P. Ippen, and M. R. Watts, “Integrated rare-earth doped mode-locked lasers on a CMOS platform,” in *Silicon Photonics: From Fundamental Research to Manufacturing*, vol. 10686, p. 106860F, International Society for Optics and Photonics, 2018.
- [30] N. Li, M. Xin, Z. Su, E. S. Magden, N. Singh, J. Notaros, E. Timurdogan, P. Purnawirman, J. D. B. Bradley, and M. R. Watts, “A silicon photonic data link with a monolithic erbium-doped laser,” *Scientific Reports*, vol. 10, no. 1, pp. 1–9, 2020.
- [31] J. Notaros, J. Mower, M. Heuck, C. Lupo, N. C. Harris, G. R. Steinbrecher, D. Bunandar, T. Baehr-Jones, M. Hochberg, S. Lloyd, and D. Englund, “Programmable dispersion on a photonic integrated circuit for classical and quantum applications,” *Optics Express*, vol. 25, no. 18, pp. 21275–21285, 2017.
- [32] J. Notaros, J. Mower, M. Heuck, N. C. Harris, G. R. Steinbrecher, D. Bunandar, C. Lupo, T. Baehr-Jones, M. Hochberg, S. Lloyd, and D. Englund, “Tunable-coupling resonator arrays for chip-based quantum enigma machines,” in *CLEO: Fundamental Science*, pp. FTh4C–4, Optical Society of America, 2016.
- [33] U. Chakraborty, J. Carolan, G. Clark, D. Bunandar, J. Notaros, M. Watts, and D. Englund, “Cryogenic operation of silicon photonic electro-optic modulators based on DC kerr effect,” *Bulletin of the American Physical Society*, 2020.
- [34] C. V. Poulton, A. Yaacobi, D. B. Cole, M. J. Byrd, M. Raval, D. Vermeulen, and M. R. Watts, “Coherent solid-state LIDAR with silicon photonic optical phased arrays,” *Optics Letters*, vol. 42, no. 20, pp. 4091–4094, 2017.
- [35] F. Aflatouni, B. Abiri, A. Rekhı, and A. Hajimiri, “Nanophotonic projection system,” *Optics Express*, vol. 23, no. 16, pp. 21012–21022, 2015.
- [36] C. V. Poulton, M. J. Byrd, P. Russo, E. Timurdogan, M. Khandaker, D. Vermeulen, and M. R. Watts, “Long-range LiDAR and free-space data communication with high-performance optical phased arrays,” *IEEE Journal of Selected Topics in Quantum Electronics*, 2019.
- [37] J. Hulme, J. Doylend, M. Heck, J. Peters, M. Davenport, J. Bovington, L. Coldren, and J. Bowers, “Fully integrated hybrid silicon two dimensional beam scanner,” *Optics Express*, vol. 23, no. 5, pp. 5861–5874, 2015.
- [38] J. Doylend, M. Heck, J. Bovington, J. Peters, M. Davenport, L. Coldren, and J. Bowers, “Hybrid III/V silicon photonic source with integrated 1D free-space beam steering,” *Optics Letters*, vol. 37, no. 20, pp. 4257–4259, 2012.
- [39] W. Guo, P. R. Binetti, C. Althouse, M. L. Mašanović, H. P. Ambrosius, L. A. Johansson, and L. A. Coldren, “Two-dimensional optical beam steering with InP-based photonic integrated circuits,” *IEEE Journal of Selected Topics in Quantum Electronics*, vol. 19, no. 4, pp. 6100212–6100212, 2013.

- [40] J. Sun, E. shah Hosseini, A. Yaacobi, D. B. Cole, G. Leake, D. Coolbaugh, and M. R. Watts, “Two-dimensional apodized silicon photonic phased arrays,” *Optics Letters*, vol. 39, no. 2, pp. 367–370, 2014.
- [41] D. N. Hutchison, J. Sun, J. K. Doylend, R. Kumar, J. Heck, W. Kim, C. T. Phare, A. Feshali, and H. Rong, “High-resolution aliasing-free optical beam steering,” *Optica*, vol. 3, no. 8, pp. 887–890, 2016.
- [42] S. Chung, H. Abediasl, and H. Hashemi, “A monolithically integrated large-scale optical phased array in silicon-on-insulator CMOS,” *IEEE Journal of Solid-State Circuits*, vol. 53, no. 1, pp. 275–296, 2017.
- [43] R. Fatemi, A. Khachaturian, and A. Hajimiri, “A nonuniform sparse 2-D large-FOV optical phased array with a low-power PWM drive,” *IEEE Journal of Solid-State Circuits*, 2019.
- [44] J. K. Doylend, M. Heck, J. T. Bovington, J. D. Peters, L. Coldren, and J. Bowers, “Two-dimensional free-space beam steering with an optical phased array on silicon-on-insulator,” *Optics Express*, vol. 19, no. 22, pp. 21595–21604, 2011.
- [45] <https://www.intel.com/content/dam/www/public/us/en/documents/product-briefs/optical-transceiver-100g-psm4-qsf28-brief.pdf>.
- [46] B. R. Koch, E. J. Norberg, B. Kim, J. Hutchinson, J.-H. Shin, G. Fish, and A. Fang, “Integrated silicon photonic laser sources for telecom and datacom,” in *National Fiber Optic Engineers Conference*, pp. PDP5C–8, Optical Society of America, 2013.
- [47] D. Liang, X. Huang, G. Kurczveil, M. Fiorentino, and R. Beausoleil, “Integrated finely tunable microring laser on silicon,” *Nature Photonics*, vol. 10, no. 11, p. 719, 2016.
- [48] E. S. Magden, N. Li, J. D. B. Bradley, N. Singh, A. Ruocco, G. S. Petrich, G. Leake, D. D. Coolbaugh, E. P. Ippen, M. R. Watts, and L. A. Kolodziejski, “Monolithically-integrated distributed feedback laser compatible with CMOS processing,” *Optics Express*, vol. 25, no. 15, pp. 18058–18065, 2017.
- [49] N. Li, Z. Su, E. S. Magden, P. T. Callahan, K. Shtyrkova, M. Xin, A. Ruocco, C. Baiocco, E. P. Ippen, F. X. Kärtner, J. D. B. Bradley, D. Vermeulen, and M. R. Watts, “High-power thulium lasers on a silicon photonics platform,” *Optics Letters*, vol. 42, no. 6, pp. 1181–1184, 2017.
- [50] Purnawirman, N. Li, E. S. Magden, G. Singh, N. Singh, A. Baldycheva, E. S. Hosseini, J. Sun, M. Moresco, T. N. Adam, G. Leake, D. Coolbaugh, J. D. B. Bradley, and M. R. Watts, “Ultra-narrow-linewidth Al₂O₃:Er³⁺ lasers with a wavelength-insensitive waveguide design on a wafer-scale silicon nitride platform,” *Optics Express*, vol. 25, no. 12, pp. 13705–13713, 2017.

- [51] Purnawirman, N. Li, G. Singh, E. S. Magden, Z. Su, N. Singh, M. Moresco, G. Leake, J. D. B. Bradley, and M. R. Watts, “Reliable integrated photonic light sources using curved Al₂O₃:Er³⁺ distributed feedback lasers,” *IEEE Photonics Journal*, vol. 9, no. 4, pp. 1–9, 2017.
- [52] N. Li, E. S. Magden, Z. Su, N. Singh, A. Ruocco, M. Xin, M. Byrd, P. T. Callahan, J. D. B. Bradley, C. Baiocco, D. Vermeulen, and M. R. Watts, “Broadband 2- μ m emission on silicon chips: monolithically integrated holmium lasers,” *Optics Express*, vol. 26, no. 3, pp. 2220–2230, 2018.
- [53] M. Belt, T. Huffman, M. L. Davenport, W. Li, J. S. Barton, and D. J. Blumenthal, “Arrayed narrow linewidth erbium-doped waveguide-distributed feedback lasers on an ultra-low-loss silicon-nitride platform,” *Optics Letters*, vol. 38, no. 22, pp. 4825–4828, 2013.
- [54] M. Belt and D. J. Blumenthal, “Erbium-doped waveguide DBR and DFB laser arrays integrated within an ultra-low-loss Si₃N₄ platform,” *Optics Express*, vol. 22, no. 9, pp. 10655–10660, 2014.
- [55] E. Bernhardt, H. A. van Wolferen, L. Agazzi, M. Khan, C. Roeloffzen, K. Wörhoff, M. Pollnau, and R. De Ridder, “Ultra-narrow-linewidth, single-frequency distributed feedback waveguide laser in Al₂O₃:Er³⁺ on silicon,” *Optics Letters*, vol. 35, no. 14, pp. 2394–2396, 2010.
- [56] E. Bernhardt, H. A. van Wolferen, K. Wörhoff, R. De Ridder, and M. Pollnau, “Highly efficient, low-threshold monolithic distributed-bragg-reflector channel waveguide laser in Al₂O₃:Yb³⁺,” *Optics Letters*, vol. 36, no. 5, pp. 603–605, 2011.
- [57] N. Li, Z. Su, Purnawirman, E. Salih Magden, C. V. Poulton, A. Ruocco, N. Singh, M. J. Byrd, J. D. B. Bradley, G. Leake, and M. R. Watts, “Athermal synchronization of laser source with WDM filter in a silicon photonics platform,” *Applied Physics Letters*, vol. 110, no. 21, p. 211105, 2017.
- [58] A. H. Atabaki, S. Moazeni, F. Pavanello, H. Gevorgyan, J. Notaros, L. Alloatti, M. T. Wade, C. Sun, S. A. Kruger, H. Meng, K. Al Qubaisi, I. Wang, B. Zhang, A. Khilo, C. V. Baiocco, M. A. Popovic, V. M. Stojanovic, and R. J. Ram, “Integrating photonics with silicon nanoelectronics for the next generation of systems on a chip,” *Nature*, vol. 556, no. 7701, p. 349, 2018.
- [59] D. T. Spencer, T. Drake, T. C. Briles, J. Stone, L. C. Sinclair, C. Fredrick, Q. Li, D. Westly, B. R. Ilic, A. Bluestone, N. Volet, T. Komljenovic, L. Chang, S. H. Lee, D. Y. Oh, M.-G. Suh, K. Y. Yang, M. H. P. Pfeiffer, T. J. Kippenberg, E. Norberg, L. Theogarajan, K. Vahala, N. R. Newbury, K. Srinivasan, J. E. Bowers, S. A. Diddams, and S. B. Papp, “An optical-frequency synthesizer using integrated photonics,” *Nature*, vol. 557, no. 7703, pp. 81–85, 2018.

- [60] E. Timurdogan, C. M. Sorace-Agaskar, J. Sun, E. S. Hosseini, A. Biberman, and M. R. Watts, “An ultralow power athermal silicon modulator,” *Nature Communications*, vol. 5, 2014.
- [61] W. D. Sacher, J. C. Mikkelsen, Y. Huang, J. C. C. Mak, Z. Yong, X. Luo, Y. Li, P. Dumais, J. Jiang, D. Goodwill, E. Bernier, P. G.-Q. Lo, and J. K. S. Poon, “Monolithically integrated multilayer silicon nitride-on-silicon waveguide platforms for 3-D photonic circuits and devices,” *Proceedings of the IEEE*, no. 99, pp. 1–14, 2018.
- [62] <http://www.aimphotonics.com/pdk>.
- [63] K. Worhoff, J. D. B. Bradley, F. Ay, D. Geskus, T. P. Blauwendraat, and M. Pollnau, “Reliable low-cost fabrication of low-loss Al₂O₃:Er³⁺ waveguides with 5.4-dB optical gain,” *IEEE Journal of Quantum Electronics*, vol. 45, no. 5, pp. 454–461, 2009.
- [64] L. Agazzi, K. Worhoff, and M. Pollnau, “Energy-transfer-upconversion models, their applicability and breakdown in the presence of spectroscopically distinct ion classes: A case study in amorphous Al₂O₃: Er³⁺,” *The Journal of Physical Chemistry C*, vol. 117, no. 13, pp. 6759–6776, 2013.
- [65] N. Li, Purnawirman, J. D. Bradley, G. Singh, E. S. Magden, J. Sun, and M. R. Watts, “Self-pulsing in erbium-doped fiber laser,” in *2015 Optoelectronics Global Conference (OGC)*, pp. 1–2, IEEE, 2015.
- [66] T. Barwicz, Y. Taira, T. W. Lichoulas, N. Boyer, Y. Martin, H. Numata, J. Nah, S. Takenobu, A. Janta-Polczynski, E. L. Kimbrell, R. Leidy, M. H. Khater, S. Kamlapurkar, S. Engelmann, Y. A. Vlasov, and P. Fortier, “A novel approach to photonic packaging leveraging existing high-throughput microelectronic facilities,” *IEEE Journal of Selected Topics in Quantum Electronics*, vol. 22, no. 6, pp. 455–466, 2016.
- [67] S. A. Miller, Y.-C. Chang, C. T. Phare, M. C. Shin, M. Zadka, S. P. Roberts, B. Stern, X. Ji, A. Mohanty, O. A. J. Gordillo, U. D. Dave, and M. Lipson, “Large-scale optical phased array using a low-power multi-pass silicon photonic platform,” *Optica*, vol. 7, no. 1, pp. 3–6, 2020.
- [68] H. Abediasl and H. Hashemi, “Monolithic optical phased-array transceiver in a standard SOI CMOS process,” *Optics Express*, vol. 23, no. 5, pp. 6509–6519, 2015.
- [69] C. McDonough, D. La Tulipe, D. Pascual, P. Tariello, J. Mucci, M. Smalley, A. Nguyen, T. Vo, C. Johnson, P. Nguyen, J. Hebding, G. Leake, M. Moresc, E. Timurdogan, V. Stojanovic, M. R. Watts, and D. Coolbaugh, “Heterogeneous integration of a 300-mm silicon photonics-CMOS wafer stack by direct oxide bonding and via-last 3-D interconnection,” *Journal of Microelectronics and Electronic Packaging*, vol. 13, no. 2, pp. 71–76, 2016.

- [70] C. V. Poulton, M. J. Byrd, M. Raval, Z. Su, N. Li, E. Timurdogan, D. Coolbaugh, D. Vermeulen, and M. R. Watts, “Large-scale silicon nitride nanophotonic phased arrays at infrared and visible wavelengths,” *Optics Letters*, vol. 42, no. 1, pp. 21–24, 2017.
- [71] J. Sun, E. Timurdogan, A. Yaacobi, E. S. Hosseini, and M. R. Watts, “Large-scale nanophotonic phased array,” *Nature*, vol. 493, no. 7431, pp. 195–199, 2013.
- [72] S. Chung, H. Abediasl, and H. Hashemi, “A 1024-element scalable optical phased array in 0.18 μm SOI CMOS,” in *IEEE International Solid-State Circuits Conference (ISSCC)*, pp. 262–263, IEEE, 2017.
- [73] T. Komljenovic, R. Helkey, L. Coldren, and J. E. Bowers, “Sparse aperiodic arrays for optical beam forming and LIDAR,” *Optics Express*, vol. 25, no. 3, pp. 2511–2528, 2017.
- [74] J. Zhou, J. Sun, A. Yaacobi, C. V. Poulton, and M. Watts, “Design of 3D hologram emitting optical phased arrays,” in *Integrated Photonics Research, Silicon and Nanophotonics*, p. IT4A.7, Optical Society of America, 2015.
- [75] D. G. Grier, “A revolution in optical manipulation,” *Nature*, vol. 424, no. 6950, pp. 810–816, 2003.
- [76] C. Bustamante, Z. Bryant, and S. B. Smith, “Ten years of tension: single-molecule dna mechanics,” *Nature*, vol. 421, no. 6921, pp. 423–427, 2003.
- [77] M.-C. Zhong, X.-B. Wei, J.-H. Zhou, Z.-Q. Wang, and Y.-M. Li, “Trapping red blood cells in living animals using optical tweezers,” *Nature Communications*, vol. 4, p. 1768, 2013.
- [78] M. Endres, H. Bernien, A. Keesling, H. Levine, E. R. Anschuetz, A. Krajenbrink, C. Senko, V. Vuletic, M. Greiner, and M. D. Lukin, “Atom-by-atom assembly of defect-free one-dimensional cold atom arrays,” *Science*, p. aah3752, 2016.
- [79] D. Gu, W. Meiners, K. Wissenbach, and R. Poprawe, “Laser additive manufacturing of metallic components: materials, processes and mechanisms,” *International materials reviews*, vol. 57, no. 3, pp. 133–164, 2012.
- [80] J. A. Neff, R. A. Athale, and S. H. Lee, “Two-dimensional spatial light modulators: a tutorial,” *Proceedings of the IEEE*, vol. 78, pp. 826–855, May 1990.
- [81] M. Khorasaninejad and F. Capasso, “Metalenses: Versatile multifunctional photonic components,” *Science*, vol. 358, no. 6367, 2017.
- [82] Y. Zhang, S. Yang, A. E.-J. Lim, G.-Q. Lo, C. Galland, T. Baehr-Jones, and M. Hochberg, “A compact and low loss Y-junction for submicron silicon waveguide,” *Optics Express*, vol. 21, no. 1, pp. 1310–1316, 2013.

- [83] J. Notaros and M. A. Popović, “Finite-difference complex-wavevector band structure solver for analysis and design of periodic radiative microphotonic structures,” *Optics Letters*, vol. 40, no. 6, pp. 1053–1056, 2015.
- [84] J. Notaros, F. Pavanello, M. T. Wade, C. Gentry, A. Atabaki, L. Alloatti, R. J. Ram, and M. Popovic, “Ultra-efficient CMOS fiber-to-chip grating couplers,” in *Optical Fiber Communication Conference*, p. M2I.5, Optical Society of America, 2016.
- [85] K. K. Mehta and R. J. Ram, “Precise and diffraction-limited waveguide-to-free-space focusing gratings,” *Scientific Reports*, vol. 7, no. 1, pp. 1–8, 2017.
- [86] J. Sun, E. Timurdogan, A. Yaacobi, Z. Su, E. S. Hosseini, D. B. Cole, and M. R. Watts, “Large-scale silicon photonic circuits for optical phased arrays,” *IEEE Journal of Selected Topics in Quantum Electronics*, vol. 20, no. 4, pp. 1–15, 2014.
- [87] P. J. Pauzauskie, A. Radenovic, E. Trepagnier, H. Shroff, P. Yang, and J. Liphardt, “Optical trapping and integration of semiconductor nanowire assemblies in water,” *Nature Materials*, vol. 5, no. 2, pp. 97–101, 2006.
- [88] S. H. Simpson and S. Hanna, “Holographic optical trapping of microrods and nanowires,” *JOSA A*, vol. 27, no. 6, pp. 1255–1264, 2010.
- [89] J. Durnin, “Exact solutions for nondiffracting beams. I. the scalar theory,” *JOSA A*, vol. 4, no. 4, pp. 651–654, 1987.
- [90] F. Gori, G. Guattari, and C. Padovani, “Bessel-gauss beams,” *Optics Communications*, vol. 64, no. 6, pp. 491–495, 1987.
- [91] Z. Bouchal, J. Wagner, and M. Chlup, “Self-reconstruction of a distorted non-diffracting beam,” *Optics Communications*, vol. 151, no. 4, pp. 207–211, 1998.
- [92] J. Chen, J. Ng, Z. Lin, and C. Chan, “Optical pulling force,” *Nature Photonics*, vol. 5, no. 9, pp. 531–534, 2011.
- [93] D. McGloin and K. Dholakia, “Bessel beams: diffraction in a new light,” *Contemporary Physics*, vol. 46, no. 1, pp. 15–28, 2005.
- [94] V. Garces-Chavez, D. McGloin, H. Melville, W. Sibbett, and K. Dholakia, “Simultaneous micromanipulation in multiple planes using a self-reconstructing light beam,” *Nature*, vol. 419, no. 6903, pp. 145–147, 2002.
- [95] F. O. Fahrbach, P. Simon, and A. Rohrbach, “Microscopy with self-reconstructing beams,” *Nature Photonics*, vol. 4, no. 11, pp. 780–785, 2010.
- [96] P. Dufour, M. Piché, Y. De Koninck, and N. McCarthy, “Two-photon excitation fluorescence microscopy with a high depth of field using an axicon,” *Applied Optics*, vol. 45, no. 36, pp. 9246–9252, 2006.

- [97] L. Yang, S. Ji, K. Xie, W. Du, B. Liu, Y. Hu, J. Li, G. Zhao, D. Wu, W. Huang, S. Liu, H. Jiang, and J. Chu, "High efficiency fabrication of complex microtube arrays by scanning focused femtosecond laser Bessel beam for trapping/releasing biological cells," *Optics Express*, vol. 25, no. 7, pp. 8144–8157, 2017.
- [98] D. Li, K. Imasaki, S. Miyamoto, S. Amano, and T. Mochizuki, "Conceptual design of Bessel beam cavity for free-electron laser," *International Journal of Infrared and Millimeter Waves*, vol. 27, no. 2, pp. 165–171, 2006.
- [99] O. Ren and R. Birngruber, "Axicon: a new laser beam delivery system for corneal surgery," *IEEE Journal of Quantum Electronics*, vol. 26, no. 12, pp. 2305–2308, 1990.
- [100] S. Li and J. Wang, "Adaptive free-space optical communications through turbulence using self-healing Bessel beams," *Scientific Reports*, vol. 7, 2017.
- [101] N. Chattapiban, E. A. Rogers, D. Cofield, W. T. Hill III, and R. Roy, "Generation of nondiffracting Bessel beams by use of a spatial light modulator," *Optics Letters*, vol. 28, no. 22, pp. 2183–2185, 2003.
- [102] P. García-Martínez, M. M. Sánchez-López, J. A. Davis, D. M. Cottrell, D. Sand, and I. Moreno, "Generation of Bessel beam arrays through Dammann gratings," *Applied Optics*, vol. 51, no. 9, pp. 1375–1381, 2012.
- [103] S. Kang and K. Oh, "1D Bessel-like beam generation by highly directive transmission through a sub-wavelength slit embedded in periodic metallic grooves," *Optics Communications*, vol. 284, no. 22, pp. 5388–5393, 2011.
- [104] X. Li, M. Pu, Z. Zhao, X. Ma, J. Jin, Y. Wang, P. Gao, and X. Luo, "Catenary nanostructures as compact Bessel beam generators," *Scientific Reports*, vol. 6, p. 20524, 2016.
- [105] W. T. Chen, M. Khorasaninejad, A. Y. Zhu, J. Oh, R. C. Devlin, A. Zaidi, and F. Capasso, "Generation of wavelength-independent subwavelength Bessel beams using metasurfaces," *Light Sci. Appl.*, vol. 6, 2017.
- [106] A. Yaacobi, J. Sun, M. Moresco, G. Leake, D. Coolbaugh, and M. R. Watts, "Integrated phased array for wide-angle beam steering," *Optics Letters*, vol. 39, no. 15, pp. 4575–4578, 2014.
- [107] L. B. Soldano and E. C. Pennings, "Optical multi-mode interference devices based on self-imaging: principles and applications," *Journal of Lightwave Technology*, vol. 13, no. 4, pp. 615–627, 1995.
- [108] M. R. Watts, J. Sun, C. DeRose, D. C. Trotter, R. W. Young, and G. N. Nielson, "Adiabatic thermo-optic mach-zehnder switch," *Optics Letters*, vol. 38, no. 5, pp. 733–735, 2013.

- [109] G. Calo, A. D’Orazio, and V. Petruzzelli, “Broadband mach–zehnder switch for photonic networks on chip,” *Journal of Lightwave Technology*, vol. 30, no. 7, pp. 944–952, 2012.
- [110] E. Shim, Y. Chen, S. Masmanidis, and M. Li, “Multisite silicon neural probes with integrated silicon nitride waveguides and gratings for optogenetic applications,” *Scientific Reports*, vol. 6, p. 22693, 2016.
- [111] Y. Xing, T. Ako, J. P. George, D. Korn, H. Yu, P. Verheyen, M. Pantouvaki, G. Lepage, P. Absil, A. Ruocco, C. Koos, J. Leuthold, K. Neyts, J. Beeckman, and W. Bogaerts, “Digitally controlled phase shifter using an SOI slot waveguide with liquid crystal infiltration,” *IEEE Photonics Technology Letters*, vol. 27, no. 12, pp. 1269–1272, 2015.
- [112] W. De Cort, J. Beeckman, T. Claes, K. Neyts, and R. Baets, “Wide tuning of silicon-on-insulator ring resonators with a liquid crystal cladding,” *Optics Letters*, vol. 36, no. 19, pp. 3876–3878, 2011.
- [113] W. De Cort, J. Beeckman, R. James, F. A. Fernández, R. Baets, and K. Neyts, “Tuning of silicon-on-insulator ring resonators with liquid crystal cladding using the longitudinal field component,” *Optics Letters*, vol. 34, no. 13, pp. 2054–2056, 2009.
- [114] H. Desmet, W. Bogaerts, A. Adamski, J. Beeckman, K. Neyts, and R. Baets, “Silicon-on-insulator optical waveguides with liquid crystal cladding for switching and tuning,” in *Proc. ECOC*, vol. 3, pp. 430–431, 2003.
- [115] M. Raval, A. Yaacobi, and M. R. Watts, “Integrated visible light phased array system for autostereoscopic image projection,” *Optics Letters*, vol. 43, no. 15, pp. 3678–3681, 2018.
- [116] B. Kress and T. Starner, “A review of head-mounted displays (HMD) technologies and applications for consumer electronics,” in *Photonic Applications for Aerospace, Commercial, and Harsh Environments IV*, vol. 8720, p. 87200A, International Society for Optics and Photonics, 2013.
- [117] C. Martinez, V. Krotov, B. Meynard, and D. Fowler, “See-through holographic retinal projection display concept,” *Optica*, vol. 5, no. 10, pp. 1200–1209, 2018.
- [118] G.-Y. Lee, J.-Y. Hong, S. Hwang, S. Moon, H. Kang, S. Jeon, H. Kim, J.-H. Jeong, and B. Lee, “Metasurface eyepiece for augmented reality,” *Nature Communications*, vol. 9, no. 1, pp. 1–10, 2018.